FULL-SCALE INVESTIGATION OF CRACK GROWTH BEHAVIOUR UNDER VARIABLE PRESSURE FLUCTUATIONS IN NEAR-NEUTRAL PH ENVIRONMENTS

by

Joshua J. Knechtel

A thesis submitted in partial fulfillment of the requirements for the degree of

Master of Science

in

Materials Engineering

Department of Chemical and Materials Engineering

University of Alberta

ABSTRACT

The goal of this investigation was to study hydrogen-facilitated fatigue crack growth behaviour on pre-existing cracks in a full-scale specimen exposed to a near-neutral pH (NNpH) environment. The full-scale specimen used in this study was a 4.77 m segment of NPS 18, SCH 10, X-60 gas transmission steel pipeline. The segment was cut-out after 46 years of service when multiple stress corrosion cracking (SCC) colonies were discovered during an integrity assessment. A novel corrosion cell was developed to encapsulate portions of the pipe segment containing some of the SCC colonies; the remainder were exposed to atmospheric conditions. The corrosion cell was sealed, and the bulk solution was purged with a 5 % CO_2 + 95 % N_2 gas mixture for the duration of the test to maintain a pH of 6.29 and an anaerobic environment. To eliminate the effects of corrosion, -130 mV of cathodic polarization was applied to the fully exposed steel pipe, delivered by a custom impressed current cathodic protection system.

Constant amplitude and underload-type variable amplitude loading schemes were designed to simulate conditions commonly seen in the field. The maximum stress throughout the full-scale test and the frequency of the major loading events in each loading scheme were set at fixed values of 310 MPa (75 % SMYS) and 10^{-3} Hz, respectively. After completion of the 91-day test, destructive analysis found that 2.5 % of the total cracks examined exhibited re-initiation and growth. It was found that the threshold stress intensity factor (K_{th}) required for re-initiation and growth in the depth direction for the NNpH and atmospheric environments were ~ 18 and ~ 25 MPa√m, respectively. The average crack growth rate in the former environment was determined to be 2 – 3 times greater than the latter. It should be noted that this threshold is only valid for the loading conditions of the full-scale test. Four dents were machined into sections of the pipe with no pre-existing cracking in an opportunistic study of NNpHSCC initiation in dents. After test completion,

magnetic particle inspection was conducted in the areas surrounding the dents and no cracking was found.

The total measured crack growth attributed to the full-scale test was significantly less than expected. The primary cause was attributed to conservative reporting of the pre-test crack depths, where the depths reported by ECHO-3D were at least 30 – 40 % deeper than what was found by destructive analysis. This error was significantly larger than the maximum allowable manufacturer specification and the pressure fluctuation design did not account for such a large error in the pre-test crack depth measurement. Consequently, crack re-initiation did not occur at the start of the test and significant uncertainty regarding the moment of crack re-initiation was introduced; thereby impacting the discussion of this study and severely limiting the findings related to the original research objectives.

PREFACE

Part of this work involved research collaboration. Results presented in **Section 4.3.1.1** were obtained by Dr. Zhezhu Xu, under the supervision of Dr. Weixing Chen. Dr. Weixing Chen is a professor in the Department of Chemical and Materials Engineering, University of Alberta and is the supervisor of Dr. Zhezhu Xu who is a Postdoctoral Fellow in the Department of Chemical and Materials Engineering, University of Alberta. All other parts of this thesis are the original work of the author.

DEDICATION

This work is dedicated to three individuals who have had great impact on my growth and development. First, to my parents Lew and Colleen Knechtel. Their support throughout my education has pushed me to achieve my goals. Finally, to my partner Stephanie Keats, who I am truly grateful for in more ways than words can convey.

It doesn't get easier; you just get better at it.

ACKNOWLEDGEMENTS

TABLE OF CONTENTS

LIST OF FIGURES

LIST OF TABLES

LIST OF ABBREVIATIONS

A&B	Arnett & Burgess
AB	Alberta
AC	Alternating Current
AER	Alberta Energy Regulator
BSE	Backscattered Electron
CA	Constant Amplitude
CEPA	Canadian Energy Pipeline Association
CER	Canadian Energy Regulator
CF	Combined Factor
CGSB	Canadian General Standards Board
CME	Chemical and Materials Engineering
CP	Cathodic Protection
CSE	Saturated Copper/Copper Sulphate
CT	Compact Toughness
EAC	Environmentally Assisted Cracking
EAS	Earth and Atmospheric Sciences
EDPM	Ethylene Propylene Diene Terpolymer
EG	Enviro-Grit
EMAT	Electromagnetic acoustic transducer
EMF	Electro-Magnetic Field
FBE	Fusion Bonded Epoxy
HAC	Hydrogen Assisted Cracking
HE	Hydrogen Embrittlement
HEDE	Hydrogen-enhanced Decohesion
HELP	Hydrogen Enhanced Local Plasticity
HIC	Hydrogen Induced Cracking
HpH	High pH
HpHSCC	High pH Stress Corrosion Cracking
ID	Inner Diameter
ILI	In-line Inspection
LIBS	Laser Induced Breakdown Spectroscopy
LME	Liquid Metal Embrittlement
MC	Minor Cycle
MFL	Magnetic Flux Leakage
MPI	Magnetic Particle Inspection
NDE	Non-Destructive Examination
NEB	National Energy Regulator
NNpH	Near Neutral pH
NNpHSCC	Near Neutral pH Stress Corrosion Cracking
NPT	National Pipe Thread
OCP	Open Circuit Potential
OD	Outer Diameter

OES	Optical Emission Spectroscopy
OL	Overload
OM	Open Mouth
PAUT	Phased Array Ultrasonic Testing
PCS	Pressure Control System
PL	Petro-Line
PLI	Pipeline Integrity
PPE	Personal Protective Equipment
PT	Pressure Transmitter
PVC	Polyvinyl Chloride
SCADA	Supervisory Control and Data Acquisition
SCC	Stress Corrosion Cracking
SCT	Surface Crack Tension
SE	Secondary Electron
SMAW	Shielded Metal Arc Welding
SMP	SCC Management Program
SMYS	Specified Minimum Yield Strength
SW	Shear Wave
UL	Underload
UPS	Uninterruptible Power Supply
UT	Ultrasonic
XRD	X-Ray Diffraction

CHAPTER 1: INTRODUCTION

Near-neutral pH stress corrosion cracking (NNpHSCC) was first reported in 1985 [1, 2] by a Canadian pipeline operator, and is still a challenge to pipeline operators around the world today [3]. It is well known that failure of the pipeline coating proceeds the initiation of NNpHSCC, and approximately 95 % of cracks become dormant at depths less than ~ 1 mm [4]. However, entire pipeline integrity (PLI) programs are required to manage the remaining 5 % that exit dormancy. Modern PLI programs use many tools to manage NNpHSCC from traditional methods like hydrostatic testing to emerging technologies such as in-line inspection [5]. One of the challenges these programs face is determination of the remaining life of pipelines susceptible to NNpHSCC. Improving these predictive tools will not only reduce the economic losses for pipeline operators, but more importantly, will reduce the impact of oil and gas activity on public health and safety and the environment.

After 35 years of extensive research, the physical processes of NNpHSCC initiation and growth produced in a laboratory environment have been determined [6]. As discussed in the Literature Review (**Chapter 2**) of this work, it has been established that Stage 1 NNpHSCC is driven by dissolution during initiation and at the crack tip. Once the crack reaches a threshold dimension, the growth becomes driven by hydrogen-facilitated fatigue (Stage 2 NNpHSCC). Predictive models for Stage 2 NNpHSCC have been proposed based on experimental results produced with constant amplitude loading conditions using compact toughness specimens [7]. However, these models do not translate well to the variable conditions in the field.

Therefore, the current study was performed to establish a deeper understanding of Stage 2 NNpHSCC re-initiation and growth. A full-scale test was designed and conducted to determine the effects of constant amplitude and underload-minor cycle pressure fluctuations on a pipe segment containing shallow, longitudinal SCC colonies, which formed while the pipe was in service. In order to simulate field conditions, a novel enclosure was developed to encapsulate selected portions of the pipe containing SCC colonies, while maintaining an anaerobic NNpH environment. Dents were machined in the pipe, isolated from any cracking or welds, in an opportunistic study of Stage 1 crack initiation on dents that are acceptable for service based on the applicable CSA Z662 criteria [8]. From the results of this study, a threshold stress intensity level

was determined for Stage 2 crack re-initiation and growth in a NNpH environment for the loading conditions of the full-scale test. Additionally, improvements regarding the full-scale testing experimental procedure have been recommended. The structure of the thesis is described in the following paragraph.

First, a review of pipeline integrity, non-destructive examination, the conditions generally known to precede NNpHSCC and the current understandings of NNpHSCC initiation and growth are given in **Chapter 2**. Second, the experimental methods used to design and carry out the full-scale test will be described in **Chapter 3**. Then, the results obtained from the full-scale test will be presented in **Chapter 4**. Next, in **Chapter 5**, the results of the full-scale test will used to discuss Stage 2 crack re-initiation and growth under variable loading conditions. Finally, the conclusions and recommendations for future work resulting will be summarized in **Chapter 6**, alongside the lessons learned from this work.

CHAPTER 2: LITERATURE REVIEW

The following chapter will provide a technical review of near-neutral pH stress corrosion cracking (NNpHSCC) characteristics and crack growth mechanisms. First, a brief overview of pipeline infrastructure in Canada and Alberta will be provided. Then, the recommended practices for SCC management will be introduced. Next, common non-destructive techniques and their application to pipeline integrity will be discussed. Then, fundamental principles of fatigue and environmentally assisted cracking will be established. Subsequently, the general conditions required for SCC, common preventative methods and the two types of SCC will be provided. Afterwards, crack initiation and growth in NNpH environments under various loading conditions will be detailed, the primary mechanisms of crack growth will be presented, and predictive models will be presented. Finally, the research objectives of the current work will be established based on the findings and discussion of this chapter.

2.1 PIPELINE INTEGRITY

The International Energy Outlook 2019 estimates that the global liquid fuels consumption will increase more than 20 % between 2018 and 2050, and the global natural gas consumption will increase by more than 40 % over the same time period [9]. A key takeaway from the report is that natural gas and petroleum consumption is rising in Asia faster than regional supply is growing, shifting focus to the import of Oil and Gas from other continents.

Oil and Gas in an integral part of the Canadian economy, and Canada is geographically situated to fill the increased demand on the world stage. In 2018, 21 % of Canada's revenue generated by exports of goods and services originated from energy products [10]. That same year mining, quarrying, and oil and gas extraction ranked third in their contribution of 7.9 % towards Canada's gross domestic product [11]. Alberta remains the largest producer of natural gas and crude oil and equivalents in Canada. **Figure 2.1** shows the breakdown of Canada's Oil and Gas production by province.

In the most recent annual Pipeline Performance Report prepared by the Alberta Energy Regulator (AER), a total of 433 000 km of pipelines have been built in Alberta, mainly consisting of steel pipelines (86 %) [12]. Of the total steel pipelines built in Alberta as of 2018, 255 000 km were

operating, while the remaining 115 000 km were discontinued or abandoned. As of 2016, there were 263 000 km of steel pipelines operating and the remaining 99 000 km were discontinued or abandoned. It should be noted that between 2016 and 2018, there was a 3.0 % decrease in the amount of operating steel pipelines.
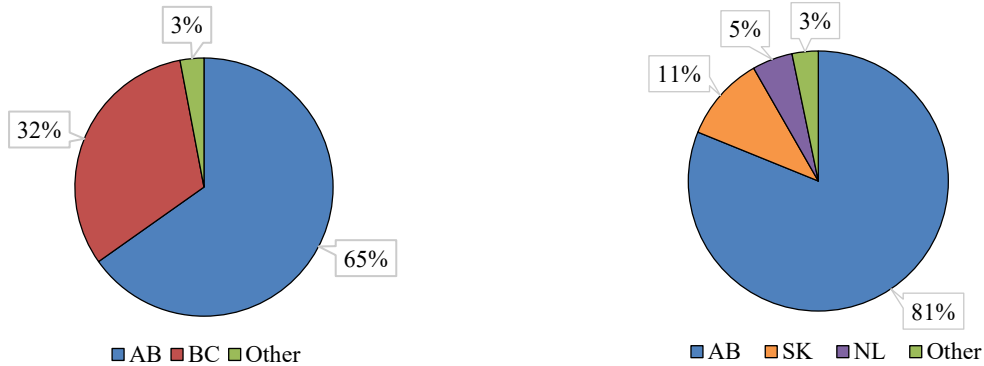
Figure 2.1 (Left) the total marketable natural gas production in 2018 [13] and (right) the total estimated production of Canadian crude oil and equivalents in 2018 [14].

In 2018, the total production of natural gas and crude oil and equivalents transported by steel pipelines in Alberta was 298×10^6 m^3 per day and 591×10^3 m^3 per day, respectively [13, 14]. This was a 3.6 % increase in transportation of natural gas and a 20 % increase in transportation of crude oil and equivalents from 2016 to 2018 [15, 16]. Coupling the increased transportation demand over recent years with the decrease in available transportation infrastructure, it is critical that operators minimize any downtime that may occur from pipeline failures.

The Canadian Energy Regulator (CER), formally known as the National Energy Regulator (NEB), mandates that regulated Oil and Gas companies falling under the CER's jurisdiction must follow the Event Reporting Guidelines. The most severe incidents fall into the immediately reportable events category. This category includes incidents that harm people or the environment, ruptures or toxic plumes. A pipeline rupture is defined by the CER as "an instantaneous release that immediately impacts the operation of a pipeline segment such that the pressure of the segment cannot be maintained" [17]. The primary causes of CER-regulated pipeline reportable ruptures from 1992 – 2012 were cracking (34 %) and metal loss (28 %) [18]. A distribution of the total primary causes of rupture failure of CER-regulated pipelines is shown in **Figure 2.2**.

4

Cracking is the primary cause of rupture for CER-regulated pipelines and is a major concern for Oil and Gas operators and **Figure 2.3** shows the occurrence of these ruptures. The sub-causes of cracking are hydrogen induced cracking (HIC), fatigue and stress corrosion cracking (SCC). There has been a gradual decline in annual ruptures since 1994 (except for 2009), which can be attributed to the mandated development of pipeline integrity and mitigation programs that Oil and Gas operators must meet [18]. For example, the Canadian Energy Pipeline Association (CEPA) has published a recommended practice for SCC management. Within this document is a series of investigative methods that can be used to develop an SCC investigative program. The three methods of detection that will be discussed are hydrostatic testing, in-line inspection and direct assessment.
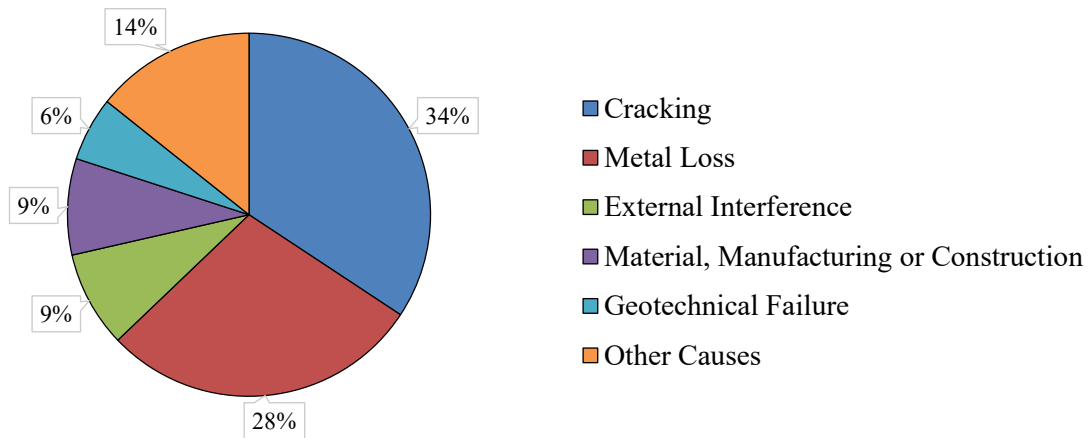
Figure 2.2   Distribution of the primary cause of CER-regulated pipeline ruptures from 1992 – 2012.
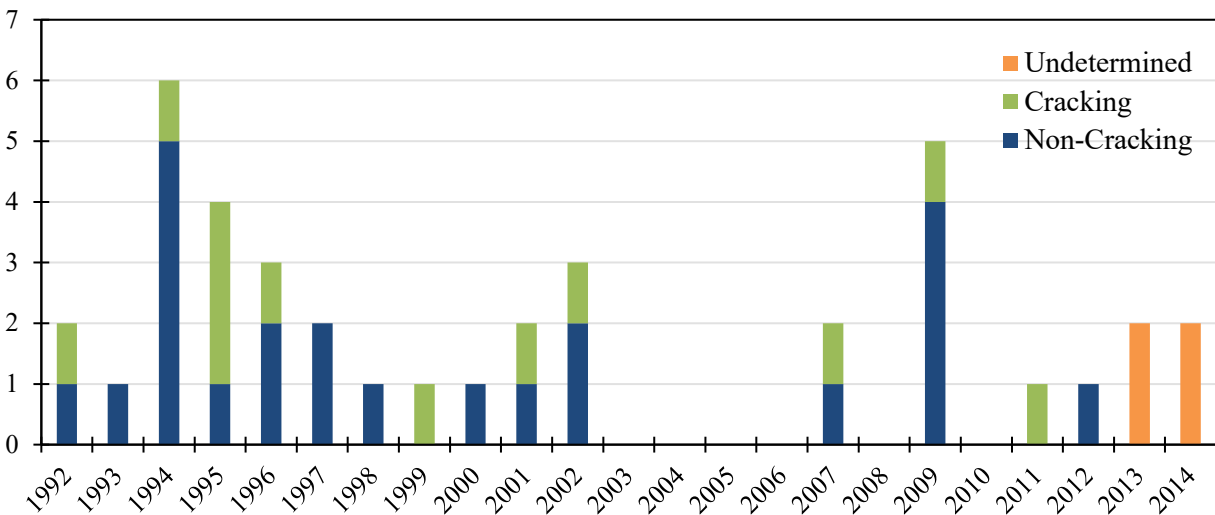
Figure 2.3   Number of ruptures on CER-regulated pipelines from 1992 – 2014.

5

2.1.1 HYDROSTATIC TESTING

Hydrostatic testing is a classic method to assess for SCC and the use of a hydrotest for the purpose of SCC detection is defined by CEPA as follows [5]:

> An SCC hydrotest […] can be a valid way of determining whether SCC, of a minimum size that will fail the hydrotest, exists on a susceptible pipe segment. An SCC hydrotest can provide data for a large length of pipe with the added benefit of verifying the pipeline integrity of this pipe length against an SCC failure for a period of time.

While hydrostatic testing has a proven track record as a successful integrity management tool, it has fallen out of favour with Oil and Gas operators. The main drawback of this detection method is that it can only identify SCC colonies above the detection threshold of the test, and it is impossible to rule out the presence of any SCC colonies with dimensions below that threshold. Additionally, a hydrotest requires a substantial amount of down-time for purging the line, conducting the test and removing the hydrotest fluid, which is costly to the operator. Finally, it has been shown that hydrostatic testing can reactivate small dormant cracks to grow to a larger size [19] effectively decreasing the remaining lifetime of the pipe segment by a significant amount of time.

2.1.2 IN-LINE INSPECTION

In-line inspection (ILI) is a constantly evolving tool available to pipeline operators for their pipeline integrity (PLI) programs. There are currently two main crack detection technologies commercially available for SCC ILI runs: ultrasonics and electromagnetic acoustic transducer (EMAT). In addition, magnetic flux leakage (MFL) tools with circumferentially orientated magnets can detect some axially oriented cracks. However, ILI tools are not available for all pipeline diameters, and they are limited by physical constraints such as changes in pipe diameter and small radius bends in pipelines.

The main advantage ILI technology possesses over hydrostatic testing is cost efficiency. ILI tools can be inserted into an active pipeline and cause minimal disruption to operations. Additionally, an ILI tool can precisely identify the location of the SCC as well as its size and severity. It should be noted that the SCC sizing data ILI tool runs generate must still be validated by field inspections.

Each new generation of ILI tools offers improvements over the previous version, making this one of the most desirable options available to PLI programs.

2.1.3 DIRECT ASSESSMENT

Direct assessment is a type of engineering assessment that can be used to partially or completely fulfill the requirements of an SCC PLI program. CEPA outlines the use of direct assessment to manage SCC as the ability of the program to assess the severity of individual SCC features (Assessment 1), and to assess the need for immediate and future pipe segment mitigation due to the presence of SCC (Assessment 2) [5]:

> Assessment 1 has a well-defined scope and requires relatively non-subjective physical data such as SCC depth, SCC length, material properties and stress levels. However, the Assessment 2 has a much broader scope and incorporates both the results of the first assessment as well as more subjective variables such as quantification of SCC growth.

Direct assessment is developed where hydrostatic testing and ILI may not be possible. These types of programs constitute four iterative steps: pre-assessment, indirect surveys, direct examination and post assessment [20]. During the pre-assessment stage, regions of similar characteristics are grouped together, and the appropriate indirect inspection tools are chosen. Next, the indirect surveys are conducted. This step includes corrosion and terrain modeling and above ground inspections. After this data is processed, direct examination is conducted in the ditch to collect data and remediate the threats. This is known as non-destructive examination and will be discussed in detain in the following section. Finally, a post assessment is conducted to determine the program effectiveness and reassessment interval. Direct assessment is a complex tool but can be an innovative solution when applied appropriately.

2.2 NON-DESTRUCTIVE EXAMINATION

Non-destructive examination (NDE) is a critical part of pipeline integrity (PLI) programs. The ability to determine specific characteristics of a material, or whether the material contains irregularities without removing the asset from service reduces downtime for operators. The NDE methods most commonly used in the context of PLI are visual, magnetic particle, radiography, eddy current, ultrasonic, and optical emission spectroscopy. Some of these methods are qualitative and others are quantitative. This section will describe these methods and their application in PLI programs.

2.2.1 VISUAL

Visual examination is the observation of an item to detect the presence or absence of surface flaws. Visual examination should be the first NDE method applied, as it may help determine the most appropriate subsequent examination. Visual examination can be applied to PLI programs in many ways. For example, a visual coating inspection can be conducted to determine the overall level of coating disbondment. After coating removal, corrosion products can be visually identified during the pre-blast inspection. Once sandblasting is conducted to remove the corrosion product and expose the bare metal; weld misalignments, dents, etc. can be initially identified by visual examination.

The leading advantage of visual examination is that it can be applied at any point in time throughout an integrity assessment with productive results. The limitations of this method can vary depending on the type of assessment. The most challenging limitation is that the nature of this examination is qualitative, relying heavily on the training and experience of the inspector. Therefore, visual examination is an important first step in NDE activity but must be combined with other methods for a complete assessment.

2.2.2 MAGNETIC PARTICLE

Magnetic particle inspection (MPI) is used to locate surface and slightly sub-surface flaws in ferromagnetic materials. A magnetic field is applied to the inspection surface and discontinuities that lie transverse to the magnetic field can be detected [21, 22]. If a flaw is present in the induced magnetic field, it will cause a leakage field. The presence of this leakage field (and the presence

of the flaw) is detected using a magnetic particulate slurry. The particles are drawn to and held by the leakage field, showing the location of the flaw.

MPI used for PLI programs requires surface preparation of the pipeline steel to a NACE No. 2/SSPC – SP 10 surface finish by sandblasting [23]. Once the surface has been prepared, a white contrast paint is applied to the steel surface. Next, a black magnetic particle water-based slurry is sprayed onto the surface and a yoke generates a magnetic field that draws the black slurry to the surface and sub-surface flaws in the material using the principles described above. The yoke must be positioned both axially and circumferentially to detect flaws oriented in both directions.

MPI is a qualitative NDE technique and can detect surface and sub-surface flaws. Embedded or internal flaws in pipeline steel cannot be detected by MPI. Advantages of this inspection method are that it is inexpensive, it has a fast inspection speed and minimal training is required to produce consistent results. The most significant limitation is that flaws can only be detected perpendicular to the magnetic field, so it is critical to apply the field in multiple directions. Another limitation occurs when the operating temperature of the pipeline approaches 100 degrees centigrade. Evaporation of the water-based slurry prematurely halts the movement of the magnetic particles, reducing flaw detection capabilities. This can be solved by using an oil-based slurry; however, oil-based products present additional safety and environmental challenges of their own.

2.2.3 RADIOGRAPHY

Radiographic examination is the general term used when material is examined by penetrating radiation. Differences in density and thickness of the material cause varying levels of radiation to be absorbed. This radiation absorption is most often captured by radiation sensitive film [24].

Radiography is a qualitative NDE technique and can detect crack-like, planar and volumetric flaws throughout the volume of the material. For PLI programs, it is most often used for inspection of new reinforcement sleeve welds installed to repair defects in the pipe. Radiography is also used in new construction projects to verify the integrity of girth welds, and in steel mills to verify the integrity of the long seam welds. The main advantage of radiography is that it provides a permanent record of the full volumetric examination. The principle challenge is that it is a radiation hazard, requiring specialised safety training and evacuation of the test area. Additionally, the depths of the flaws are not shown, and the results require a high degree of skill to interpret properly.

2.2.4 EDDY CURRENT

Eddy current examination is based on the principles of electro-magnetic induction. An electric coil with high frequency alternating current (AC) flow is placed near the specimen. The AC flow generates and electro-magnetic field (EMF) surrounding the coil. The EMF causes eddy currents to flow in the specimen via electromagnetic induction. The eddy currents react with the specimen, generating an EMF that opposes the original EMF emitted by the coil. The results of this interaction affect the voltage in the coil and can be interpreted to detect flaws [25].

Eddy current examination is a quantitative NDE technique and can detect surface breaking defects [26]. The greatest advantage of eddy current is that specimen contact is not required. Other advantages are automation and speed. The most significant disadvantage of this technology in the context of PLI programs is that the magnetic particles used during MPI may cause inconsistencies in the data collected by the coil, rendering eddy current examination ineffective once MPI has been conducted. Other limitations of this technology are that the depth of penetration is limited and surface roughness (e.g. corrosion) can produce nonrelevant indications.

Eddy current examination is most used for boiler tube inspection. Applications of eddy current examination in the PLI industry are limited to emerging technologies. One of these emerging technologies, ECHO-3D by Athena Industrial Services, delivers EMF imaging by generating a hemi elliptical toroidal field below the sensor. The feedback is captured and processed using ECHO-3D software and the location, orientation and depth of a surface breaking defect can be determined. The use of multiple sensors gives this technology the potential to analyze dense crack colonies where traditional methods cannot. The manufacturer claims the technology can detect cracks longer than 19 mm with depths of $0 - 6$ mm $\pm$ 10 % [27].

2.2.5 ULTRASONIC

Ultrasonic (UT) examination applies the use of high frequency sound waves to detect flaws in a specimen [28]. The sound is generated in a probe by applying current to a piezoelectric quartz crystal. As the current passes through the crystal, it changes shape rapidly, generating vibrations or sound waves that travel outwards. The sound waves are transferred from the probe to the specimen with a couplant and travel through the material experiencing attenuation and reflection at interfaces. Finally, the sound wave returns to the probe and is analyzed to determine the presence of a flaw in the inspected area.

UT examination is a quantitative NDE technique and can detect surface breaking, embedded and internal flaws in the material. There are numerous advantages with this technology. It is accurate and sensitive to small defects. It is a fast way to inspect a large area via automation. It has immediate response and only requires access to one surface. The principal limitation to this technique is that it is heavily reliant on operator training and experience as proper interpretation of the signal is critical. Other limitations are that it requires contact with the specimen, and a couplant.

The straight beam UT technique introduces a UT wave normal to the specimen surface. The UT wave travels through the thickness of the material, reflects from the inner surface and returns to the probe. The thickness is calculated by analyzing the time it took the sound to travel through the specimen and return to the probe. This can be used to measure the material thickness and is a reliable way to locate laminations and assess the extent of internal corrosion in the pipeline steel. This can be done manually, or with an automated UT (AUT) system.

The angle beam UT technique introduces UT shear waves (SW) at an angle to the specimen surface. The SW can be used to pinpoint the exact location of the interface within the volume of the material. For manual UTSW scanning, a six dB drop in the signal is commonly used to determine the location of the flaws. Automated UTSW methods exist as well. For example, phased array ultrasonic testing (PAUT) is a technology where an array of small ultrasonic transducers are fired in sequence, or phase. This method can scan a local area without moving the probe by modifying the phase between the transducers. The probe is mounted to a robotic crawler and can scan the entire long seam weld of a pipe joint quickly. Manual UTSW has some advantages but PAUT is generally considered more accurate. For example, when examining an electric flash weld long seam the probe used for manual UTSW can be maneuvered to get the best angle to quantify flaws in the internal weld cap. However, when examining with PAUT, features in the internal weld cap of an electric flash weld cannot be seen due to the placement and immobility of the probe.

2.2.6 OPTICAL EMISSION SPECTROSCOPY

Optical emission spectroscopy (OES) is a method of positive material identification used to quickly determine the composition of pipeline steel in the field. Characteristic visible light is produced by supplying energy to atoms, exciting the outer shell electrons. The energies of the outer shell electrons on which OES is based can be substantially influenced by the surrounding atoms to which they are bonded [29]. As a result, these bonds need to be completely broken for the OES spectra to appropriately represent the elements present in the sample. This is achieved by supplying sufficient energy to vaporize and decompose a small portion of the sample into its component atoms, as well as to excite the atoms in this plasma. As the plasma cools, electrons recombine with atoms, emitting characteristic photons. The wavelength of the photon gives the identity of the element and the intensity of the photon is proportional to the number of atoms of the element present in the sample. Combining the wavelengths and intensity of the spectra, the composition of the sample can be determined.

The external energy is frequently supplied by striking an electrical arc to the surface of the sample under an argon shielded atmosphere. Calibration to a control sample of similar composition to the test material must be conducted before and after each test to ensure the detectors are in good condition. This application of OES is called 'spark testing' and is a proven technology in the Oil & Gas industry. It is known for its accuracy and field reliability; however, the spark testing unit is cart mounted with a large argon tank and testing is limited by is large and cumbersome size. Until recently, spark OES has been the only way to measure carbon content in alloys in the field.

An emerging technology called laser induced breakdown spectroscopy (LIBS) applies the same principles of OES as traditional spark testing using argon gas purge and calibration to a control sample. However, the power source of the unit has been replaced by a miniature, pulsed laser [30]. The battery powered unit focuses the laser beam on a small area of the sample for a short burst of time, instantaneously vaporizing the sample surface and generating the plasma used for characterization. The LIBS unit is handheld and portable, making it versatile in the field.

2.3 Mechanical Fatigue

Pipeline steel is generally designed for strength; however, when in operating service it is often limited by its mechanical performance under cyclic loads. Critical and subcritical crack growth occurs as a result of two competing mechanisms [31]: intrinsic damage mechanisms ahead of the crack tip and extrinsic shielding mechanisms behind the crack tip. Fracture mechanics has been a useful tool for characterizing crack growth by fatigue. The stable (K_i) and instable (K_c) fracture toughness of a material are given by:

$$K_i = \beta \sigma_i \sqrt{\pi a_i} \quad \textbf{Equation 2.1}$$

$$K_c = \beta \sigma_{fr} \sqrt{\pi a_c} \quad \textbf{Equation 2.2}$$

where σ_i is the initial applied stress, a_i is the initial crack length, σ_{fr} is the applied stress at fracture, a_c is the crack length at fracture and β is a geometrical factor. However, both equations have limitations. K_i tends to underestimate the residual strength as it does not consider instable crack growth near fracture. K_c tends to be conservative as a_c is not the crack length in the structure currently being evaluated and is difficult to determine. An engineering approach to solve the above problem is to define an effective toughness value (K_{eff}). Physically, **Equation 2.3** is in error as it is using initial crack size and the stress at fracture. However, it is considered acceptable as K_{eff} is constant for a given material.

$$K_{eff} = \beta \sigma_{fr} \sqrt{\pi a_i} \quad \textbf{Equation 2.3}$$

Plastic collapse should also be considered when studying mechanical fatigue. Fracture and plastic collapse are two competing processes than can each lead to failure. Failure by plastic collapse becomes favourable under specific conditions when the fracture toughness is high, or the crack dimensions are approaching zero.

When a material is subjected to cyclic loading conditions, subcritical crack growth can occur at stress intensity levels (K) much lower than the material fracture toughness ($K < K_c$) due to accumulated damage to the plastic zone ahead of the crack tip [32]. Crack growth in a material subjected to constant amplitude loading conditions can be separated into three stages: initiation, steady growth, and accelerated growth to fracture. These regions are shown in the log-log plot

13

(**Figure 2.4**) of the crack growth rate per cycle as a function of the stress intensity factor range, ΔK ($\Delta K = K_{max} - K_{min}$).
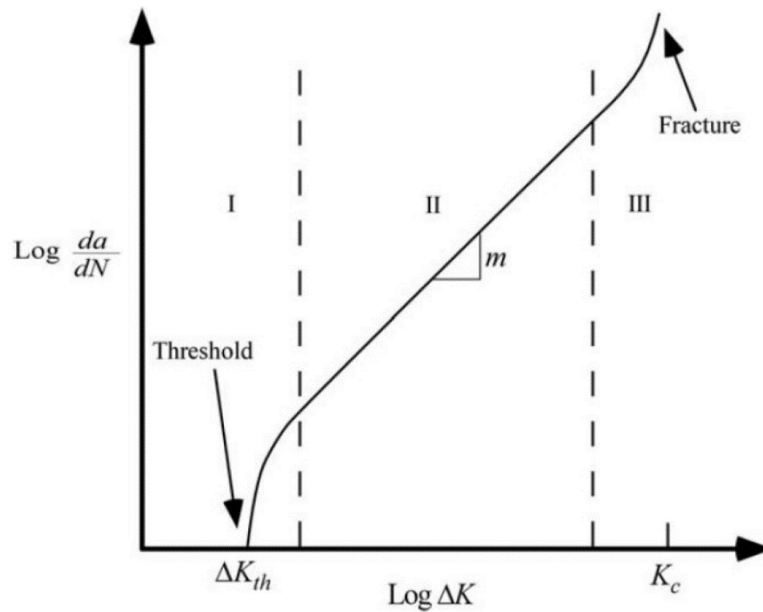
Figure 2.4 Typical fatigue crack growth in metals [32].

As shown in **Figure 2.4**, crack growth will only occur in Region I if a specific stress intensity threshold (ΔK_{th}) is met. For loading conditions where $\Delta K < \Delta K_{th}$, fatigue crack growth will not occur. Region II shows a log-log linear behaviour that is known as the Paris equation [33]:

$$da/dN = C(\Delta K)^m \quad \textbf{Equation 2.4}$$

where C and m are material constants in the range of $2-4$. Crack growth in the context of the Paris Law is only dependent on ΔK for a given material. Propagating cracks in Region II will generate small ridges perpendicular to the crack growth direction, known as striations. These ridges are formed by a repeated blunting and resharpening caused by shearing of the material ahead of the crack tip on slip planes oriented 45° to the crack plane [31]. Finally, the crack will enter Region III growth, where K_{max} approaches K_C of the material causing cleavage and/or micro-void coalescence to occur. Cracks in Region III will experience accelerated growth to failure in a short period of time.

While this model may predict fatigue crack growth rates under constant amplitude loading conditions accurately, predicting fatigue crack growth based on the Paris Law becomes

challenging when variable amplitude loading conditions are considered. The inevitable changes in loading patterns of pipelines, which deviate from constant amplitude conditions, can cause an acceleration (underloading) or retardation (overloading) effect on crack growth [34, 35] that the Paris equation can not account for. Additionally, the Paris Law is derived based on crack growth in a non-corrosive environment and does not account for the contribution of environmentally assisted cracking towards the overall crack growth rate.

2.4 ENVIRONMENTALLY ASSISTED CRACKING

Environmentally assisted cracking (EAC) is a challenging problem in many industries. EAC is a generic term referring to all forms of cracking in metals that is assisted by a chemical environment. There are four types of recognized EAC [32]:

i. **Stress Corrosion Cracking**

Stress corrosion cracking (SCC) refers to crack propagation that is driven by an anodic reaction at the crack tip. SCC is discussed in detail in **Sections 2.5 – 2.6**.

ii. **Hydrogen Embrittlement**

Hydrogen embrittlement (HE) is the weakening of a metal's bond strength due to the presence of atomic hydrogen at grain boundaries and interstitial sites in the crystal lattice. The presence of atomic hydrogen in the lattice can lead to crack propagation. HE can be classified in two sub-categories based on the method atomic hydrogen is supplied ahead of the crack tip. HE mechanisms are discussed in **Section 2.4.1**, and its contribution to corrosion fatigue is examined in **Section 2.6.2**.

iii. **Corrosion Fatigue**

Corrosion fatigue is the acceleration of mechanically driven fatigue failure in a corrosive environment compared to the fatigue life in an inert environment. Damage from corrosion fatigue results from a synergistic interaction between plastic deformation and electrochemical reactions at the crack tip. Corrosion fatigue is discussed in **Section 2.6.2**.

iv. **Liquid Metal Embrittlement (LME)**

LME does not normally involve an electrochemical corrosion reaction. Instead, LME can cause cracking when liquid metal penetrates the grain boundaries of another metal in solid state. Several alloy systems are susceptible to LME, including aluminum, titanium, stainless steel and nickel-based alloys. For example, zinc contamination of stainless steel occurs as a result of contact between galvanized parts and stainless steel at elevated temperatures. LME does not apply to this work and will not be discussed further.

2.4.1 HYDROGEN EMBRITTLEMENT

Hydrogen content at the external surface of pipeline steel after one to two years of service has been reported to increase by nearly one order of magnitude from baseline [36]. When hydrogen is introduced into steel, the toughness and ductility can be reduced, and subcritical crack growth can occur ahead of the crack tip [37, 38]. Atomic hydrogen reduces the cohesive bond strength between metal atoms, making fracture easier [32]. Hydrogen assisted cracking (HAC) can be divided into two categories based on the source of atomic hydrogen [39]: hydrogen environment-assisted cracking (HEAC) and internal hydrogen-assisted cracking (IHAC). In both forms of HAC, hydrogen is concentrated in the plastic zone ahead of the crack tip denoted as the fracture process zone (FPZ) in **Figure 2.5**. The high degree of stress in the FPZ causes the crystal lattice to expand, which increases the hydrogen solubility in that area. The hydrogen in the area causes embrittlement of the FPZ, resulting in microcracking when pressure fluctuations in the pipeline occur. The microcracks will coalesce with the main crack, resulting in crack growth. The rate of HAC is often controlled by the rate of hydrogen diffusion to the FPZ, obeying Arrhenius law:

$$D = D_o e^{-Q/RT} \quad \textbf{Equation 2.5}$$

where Q is the activation energy, R the gas constant and T is the absolute temperature. However, as temperature increases material susceptibility to HAC decreases, possibly due to the increased ductility of steel at higher temperatures [32].
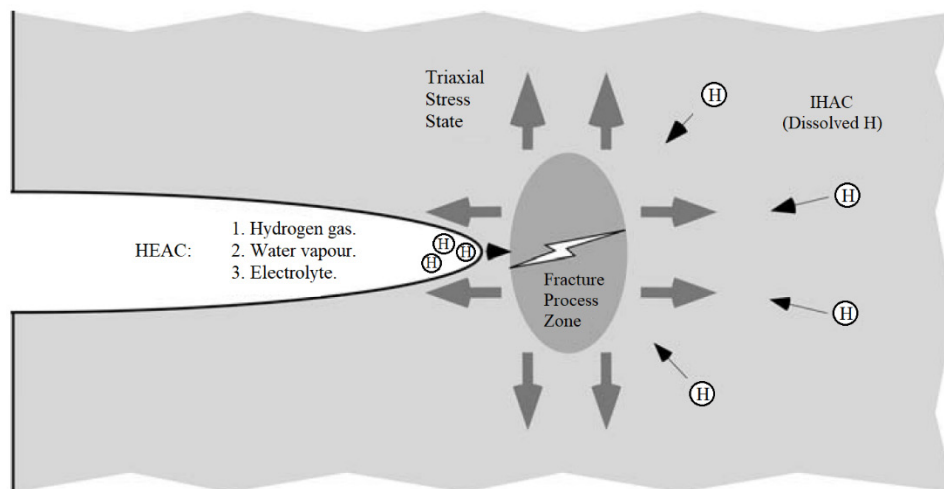
Figure 2.5   Schematic showing the two forms of hydrogen assisted cracking: hydrogen environment-assisted cracking (HEAC) and internal hydrogen-assisted cracking (IHAC) [32].

2.4.1.1 Absorbed Hydrogen Transport Mechanisms

In pipeline steels, hydrogen is known to degrade crack propagation resistance by assisting in the microscopic processes responsible for crack tip advance, while embrittlement reduces the fracture toughness [37]. Hydrogen degradation of the crack propagation resistance of pipeline steel is categorized as either HEAC or IHAC, which are distinguished by the source of hydrogen that causes cracking [39].

i. **Hydrogen Environment-assisted Cracking**

HEAC involves hydrogen entering the material at the crack tip through the conjoint action of mechanical loading and chemical reaction. Atomic hydrogen can be produced at the crack tip when gaseous hydrogen dissociates or by chemical reactions in the electrolyte near the crack tip. Once produced, the hydrogen diffuses into the FPZ if stress is applied. Diffusion of hydrogen ahead of the crack tip when there is no applied stress is negligible.

ii. **Internal Hydrogen-assisted Cracking**

IHAC occurs when there is dissolved hydrogen in the material. In the case of pipelines, hydrogen is generated by general corrosion at the external surface or from direct contact with the internal fluid. Eventually, hydrogen will diffuse through the thickness of the material reaching an equilibrium concentration. Loading causes the re-distribution of dissolved hydrogen to the FPZ, promoting crack growth.

2.4.1.2 Hydrogen Embrittlement Micro-mechanisms

The following will discuss two of the established hydrogen embrittlement micro-mechanisms in metals [40]:

i. **Hydrogen Enhanced Localized Plasticity**

Hydrogen enhanced local plasticity (HELP) was first introduced in 1990 [41]. HELP enhances the mobility of dislocations through an elastic shielding effect, locally reducing the materials shear strength, ultimately causing cracking by micro-void coalescence along preferred crystallographic glide planes. This fracture process is considered a highly localized plastic failure process, responsible for the plastic collapse of pipeline steel. HELP

is considered the governing mechanism for hydrogen-facilitated cracking of pipeline steels in NNpH environments [42].

ii.   Hydrogen-enhanced Decohesion

Hydrogen-enhanced Decohesion (HEDE) was introduced in 1960 [43]. HEDE refers to the theory that the atomic bonding ahead of the crack tip is weakened by expansion of the atomic lattice due to the presence of solid solution hydrogen, effectively lowering the bond strength. The increased concentration of solid solution hydrogen is caused by elevated local hydrostatic stress. This decohesion fracture initiates ahead of the crack tip, in the FPZ. This fracture process is responsible for the brittle fracture of pipeline steel.

2.5 SCC OF PIPELINE STEELS

A critical aspect of pipeline integrity programs is the implementation of an effective SCC management program (SMP). The cornerstone of the SMP is the application of an appropriate risk-based decision model. Each decision is based on an analysis of factors that influence SCC, with each factor having a level of uncertainty. These factors can be quantified to produce a probability of a given event such as SCC failure. This probability, when paired with an associated consequence rating system provides the overall risk related to that event. This risk is never zero; however, it is the operator's responsibility to ensure the level of risk remains acceptable [5].

The second fundamental concept of the SMP involves breaking SCC into lifecycle events and examining how often they may occur. Generally, SCC is broken into three sequential stages: crack initiation and early-stage crack growth in Stage I [44], steady state crack growth in Stage II [45], and rapid growth leading to final failure in Stage III. Typical crack management programs are designed to mitigate SCC prior to entering Stage III. As shown in **Figure 2.6**, the likelihood of SCC advancing to a more serious stage decreases at each level. Prior to discussing the stages of SCC, the conditions required for initiation must be introduced.
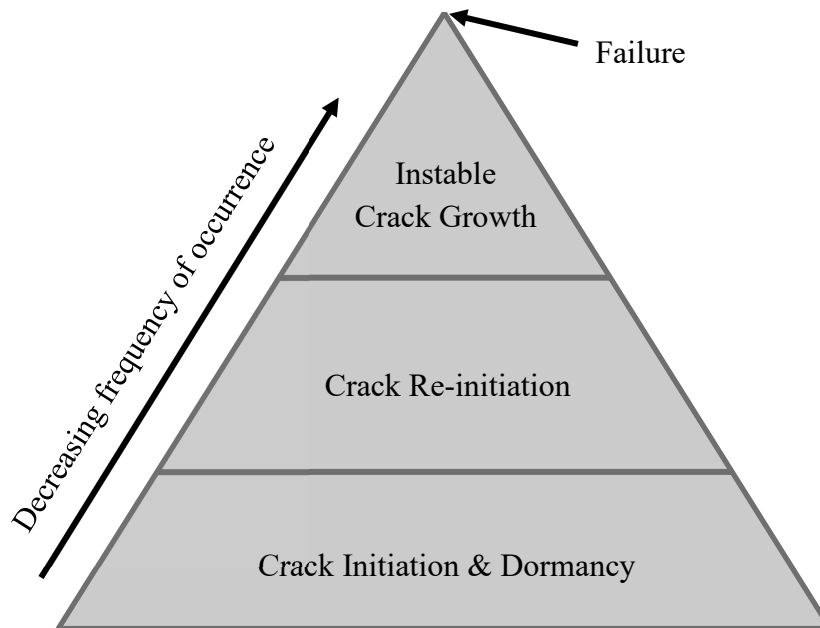
Figure 2.6 The frequency of occurrence of SCC lifecycle events [5]. Crack initiation and subsequent dormancy is the most common occurrence. Next, a fraction of the cracks will re-initiate after a period of dormancy. Finally, of the re-initiated cracks, one will enter the instable growth phase leading to failure.

20

SCC initiation in pipeline steel may only occur when three conditions are simultaneously present: susceptible material, tensile stresses present above a threshold value and exposure of the susceptible material to a potent environment. Pipeline steel has been shown to be universally susceptible to SCC [46]. Tensile stresses are generated by hoop stress from the internal pressure of the pipeline. The potent environment is the soil and electrolyte that surrounds the buried pipeline. The first and second conditions of SCC described above are always present for a pipeline under operation; the third condition is only present when ground water can reach the bare metal surface due to a failure in the pipe's external coating [47, 48]. Therefore, the extent of the coating disbondment plays a key role in SCC initiation and growth in pipeline steel.

2.5.1 COATINGS

Coatings can be applied to a pipeline prior to installation either during the manufacturing process, or at the construction site [49]. The effective application of a coating will create a barrier between the bare pipe surface and the corrosive environment. The following is a list of the characteristics that a coating should exhibit to successfully act as a barrier over the lifetime of the pipeline [5, 8, 50].

   i.   **Adhesion and Resistance to Disbonding**

   Coating adhesion and resistance to disbonding are primary performance properties that indicate a coating's ability to act as a barrier to the external corrosive environment. Coatings with good adhesive properties are less likely to be affected by soil expansion and contraction during changes in the soil moisture content or freeze and thaw cycles. Resistance to the downward forces of the surrounding soil as it settles after construction is critical as well.

   ii.   **Proper Surface Preparation**

   Proper surface preparation prior to coating application will increase adhesion and reduce the chances of disbondment. This is achieved by creating a clean, rough surface finish, which increases the surface area available for adhesive bonding. Additionally, removal of the mill-scale layer can reduce the effects of galvanic corrosion, in turn slowing early stage SCC growth [7, 51].

iii. Non-shielding to CP if Disbonded

If the coating does disbond, cathodic protection (CP) must have an electric path to the bare metal surface. Proper delivery of CP at the disbonded location is the second measure in place to prevent corrosion and SCC. Some coatings, such as polymer tapes, will disbond adhesively creating a gap between the coating and the bare metal surface where water can collect but CP cannot reach. High-integrity coatings will disbond adhesively (completely removed away from the pipe surface) and cohesively such that adequate CP can reach the disbonded area.

iv. Low Water Permeability

Water vapour transmission into the coating may cause disbondment and can lead to further accumulation of moisture at the metal surface. As the coating becomes saturated with water, its conductivity increases. This results in a higher drain in the CP system, reducing the electric current available for regions that have previously disbonded. This also causes higher electricity consumption costs.

v. Effective Electrical Insulator

Good electrical properties will limit the long-term exposure effects on the coating from the CP system. The insulating properties will also reduce the electric demand of the system. However, if the coating disbonds, it will shield the CP from reaching the exposed surface causing high levels of localized corrosion.

vi. Abrasion and Impact Resistance

Pipe contact with mechanical equipment or rocks could damage the coating. Good abrasion and impact resistance will minimize this damage.

vii. Temperature Effects and Ductility

Coatings must maintain ductility to resist cracking throughout a range of temperatures that it may encounter during transportation, handling by heavy machinery, bending, installation and during the pipeline's operation life.

viii. Resistance to Degradation

Coating degradation can be generally attributed to the soil type surrounding the pipe, as well as the pipe's operating temperature. Selecting the correct coating for a stretch of pipe that experiences similar soil type and operating temperature can reduce the degradation of the coating over time.

ix. Retention of Mechanical and Physical Properties

Coating properties may change over its lifetime in service. For example, polyethylene tapes may stretch over time, and ageing fusion bond epoxy (FBE) coatings may become brittle.

2.5.1.1 Effective Coatings

The effectiveness of preventing SCC initiation in pipelines is primarily related to three coating requirements. The first requirement is that the coating must prevent the corrosive environment from contacting the bare metal surface. The second requirement is the ability for current to pass through the coating if disbondments occur, protecting the disbonded regions from the corrosive environment that cause corrosion or SCC. The third requirement is that surface preparation prior to coating application should be carried out in a manner that reduces susceptibility to SCC initiation. Four types of coating are recommended for new construction projects: FBE, liquid epoxy and urethane, extruded polyethylene and multi-layer or composite coatings [5, 50, 52].

i. Fusion Bond Epoxy

FBE is a high-integrity coating with excellent bonding strength and is resistant to deterioration from CP, soil stress and chemicals. FBE coatings are heat-activated, chemically cured coating systems. While FBE may infrequently disbond due to osmotic blistering, the coating properties prevent cathodic shielding, thereby ensuring protection is maintained. During pipe surface preparation prior to coating application, the surface is grit blasted. This process imparts a compressive residual stress on the pipe surface, improving resistance to pitting and SCC initiation [53, 54]. FBE coated pipe has been known to resist SCC initiation when compared with asphalt or tape-coated pipelines in similar conditions. Another primary advantage with FBE coatings is that the coating does not hide any external surface defects; therefore, the steel surface can be visually inspected after it is coated.

ii.   Liquid Epoxy and Urethane

Liquid epoxy and urethane coatings are considered a high-integrity coating, meeting all three requirements discussed above. This coating requires the same surface preparation as FBE, and the same benefits from that process are realized. This coating type is used extensively as a repair coating on FBE-coated pipelines and for coating girth welds in new construction projects.

iii.   Extruded Polyethylene

Extruded polyethylene meets requirements one and three. It has good adhesive properties and surface preparation by grit blasting prior to installation make it an effective coating that promotes resistance to SCC initiation. However, if the outer shell is damaged and disbondment occurs, the shell will shield the exposed metal from CP. Usually the disbondment occurs at the polyethylene/mastic interface instead of the mastic/pipe interface. In these instances, the mastic has been found to provide corrosion protection on its own.

iv.   Multi-layer or Composite Coatings

Multi-layer coatings consist of an inner layer of FBE and an outer polyolefin layer held together with an adhesive. Composite coatings are layered with FBE and a polyethylene outer layer. Initial performance analysis of these coatings predicted CP shielding in the event of disbondment. However, in practice these coatings are extremely resistant to mechanical damage and adhesion failure.

2.5.1.2 Problematic Coatings

There are many coating types commercially available that meet some of the characteristics discussed in **Section 2.5.1**. While it is true that the more desirable characteristics a coating possesses, the more broadly applicable the coating will be; it does not indicate if the coating will be effective in preventing SCC initiation. Two coating types have shown historical evidence of SCC susceptibility and are not recommended for new pipe, joint or repair coating [5, 55]:

i. Polyethylene Tape

Pipelines with tape coatings have historically presented a high susceptibility to SCC. Tape coatings satisfy the first requirement established in **Section 2.5.1.1**, but generally do not satisfy the second and third requirement. Adhesion is critical to the effectiveness of tape coatings. If the coating disbonds from the pipe or tents on the girth weld or long seam weld, it will shield the exposed metal from CP. Furthermore, surface preparation is usually completed by wire brush cleaning. This surface preparation method does not have the same benefits as grit blasting. Additionally, the porous structure of the mill scale left behind underneath the coating after wire brush cleaning enhances anodic and cathodic differences, promoting localized corrosion [56]. Consequently, the coating installation process does not produce a pipe surface resistant to SCC initiation and disbondment will create the idealized environment for SCC initiation and growth.

ii. Bituminous Enamel

Bituminous enamel coatings such as asphalt and coal tar have a history of susceptibility to SCC. The enamel is the corrosion inhibiting portion of the coating and it is reinforced with various combinations of fiberglass or felt to strengthen the coating for handling. This coating type satisfies requirements one and two established in **Section 2.5.1.1**. However, surface preparation is traditionally completed with a wire brush cleaning, presenting the same limitations discussed for polyethylene tape. Coal tar coatings have been historically susceptible to intergranular SCC [55]. This correlation is likely because disbonded coal tar coatings do not completely shield CP and full cathodic shielding is a pre-requisite for transgranular SCC.

2.5.2 CATHODIC PROTECTION

Cathodic protection is defined as a technique used to prevent the corrosion of a metal surface by making that surface the cathode of an electrochemical cell [8]. As external corrosion and SCC are electro-chemical phenomena they can be prevented or mitigated by applying a negative potential, making the pipe surface a cathode. Through this process, the rate of corrosion (oxidation) at the pipe surface is reduced [52].

There are two types of CP systems: sacrificial anode and impressed-current. The sacrificial anode system uses an anodic material that is less noble than pipe steel on the galvanic series. When connected to the pipe, the sacrificial anode provides protection to the pipe against corrosion. The impressed current system utilizes an external power supply, called a rectifier, connected to the pipe to control the voltage between the pipe and an anode bed, making the pipe the cathode in the electric circuit. These two systems are illustrated in **Figure 2.7**.

Cathodic protection is the second line of defence implemented in pipeline integrity programs to protect against corrosion and SCC when the coating disbonds. However, if the exposed pipe is partially or completely shielded from CP, all conditions for SCC are present and initiation may occur. There are two forms of SCC that have been found in pipeline steels, which can be classified by the *pH* of the corrosive environment at the location of coating disbondment, or the method of crack propagation through the microstructure of the steel. Both forms typically present as parallel external cracks oriented in the longitudinal direction on a pipe that group together as dense or sparse colonies. Dense colonies exhibit a circumferential crack spacing less than 20 % of the pipeline wall thickness, while sparse colonies have a larger separation [3]. The two forms are Near-neutral *pH* (NNpH) SCC and High *pH* (HpH) SCC and extensive reviews of the two types of SCC can be found in the literature [2, 3, 5, 47, 48, 52, 55, 57-64]. The former will be discussed in great deal in the following sections, while the latter will be introduced briefly below.
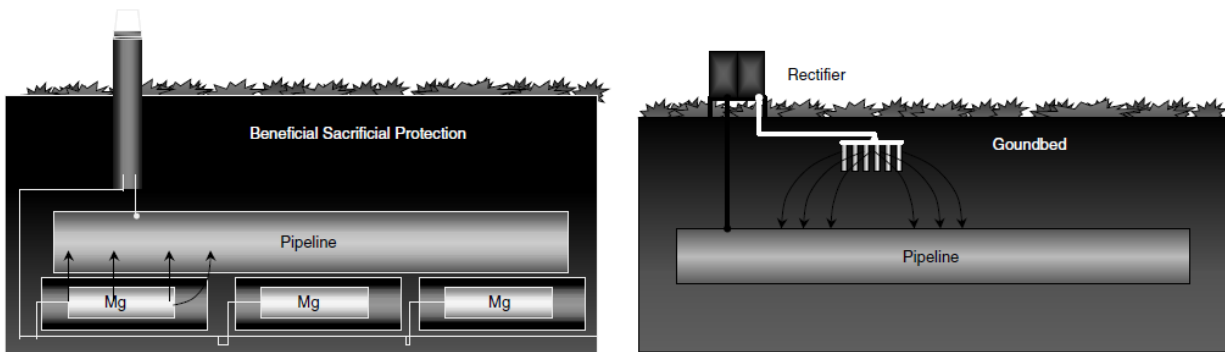
Figure 2.7   (Left) a sacrificial anode CP system with distributed magnesium anodes and an above-ground test station and (right) an impressed current CP system with an above-ground rectifier and a single remote anode ground bed [52].

2.5.3 HIGH PH SCC

The first recognized SCC failure on a pipeline occurred in 1965, when an intergranular form of cracking was observed that would later be named classical or High *pH* SCC [55, 57]. Colonies of HpHSCC are typically found where improperly cathodically protected pipeline steel is exposed to a high concentration solution mainly composed of carbonate (CO_3^{2-}) and bicarbonate (HCO_3^-) ions [58, 59]. The *pH* of these solutions typically range from 9.5 – 12.5 [60]. As some level of CP is present at these locations, HpHSCC is not typically found with external corrosion of the pipe surface. The cracks can become branched as the crack propagates along the steel grain boundaries (intergranular crack propagation), with little corrosion on the crack faces (**Figure 2.8**). The mechanism responsible for continuous crack growth has been well characterized by the repeated process of crack tip passivation and rupture of the passive film. In general, the average crack velocity is related to the crack tip strain rate [61, 62]. The study of crack growth rates has shown that HpHSCC is sensitive to temperature [63, 64]. It was found that a decrease in operating temperature led to a decreased probability of failure caused by HpHSCC.
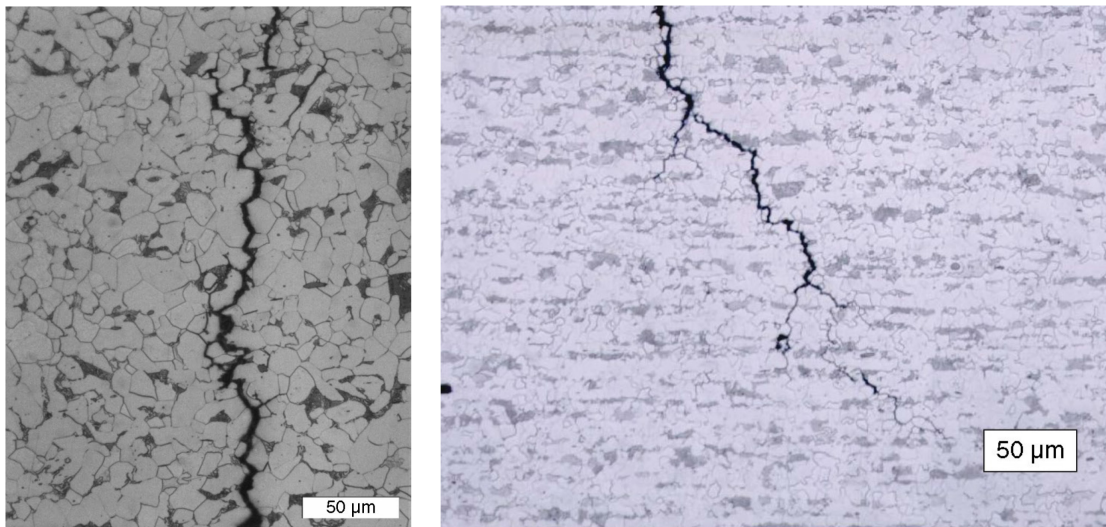
Figure 2.8   Cross sectional images of High *pH* stress corrosion cracks in a gas transmission pipeline [55].

The three stages of HpHSCC growth are often described by the bathtub model (**Figure 2.9**) proposed by Parkins [65, 66], where the crack velocity is plotted as a function of time. Prior to initiation, the conditions of SCC must be met. This usually involves pitting, and development of an aggressive chemical environment. Crack initiation (Stage 1) can be divided into two sections with respect to crack growth: (a) initiation by grain boundary selective dissolution [67] and (b) continuous initiation and microcrack coalescence. Pipeline steel spends most of its lifetime in Stage 1 SCC. Eventually, a threshold stress intensity value that will allow SCC (K_{ISCC}) is reached, and Stage 2 rapid growth begins. Finally, when the crack dimensions become severe, accelerated crack growth (Stage 3) begins, leading to abrupt failure. Stage 3 has little engineering significance as it cannot be controlled; pipelines should be replaced prior to reaching Stage 3 crack growth. The other form of SCC will be discussed in the following section.
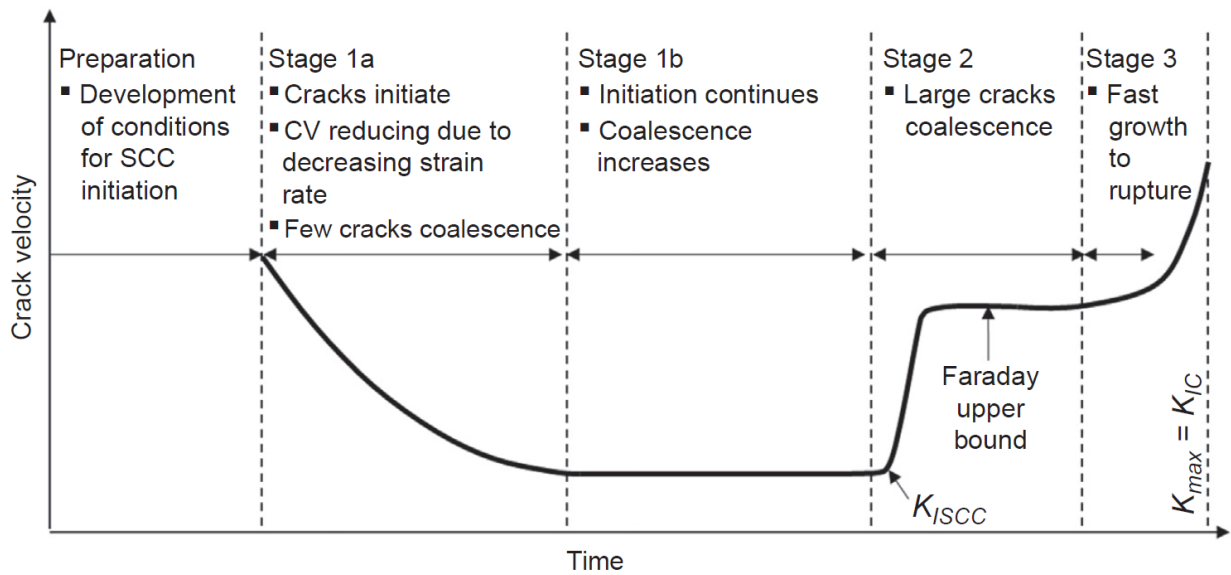
Figure 2.9   Visual representation of the stages of SCC growth during the lifetime of a pipeline failure [65, 66].

2.6 Near–neutral pH SCC

The second form of SCC was discovered in Canada in 1985, when cracking presented with some characteristics of HpHSCC, yet some differences [2]. It was noted that wide transgranular cracks with little branching were present and were associated with electrolytes with *pH* values of 7.5 or less [1]. Transgranular SCC, or near-neutral *pH* (NNpH) SCC occurs when the exposed metal surface beneath a coating disbondment is partially or completely shielded from CP. As the central focus of this work, the corrosive environment, corrosion mechanism, corrosion fatigue, crack propagation mechanisms, fracture surface characteristics and mathematical models related to NNpHSCC will be explored in detail in the following sections.

2.6.1 ENVIRONMENT AND CORROSION

As discussed in **Section 2.5**, one of the prerequisites for crack initiation is that the pipe surface is exposed to a potent environment. For this to occur, the soil electrolyte must penetrate the coating in a location where the pipeline surface is at least partially shielded from CP, near open circuit potential (OCP) condition. Coatings that disbond and shield the pipe surface from CP are most likely to promote NNpHSCC [2], and it has been shown that steel susceptibility to NNpHSCC increases with decreasing CP [68]. The *pH* level of the groundwater is dependent on CO_2 partial pressure, which is in equilibrium with bicarbonate ions in an anaerobic environment. The following will discuss the CO_2 corrosion mechanism of a NNpH environment.

2.6.1.1 CO_2 Corrosion Mechanism

The most important reactions which result in the CO_2 corrosion of mild steel are the electrochemical reactions occurring at the steel surface [69, 70]:

Water in the presence of dissolved carbon dioxide results in the formation of carbonic acid.

$$H_2O + CO_2 \leftrightarrow H_2CO_3 \qquad \qquad \textbf{Reaction 2.1}$$

Favourable dissociation of carbonic acid into bicarbonate occurs spontaneously.

$$H_2CO_3 \leftrightarrow H^+ + HCO_3^- \qquad \qquad \textbf{Reaction 2.2}$$

Anodic dissolution (oxidation) of iron at the metal-electrolyte interface occurs when a coating disbondment shields the metal surface from CP.

$$Fe \leftrightarrow Fe^{2+} + 2e^-$$ **Reaction 2.3**

Cathodic hydrogen evolution by reduction of dissociated hydrogen ions.

$$2H^+ + 2e^- \leftrightarrow 2H_{(ads)}$$ **Reaction 2.4**

Precipitation of iron-carbonate in solution.

$$HCO_3^- + Fe^{2+} \leftrightarrow FeCO_3 + H^+$$ **Reaction 2.5**

The overall reaction combining the above steps.

$$H_2O + CO_2 + Fe \leftrightarrow FeCO_3 + 2H_{(ads)}$$ **Reaction 2.6**

The rate limiting step to the reactions listed above is **Reaction 2.1**, which is controlled by the partial pressure of dissolved CO_2 (P_{CO2}). As the P_{CO2} increases, there is an increase in bicarbonate formation which increases the dissolution rate of steel in the corrosion cell. Conversely, as the P_{CO2} decreases, there is a shift in the equilibrium of the carbonate-bicarbonate system and the bicarbonate dissociation reverses, causing dissolution of the iron-carbonate. This equilibrium reaction, known as the Colwell-Leis mechanism, allows the generation of hydrogen in solution and formation of $FeCO_3$ while maintaining the *pH* of the bulk solution at approximately 6.4. Furthermore, this reaction forms a non-passive layer on the steel surface where active dissolution of iron takes place [70]. A visualisation of this equilibrium reaction is shown in **Figure 2.10**.

It is generally accepted that corrosion of pipeline steel under a coating disbondment is proportional to the CO_2 concentration. The level of dissolved CO_2 is homogenous in the soil electrolyte and near the open mouth (OM) of the disbondment. However, as CO_2 can only be replenished from the bulk solution, there is a decrease in concentration as the electrolyte moves further into the narrow disbondment. Recently, a second contributing factor to corrosion acceleration in small gap size disbondments was proposed [71]. It was theorized that as the concentration of Fe^{2+} increased, the corrosion rate at that location decreased. There is debate [72] regarding the mechanism causing this effect, as well as the location within the disbondment most affected. However, there is

agreement between the authors that an increase in local Fe^{2+} concentration within a coating disbondment will decrease the dissolution rate of iron at that location. A visualization of the Fe^{2+} concentration gradient theories is shown in **Figure 2.11**. The former author theorised a linear gradient decreasing from the OM, while the latter author theorized a peak concentration at the mid-way point of the disbondment. The results of a study of the crack width through the crack depth profile conducted by Egbewande *et al.* [73] shows the smallest width at the mid point of the crack depth; corelating with the theory proposed by Engel [72].
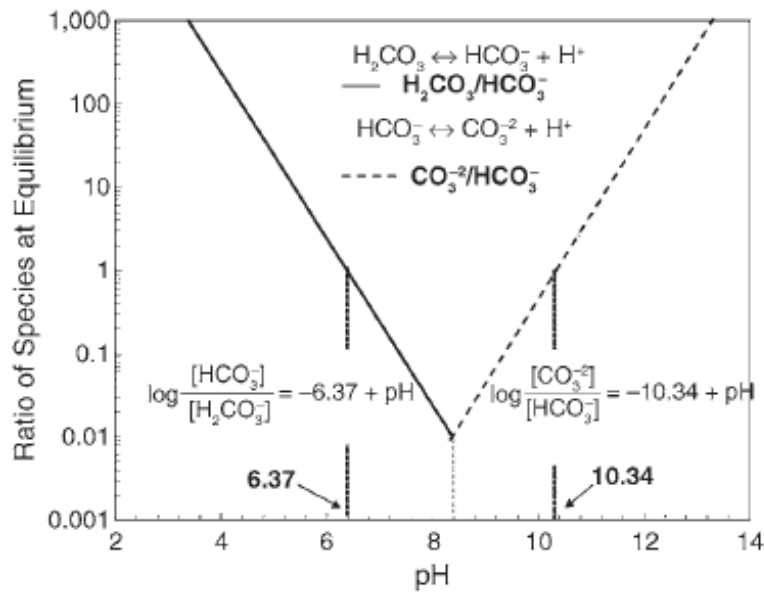
Figure 2.10   Calculated equilibrium constant values as a function of the ratio of species at equilibrium and [70].
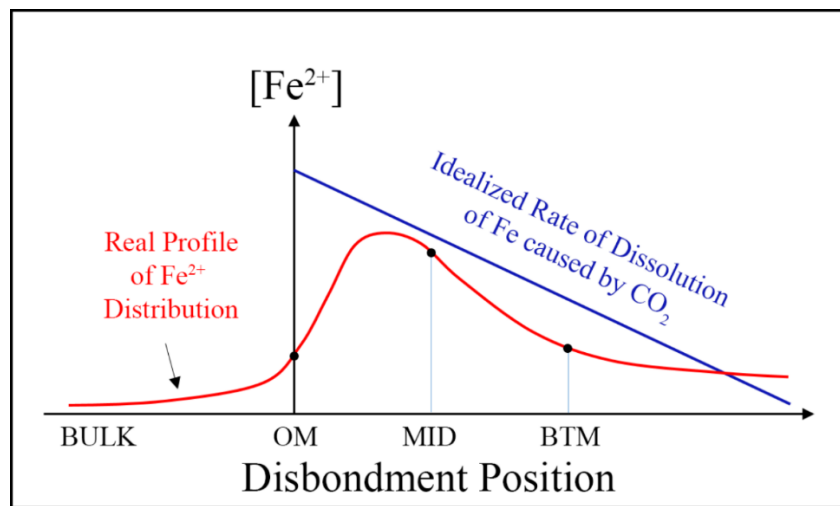
Figure 2.11   Iron distribution at various points of the coating disbondment within a corrosion cell [72].

Statistical analysis of field data shows that more than 95 % of SCC becomes dormant due to crack tip blunting at a depth of less than 1 mm [4]. In a pipeline steel NNpH environment system, crack dormancy is physically related to crack tip blunting, which is induced either mechanically or environmentally [73]:

i. Mechanically Induced Crack Dormancy

Mechanically induced blunting primarily occurs due to low temperature creep at the crack tip. Time dependent plastic deformation will reduce the sharpness of the crack tip, in turn reducing the stress intensity, K_{max}, at that location. If K_{max} is reduced below a threshold value, continuous crack growth cannot be sustained.

ii. Environmentally Induced Crack Dormancy

Environmentally induced blunting is primarily caused by the direct removal of material via dissolution at the crack tip. Sufficient blunting by dissolution is only possible in non-passivating corrosion systems, such as the NNpH environment. Environmentally induced blunting is typically seen in the early stages of crack growth and in high concentrations of CO_2 as shallow cracks still observe similar CO_2 concentrations as the bulk electrolyte. As the crack depth increases, the rate of CO_2 corrosion decreases at the crack tip and the blunting effect is lessened. Because the highest levels of CO_2 are at the crack OM, dissolution of shallow cracks may lead to the formation of pits.

2.6.1.2 Soil Conditions

There are no obvious known trends with respect to soluble cation concentrations of the soils analyzed in the field where NNpHSCC has been found on pipelines [55]. However, the presence of CO_2 and low concentrations of bicarbonates in solution have been established [70]. The generation of CO_2 in the field can be attributed to the decay of organic matter in the soil [74]. CO_2 concentrations vary seasonally with the highest concentrations in the winter months. Soil moisture content is also a key variable in producing conditions favourable for NNpHSCC. To study NNpHSCC initiation and growth, a realistic potent NNpH environment must be simulated under controlled conditions.

Chen *et al.* [75] initiated a study to determine the effect distinct chemical environments have on corrosion and crack growth rates. Additionally, an attempt to identify specific conditions that enhance environmentally driven crack growth to further understand crack dormancy effects was undertaken. The corrosion rate of a synthetic solution with set ion concentrations was studied and compared to commonly used NS4 solution and occasionally used NOVATW solution. Four variations of the synthetic solution were produced, with the only variation in the $CaCO_3$ (by extension CO_3^{2-}) content. An increase in $CaCO_3$ caused an increase in the solutions *pH* level when purged with 5 % $CO_2 + N_2$ gas leading to a decreased corrosion rate of steel exposed to the solution. Lower long-term corrosion rates were found in more concentrated solutions, which was attributed to a surface film formation that slowed the diffusion of the species required in the electro-chemical reaction. One of these solutions (C2 solution) was found to maintain a *pH* of 6.29 in equilibrium with the purged gas. Crack growth rates of C2 were compared with NOVATW (*pH* = 7.11) and it was found that crack growth in a C2 environment was three times larger than a NOVATW environment for the same loading conditions, but still at levels applicable to NNpHSCC.

2.6.2 CORROSION FATIGUE

The classical approach to mechanical fatigue, known as the Paris Law (**Section 2.3**), can be presented as the average crack propagation rate (da/dN) as a function of the applied stress intensity range (ΔK). However, there exists a variety of crack growth responses for material subjected to variable amplitude loading conditions and/or a corrosive environment that deviate from the Paris Law, which was based on experimental results obtained using constant amplitude loading conditions in an inert environment [33, 76]. The Unified Approach (**Section 2.6.5.2**) to mechanical fatigue considers both the amplitude (ΔK) and peak stress intensity (K_{max}). However, it also has limited application to crack growth sensitive to the loading frequency or when exposed to a corrosive environment.

Corrosion fatigue is defined as the harmful effect of an external chemical environment on one of the stages of damage accumulation leading to the fatigue failure of metals [76]. This damage results from the interaction of plastic deformation and local chemical or electrochemical reactions. There are four defined stages of corrosion fatigue. The first stage is cyclic plastic deformation, where basic principles of fatigue weaken the material. Next, microcrack initiation occurs in an accelerated fashion when the material is exposed to a chemical environment compared to an inert environment.

As microcracks coalesce to form a small crack, the third stage ensues. Finally, macro crack propagation occurs.

Corrosion fatigue can be classified into three categories: (1) cycle-dependent, (2) time-dependent and (3) time- and cycle-dependent. Crack growth in the first category is not loading frequency dependent, while the second and third categories are. Some of the time-dependent processes that contribute to the crack growth are [77]:

i. Surface passivation, or oxide film formation is a time-dependent process. However, this is not the case for NNpHSCC as the corrosion mechanism forms non-passivating corrosion products.

ii. Lower loading frequencies can cause higher crack growth rates per cycle as maximum hydrogen effects can be achieved when the loading rate is slow enough to allow maximum segregation ahead of the crack tip.

iii. The time-dependent process of room temperature creep can lead to crack tip blunting and mechanical damage to the material ahead of the crack tip in the plastic zone [39].

iv. Many other conditions can affect time-dependent crack growth positively or negatively such as temperature [64], interaction between the chemistry of the material and the environment [69], and electrolyte dynamics [75].

NNpHSCC has many competing considerations that contribute to the crack growth rate. Examining the physical crack growth rate mechanisms yields a more direct understanding. Generally, there are three physical crack growth processes that contribute to the crack growth rate [77]:

i. Dissolution at the crack tip only, which is primarily the dominant process of crack growth in the early stages when the cracks are shallow. As the crack deepens, the diffusion driven processes of CO_2 corrosion become rate limiting and this process becomes secondary.

ii. Micro-crack initiation and coalescence ahead of the crack tip through hydrogen embrittlement. This mechanism is the primary cause of crack growth following the initiation phase of crack tip dissolution.

iii.   Direct cracking caused by cyclic loading that results from pressure fluctuations during pipeline operation.

Further complications are presented when the loading rates observed during pipeline operation are considered. The loading frequency of pipelines is typically in the range of 10^{-1} to 10^{-6} Hz [78]. Additionally, the transport media must be considered as pressure fluctuations for oil media and gas media pipelines are drastically different [79]. Finally, the pressure fluctuations are dictated by many factors related to pipeline operation including unpredictable supply and consumption of the transport media, flow rate changes, planned pressure reductions for maintenance work, unplanned line outages and mid-point injections [80]. The aforementioned factors create variable amplitude pressure fluctuations within the pipeline that are difficult to control from an operations perspective and difficult to mathematically relate to the crack growth rate from a modeling perspective.

Since pressure fluctuations are the driving force behind crack growth in pipelines exposed to NNpH environments, many experimental studies have been conducted to determine the mechanisms of cracking under constant amplitude loading conditions [19, 73, 81-87] and recently under variable amplitude loading conditions [72, 88-93]. The effects of the stress intensity factor range, the maximum stress intensity factor, the loading frequency and variable amplitude pressure fluctuations have been studied.

2.6.2.1 Effect of ΔK

The stress intensity factor range, ΔK, has been identified as the most important factor in controlling and predicting fatigue crack growth. The three regions of mechanical fatigue crack growth, introduced in **Section 2.3**, are commonly found when testing corrosion fatigue. The steady state growth regime (Region II), defined by the Paris equation is exclusively dependent on ΔK. This relationship named the Paris Law has historically been applied to determine re-inspection intervals and perform remaining life calculations on engineering components.

Historically, most experimental tests have been conducted in Region II instead of Region I as the crack growth rate in Region I is so low at low ΔK that test durations are not practical [84-86]. This effect is enhanced by low loading frequencies and intermediate stresses used to simulate realistic field conditions. Recently, it has been found that pressure fluctuations with $\Delta K < \Delta K_{th}$ can contribute to crack growth in NNpH environments by causing a load interaction effect coupled with the large fluctuation events [72, 77, 78, 88] and will be discussed in **Section 2.6.2.4**.

2.6.2.2 Effect of K_{MAX}

The maximum stress intensity factor, K_{max}, is the dominating mechanical driving force responsible for fracture and is especially pronounced at low crack growth rates [76]. K_{max} is especially relevant to systems involving hydrogen embrittlement such as the NNpH environment. The amount of hydrogen able to diffuse to the plastic zone ahead of the crack tip dictates the severity of the embrittlement effect. K_{max} is directly proportional to the applied stress at the crack tip, and the equilibrium concentration of hydrogen in the stressed lattice (c_{eq}) ahead of the crack tip follows an exponential relationship with the hydrostatic stress at that point, defined by [77, 94]:

$$K_{max} = \beta\sigma_{max}\sqrt{\pi a} \quad \textbf{Equation 2.6}$$

$$c_{eq} = c_o exp\left(\frac{\sigma_{hyd}\Omega}{k_B T}\right) \quad \textbf{Equation 2.7}$$

where β is a geometrical factor, σ_{max} is the maximum applied stress of the pressure fluctuation, a is the crack length, c_o is the equilibrium concentration of hydrogen in the bulk material, σ_{hyd} is the hydrodynamic stress ahead of the crack tip, Ω is the partial molar volume of hydrogen, k_B is the Boltzmann constant and T is the absolute temperature.

In conclusion, K_{max} effectively merges the principles of mechanical fatigue and hydrogen embrittlement to weaken the plastic zone ahead of the crack tip, promoting crack growth.

2.6.2.3 Effect of Frequency

The effect of loading frequency, f, on crack growth in a NNpH environment is shown in **Figure 2.12**. When the frequency is higher than 10^{-3} Hz, f is inversely proportional to the crack growth rate per cycle. This trend can be explained by the increased time for hydrogen diffusion ahead of the crack tip, as described by **Equation 2.5**. Experimental work is generally conducted with loading frequencies higher than 10^{-3} Hz as the duration of experiments becomes impractical at low frequencies. The transition of crack growth behaviour at $f < 10^{-3}$ Hz will be discussed in **Section 2.6.5.5**.
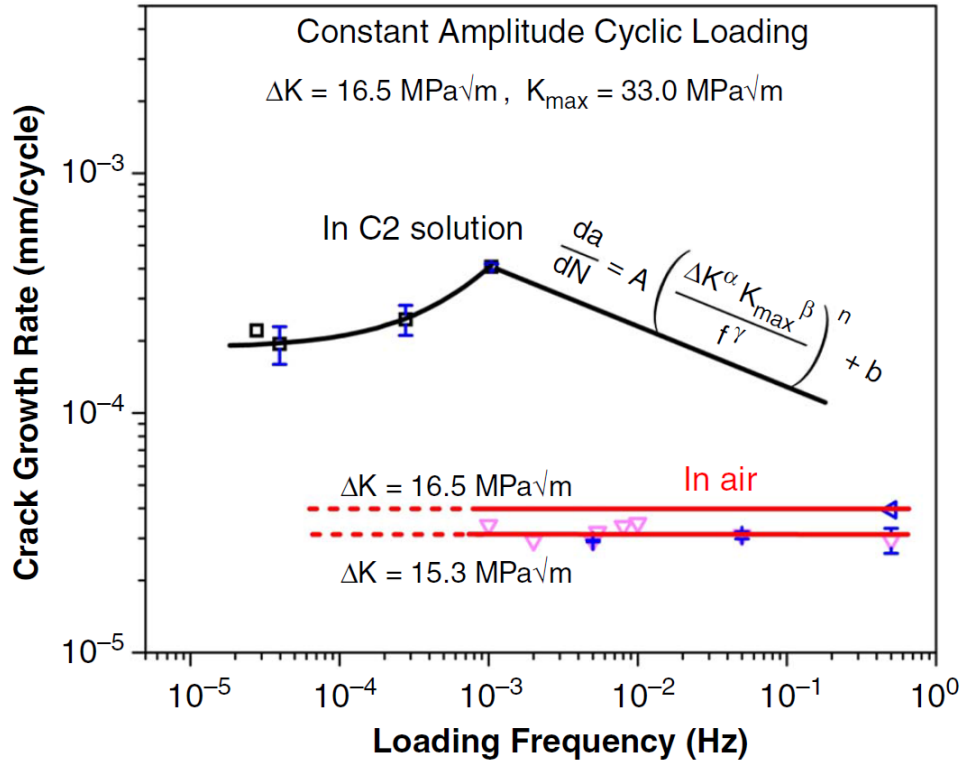
Figure 2.12   Crack growth rate as a function of the loading frequency of constant amplitude cyclic loading of CT specimens in C2 solution and in air [77].

2.6.2.4 Effect of Variable Amplitude Pressure Fluctuations

Variable amplitude pressure fluctuations can be categorized into three types, as shown in **Figure 2.13**: Type I – underload pressure fluctuations, Type II – mean load pressure fluctuations, and Type III – overload pressure fluctuations. Type I and III fluctuations are also accompanied by minor cycles, which have been shown to contribute to crack growth by the process of loading interaction [72, 77, 78, 88]. Additionally, these loading conditions can interact synergistically to promote crack growth or induce retardation effects [35]. A schematic showing the general trend of the interaction between some pressure fluctuation combinations is shown in **Figure 2.14**. The following will explore the effect of the varying types of pressure fluctuations on SCC growth rates in a NNpH environment.
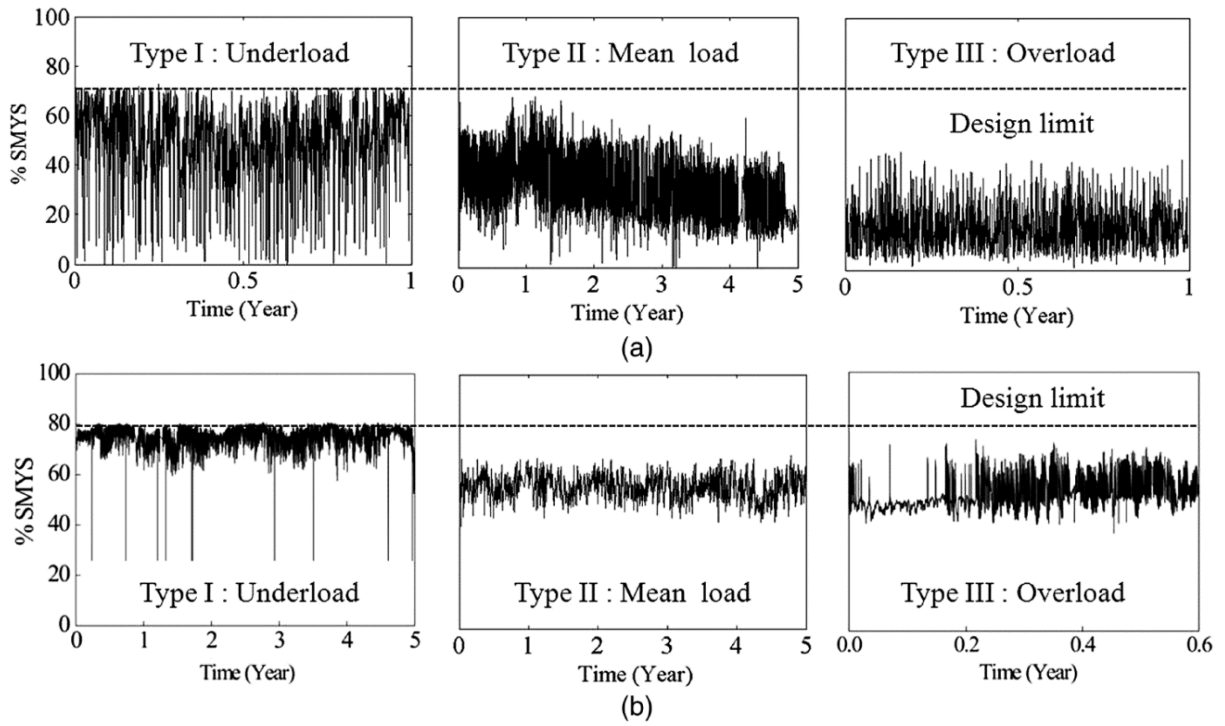
Figure 2.13 Classification of pressure fluctuation spectra of (a) oil pipelines and (b) gas pipelines [79].
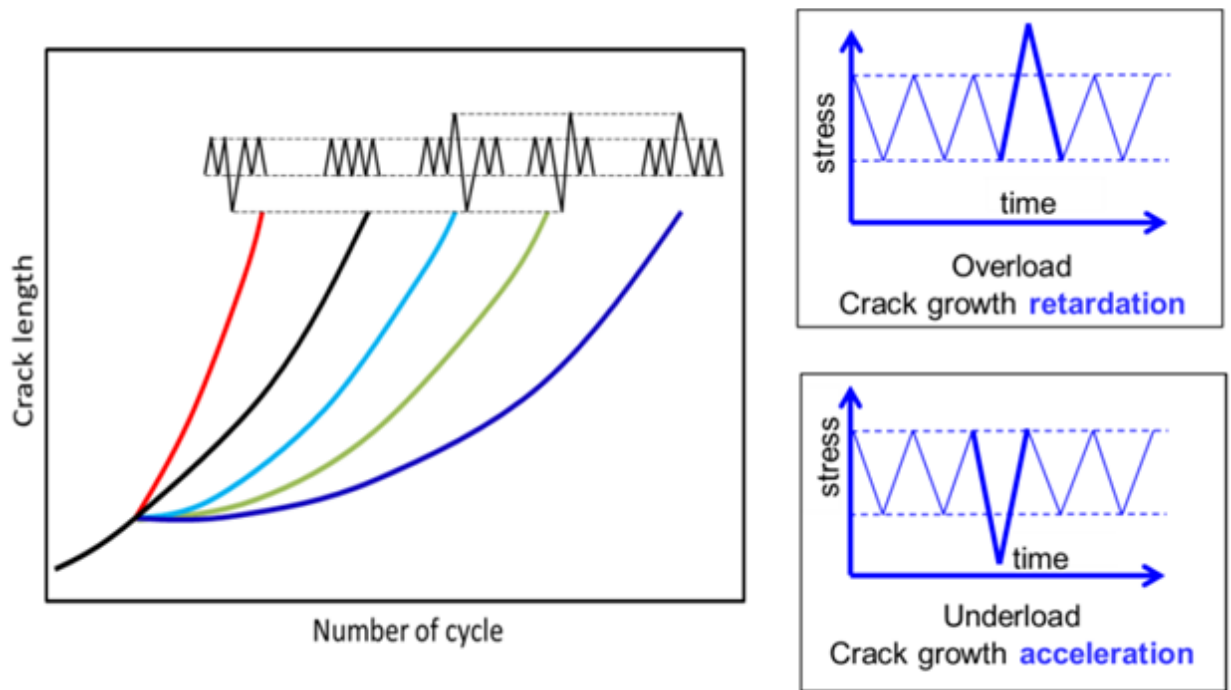
Figure 2.14 Generalized crack growth behaviour of various combinations of Type I and III pressure fluctuations, compared to the crack growth contribution of the minor cycles [79].

i. Type I – Underload Pressure Fluctuations

Type I pressure fluctuations are often found within 30 km of a compressor station (gas pipelines) or a pump station (oil pipelines) [79]. The maximum pressure of Type I fluctuations is often controlled close to the design limit of the pipeline, only allowing fluctuations at a level lower than the design limit. The spectrum consists of large fluctuation cycles with low R-ratios (underload cycles) separated by minor load cycles with high R-ratios (i.e. $R > 0.9$). This section of the pipeline is subjected to the highest mean pressures of the entire pipeline. Oil pipelines typically experience higher loading and unloading rates compared to gas pipelines due to the incompressibility of the transport media. Additionally, underloads in oil pipelines will often have lower R-ratios and higher occurrence of underload cycles. Type I fluctuations are the most concerning for crack growth due to the high mean stress and the accelerating effect of the underload (UL) cycles, as illustrated in **Figure 2.14**.

ii. Type II – Mean Load Pressure Fluctuations

Type II pressure fluctuations are typically observed further downstream from compressor and pump stations [79]. The mean pressure of Type II fluctuations is lower than Type I fluctuations, where spikes at a level above the mean pressure but below the design limit are commonly seen. The mean pressure is still not low enough to eliminate the underload fluctuations typically seen in Type I. This loading regime is mainly comprised of large changes in pressure, without minor cycles.

iii. Type III – Overload Pressure Fluctuations

Type III pressure fluctuations typically occur near the suction site, at the furthest point from the compressor or pump station [79]. The mean pressure of Type III fluctuations is the lowest throughout the pipeline, where pressure spikes above the mean pressure, also referred to as overload (OL) cycles, become predominant while the occurrence of underload cycles is minimized. Like Type I fluctuations, the large loads are separated by minor cycles (MC). The low mean pressures of Type III fluctuations make this spectrum the least concerning, in addition to the crack growth retardation effects of the overload cycles, as illustrated in **Figure 2.14**.

Before discussing load interactions, the mechanisms of crack growth acceleration and retardation should be introduced. Consider a crack with a blunt tip exposed to a NNpH environment. If a Type I fluctuation occurs, the blunted crack can be forced closed by a compressive underload. As the crack re-sharpens, a tensile residual stress forms ahead of the crack tip. This effect can only occur if a crack is blunt and there is space between the crack faces, which is common in NNpHSCC as the corrosion reaction at the crack tip is non-passivating. Under these conditions, the underload can cause an acceleration of the crack growth. Now, consider a crack exposed to a NNpH environment that is experiencing active growth. If a Type III fluctuation occurs, the resulting crack blunting due to the increased stress at the crack tip causes the crack faces to move apart. Crack tip closure does not occur immediately following the overload, so crack growth may be momentarily higher for a short duration. Once the crack propagates a short distance into the overloaded zone, compressive residual stresses result in plastically induced closure, which can cause crack growth retardation [95].

Evidently, pipelines subjected to Type I pressure fluctuations experience the most aggressive crack growth rates because they have the highest K_{max} (or mean pressure), which is close to the design limit, as well as the largest ΔK and frequently occurring underload cycles [79]. It has also been determined that crack growth can be significantly enhanced by Type I fluctuations, as compared with Type II fluctuations, because of the effect of load interactions [96]. In **Figure 2.15** it can be seen that the Type I fluctuations have a growth rate nearly one order of magnitude higher than the than the Type II fluctuations under the same loading conditions. In fact, cyclic pressure fluctuations are one of the most important prerequisites for active crack growth in NNpH environments [81, 97]. In **Figure 2.16**, Engel [72] compared the data from various tests that were conducted using the same loading conditions (K_{max}, R, f and #MC), but varying waveform types. Again, Type I loading was shown to produce higher crack growth rates than Type II loading in both the surface and depth direction. Additionally, comparing Type I loading with the UL&H waveform shows the crack growth approximately doubles when minor cycles are introduced in the place of a static hold.
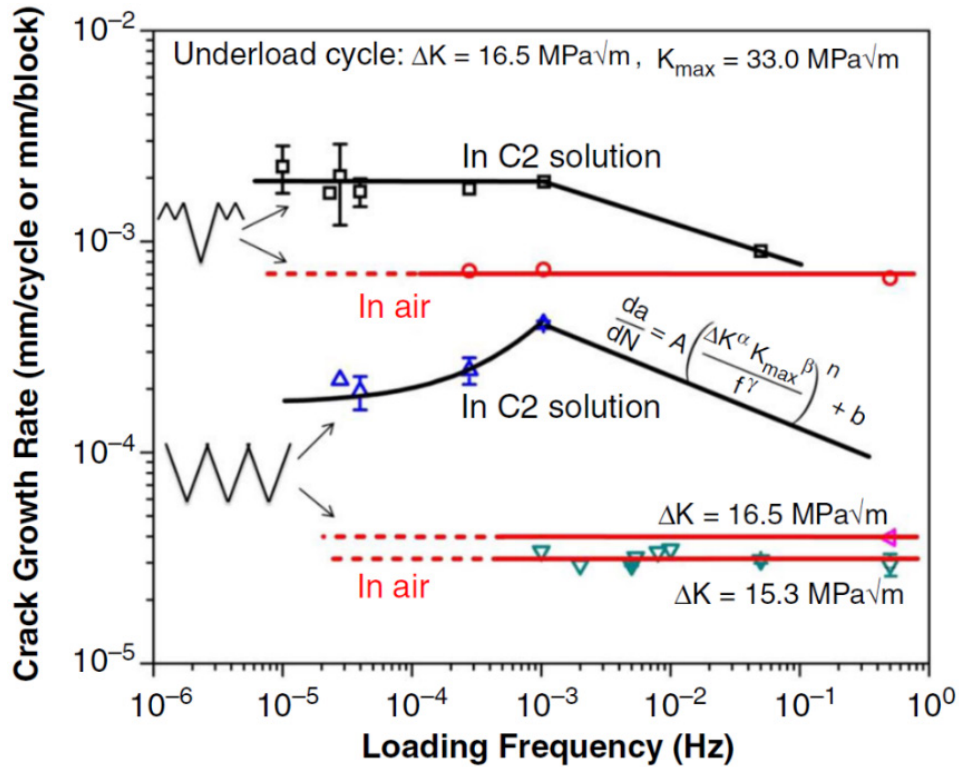
Figure 2.15   CT specimen crack growth rate of Type I and Type II fluctuations in C2 solution and in air over a variety of underload frequencies [77].
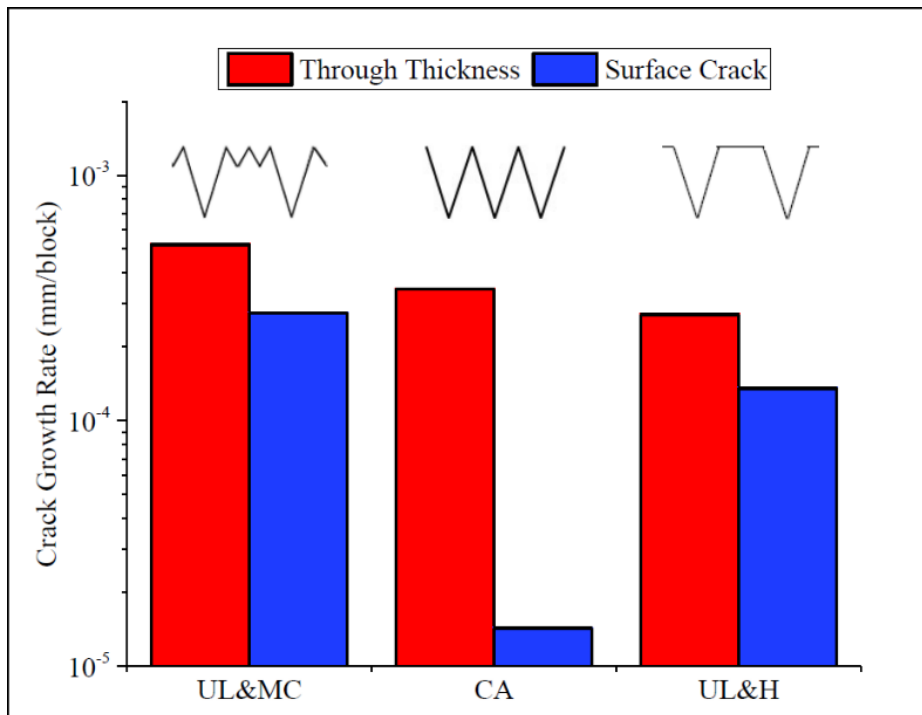
Figure 2.16   Log plot of the crack growth rate of CT [42] (red) and SCT [72] (blue) specimens under three loading conditions: (left) underload and minor cycle, (center) constant amplitude and (right) underload and hold.

The contribution of minor cycles to crack propagation via load interaction is shown in **Figure 2.17**. It is determined by dividing the crack growth rate of the respective mean load (i.e. Type I fluctuations) by the corresponding crack growth rate under constant amplitude loading. As indicated by **Figure 2.17**, increasing the number of minor cycles between each UL for Type I fluctuations will increase drive for crack propagation. It is also clear that when an OL is introduced prior to the UL, the crack growth rate is not sensitive to variation in the number of minor cycles. This indicates that applying an OL prior to an UL can reduce the contribution of subsequent minor cycles to crack growth. Based on the findings of this study, Tehinse *et al.* [88] recommended implementation of an overload with a magnitude no greater than 10 % of the minor cycles prior to an expected shutdown of a pipeline. This may reduce the acceleration affect caused by the depressurisation induced underload.
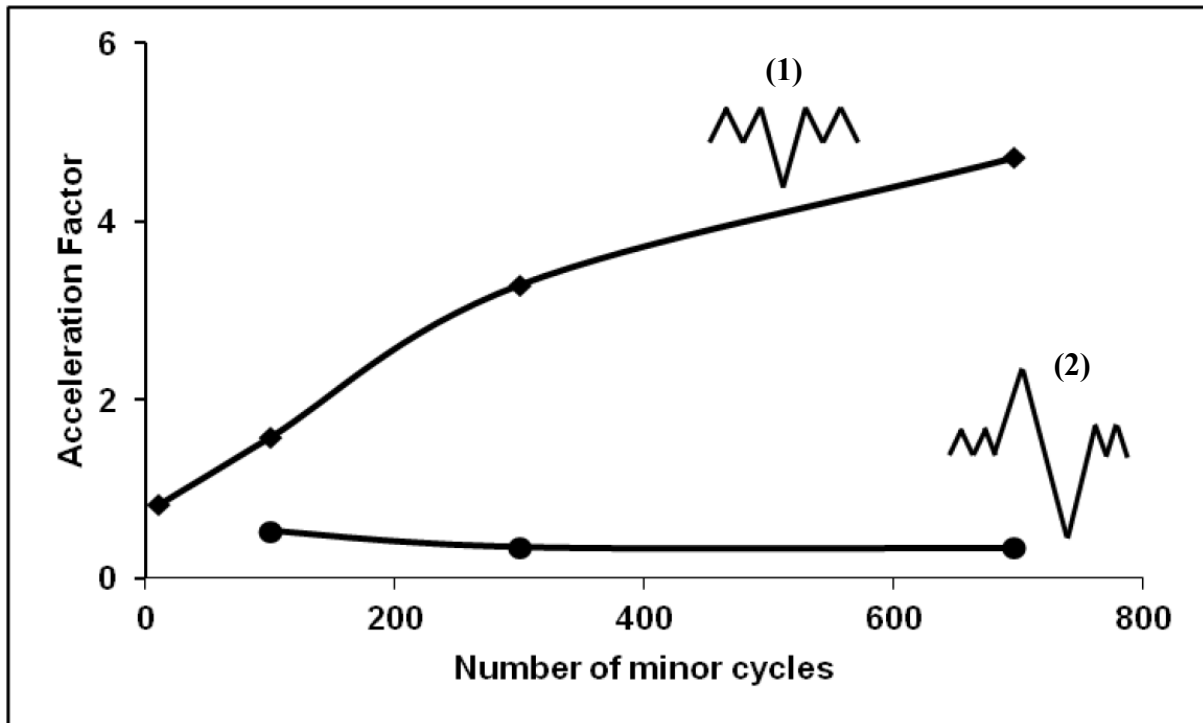
Figure 2.17   CT specimen crack growth rate showing the effect of the number of minor cycles on Type I fluctuation crack growth (1) and overload proceeding underload fluctuation crack growth (2) [88].

Zhao *et. al* [79] analyzed real pipeline pressure fluctuation data in an attempt to define the loading and unloading frequencies, number of underloads per year and number of minor cycles for oil and gas pipelines. A summary of the findings is shown in **Table 2.1**. The number of underloads experienced by oil pipelines is significantly higher than what is seen in gas pipelines due to the nature of the transport media. The loading and unloading rates of oil pipelines vary significantly, while they are consistently slow for gas pipelines. Finally, there are generally fewer minor cycles between underloads for oil pipelines than gas pipelines. The crack growth is predominantly driven by more frequent and larger underloads for oil pipelines, while it is driven by enhanced crack growth at lower frequencies and stronger load interactions in gas pipelines [96].

Table 2.1　　　Characteristics of Type I pressure fluctuations in oil and gas pipelines [79].

	Items	Oil pipelines	Gas pipelines
Underload cycles	Typical # of underload cycles per year	537	8
Frequency (Hz)	Range of unloading	$6.9 \times 10^{-6} - 1.0 \times 10^{-1}$	$1.3 \times 10^{-6} - 9.2 \times 10^{-5}$
	Range of loading	$5.1 \times 10^{-6} - 1.0 \times 10^{-2}$	$1.3 \times 10^{-6} - 5.3 \times 10^{-6}$
Minor cycles	# of MC between two underloads	$0 - 26$	$0 - 37$

2.6.3 STAGES OF NEAR–NEUTRAL PH SCC

After over 30 years of extensive investigation, the physical processes of crack initiation and growth in a NNpH environment have been determined [2, 55]. **Figure 2.18** shows the physical processes involved in crack initiation and growth for cracks exposed to a NNpH environment. As discussed in the previous section, the conditions required for SCC must develop prior to crack initiation, as shown in the far left of the figure. The growth curve is a superposition of two primary mechanisms of crack growth [6]. The first stage is modeled by the dissolution growth curve, which defines crack growth by direct dissolution of steel at localized areas during initiation or at the crack tip. The second stage is modeled by the hydrogen-facilitated fatigue growth curve, which defines crack growth by a process involving the interaction of fatigue and hydrogen embrittlement. Stage 2 crack growth is defined by the combined factor, $\Delta K^2 K_{max}/ f^{0.1}$ which will be discussed in **Section 2.6.5.5**. Finally, prior to failure the crack enters an instable growth phase, which is not of great significance in pipeline integrity as crack management programs should mitigate cracks prior to entering Stage 3. Instable crack growth will not be discussed further as the focus of this work is not on crack growth in that regime.
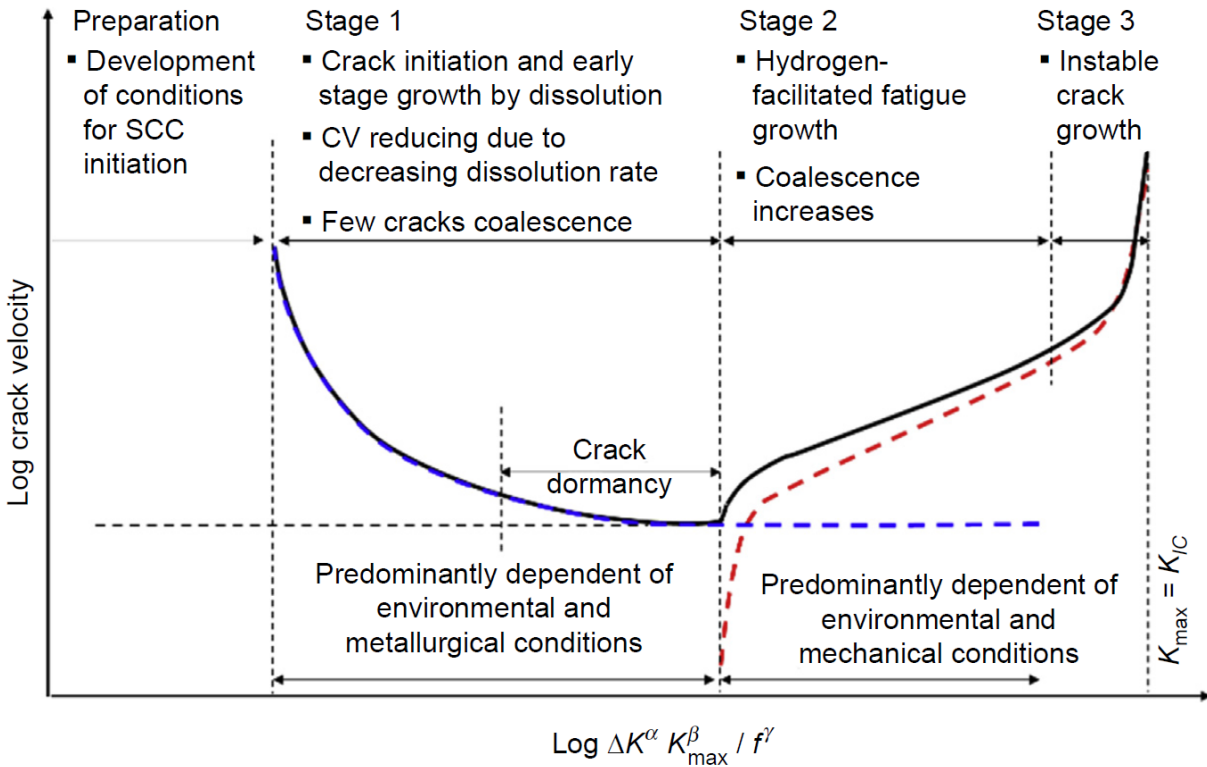
Figure 2.18   Schematic illustration of the effect of the combined factor upon SCC growth in pipeline steel exposed to NNpH solution [6].

2.6.3.1 Dissolution Crack Growth

Dissolution driven crack growth is primarily important in crack initiation and early-stage crack growth [6, 7, 53, 54]. Localized corrosion at the pipe surface causes crack initiation, leading to the formation of crack-like defects. This stage is usually dependent on coating conditions (**Section 2.5.1**), soil environments (**Section 2.6.1**) and steel metallurgy (discussed below). As time progresses and crack depth increases, the crack growth velocity decreases due to a reduction in the rate of dissolution at the crack tip. At this stage, the vast majority of cracks enter a state of dormancy, before they reach a depth 1 mm [98] (**Figure 2.19a**). Crack depths in Stage 1 crack growth can be controlled by effective coatings (**Section 2.5.1.1**) and cathodic protection (**Section 2.5.2**). Dissolution-driven crack growth is valid in Stage 1 due to the following [6]:

i.   Mechanical driving forces are negligible primarily due to a small stress intensity factor at the crack tip. The stresses required to induce fatigue crack initiation from metallurgical discontinuities requires aggressive loading conditions that are not seen in pipeline operation. For example, the loading conditions required to achieve initiation

44

by fatigue require low *R*-ratios (~ 0.4) and high maximum stresses (> 90 % SMYS) for over 10^5 cycles. However, the worst loading conditions experienced by pipelines are at discharge sites of oil pipelines where well below 1000 cycles per year meet the aggressive loading conditions described above [79, 82].

ii.   Crack initiation by hydrogen mechanism is not possible as the amount of diffusible hydrogen available in NNpH environments is very low. It has been shown that the amount of diffusible hydrogen available in pipeline steels is about ten times less than the level required to cause hydrogen induced blistering [99]. An exception to this may occur when excessively high levels of CP are applied. Excessive CP will cause an increase in the aqueous hydrogen concentration.

iii.   A common characteristic of NNpHSCC cracks is a generally wide crack crevice [2] due to the non-passivating nature of the corrosive environment which causes corrosion at the crack tip and on crack walls [77]. This type of corrosion causes pitting on the pipeline steel surface, reducing the mechanical driving forces present in the pipeline, which are required for crack growth mechanisms. It should be noted that this corrosion mechanism is quite different than the crack tip passivation and rupture mechanism of HpHSCC.
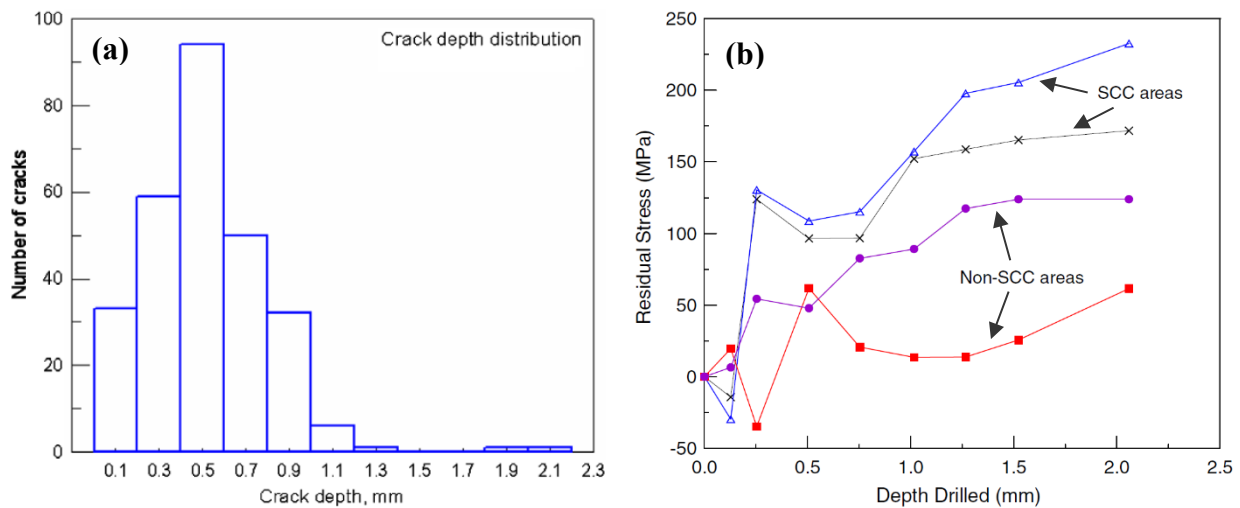
Figure 2.19   (a) Crack depth distribution in various crack colonies found on a ruptured pipeline segment after 19 years of service [98] and (b) the tensile residual stress distribution in the depth direction of a steel pipeline [46].

Beavers *et al.* [46] conducted a study to determine whether a correlation between pipe metallurgical factors and SCC exists. The study analyzed 24 SCC colonies and 28 control areas

from 14 pipes installed from the 1950's – 1970's. The following properties were measured in pipe area near the SCC colonies and in the control areas: surface roughness, residual stress, chemical composition, cyclic stress-strain behavior, grain size, microstructure, micro-hardness, inclusion size, shape and composition, and local galvanic behavior. It was concluded that there exists a strong correlation between (tensile) residual stress and the presence of NNpHSCC; **Figure 2.19b** shows that the residual stress found near the SCC colonies was approximately double the levels found in the control areas. Additional findings indicated that a higher micro-hardness and higher surface roughness both led to a higher susceptibility to SCC. Significant correlation between the remaining properties and SCC initiation was not found.

Residual stress is defined as a tensile or compressive force that exists in the bulk material without application of an external load [53]. Based on the length scale, residual stresses can be categorized in three types [100]. Type I is the macro-scale residual stresses, which vary over several grain diameters. Type I residual stresses in pipeline steels may be caused by the bending of steel plate material during pipe forming, differential cooling through the material thickness during rolling and localized plastic deformation during handling (i.e. bending, improper reinforcement during lifting, etc.). Type II is the micro-scale residual stresses, which vary over the grain scale. Type II residual stresses in pipeline steel are the typically related to microstructural and surface texture properties such as pearlite colonies versus ferritic grains. Type III is residual stresses at the atomic scale. These residual stresses are generated by chemical segregations at grain boundaries and differing phases in microalloyed steel.

Van Boven *et al.* [53, 54] initiated a two-part study to examine the role of residual stress in NNpHSCC of pipeline steels. Part 1 [53] explored the relationship between the Type I residual stresses described above and their effect on Stage 1 SCC growth behaviour on pipeline steels in a NNpH environment. Tensile and compact toughness (CT) specimens with varying levels of residual stress were tested in C2 solution and subjected to mean load pressure fluctuations. A residual stress profile was obtained using neutron diffraction. It was concluded that micro-pitting (~ 0.2 mm pit depth) occurred preferentially in areas of highest tensile residual stress (~ 300 MPa) and little corrosion or pitting occurred in areas with compressive stresses. All the cracks were found to have initiated from the bottom of the micro-pits. Cracking favourably initiated in areas of tensile residual stress in the range of 150 – 200 MPa. Cracks formed during the long-term tests

experienced crack tip blunting caused by dissolution of the crack walls and low temperature creep deformation. These crack tip blunting mechanisms occurred at depth locations where the cracking velocity had dropped below the anodic dissolution rate. This was attributed to a reduction in the local tensile residual stresses in the growth direction. This reduction in crack velocity correlates to the first portion of Stage 1 NNpHSCC growth.

Part 2 [54] was intended to both provide a quantitative analysis of the differences in the occurrence of pitting versus cracking and to establish a correlation between crack dormancy and the Type I residual stresses present in pipeline steels. The data used in this study was collected in Part 1, discussed above. It was found that cyclic loading can effectively attenuate the magnitude and gradient of residual stresses in a steel specimen. Additionally, it was concluded that the preferential pitting observed in Part 1 was a result of long-range galvanic stress cells. As cracks in NNpH environments can be easily blunted (via plastic deformation and crack tip dissolution), a high tensile residual stress gradient is necessary for development of cracks. As the crack grows in the depth direction, the tensile residual stresses may be lower than the near-surface residual stress causing the cracks to become dormant, which often occurs within less than 1 mm from the surface. This effect of crack dormancy is represented in the second half of Stage 1 NNpHSCC growth.

Tensile residual stress must be balanced by an equal compressive residual stress in the thickness of the material. It has been shown that high tensile residual near-surface stresses are usually accompanied by lower tensile residual stresses or compressive residual stresses in the depth direction [54]. According to **Figure 2.19a**, residual stress remains positive (tensile) within a depth of 2 mm from the pipeline steel OD surface. This suggests a compressive region of residual stress likely exists near the ID surface.

In conclusion, dissolution crack growth is the main initiation mechanism of NNpHSCC. It has been shown that cracks initiate from the bottoms of micro-pits that form in areas of maximum tensile residual stress, and favourably propagate in areas of mid-range residual stress. As the crack propagates away from the surface, lower tensile residual stresses and diffusion limited corrosion process are observed at the crack tip. Together, these effects slow the contribution of dissolution crack growth to the overall crack growth rate to a negligible level of 7.69×10^{-10} mm/s [44, 45].

2.6.3.2 Hydrogen-facilitated Fatigue Crack Growth

It has been determined that hydrogen plays a key role in NNpHSCC growth in pipeline steels [91]. An increase in hydrogen concentration in steel promotes crack propagation [101] and reduces fracture toughness [37]. It has been determined that IHAC is the primarily deliver mechanism for hydrogen in a NNpH environment [86]. Hydrogen-facilitated fatigue crack growth can be separated into two sub-categories:

i. **The role of fatigue**

In a laboratory testing environment, Stage 2 crack growth has not been observed under static loading conditions. In fact, active crack growth has been shown to become dormant when the loading is switched to a static hold [86] and crack growth re-initiates when cyclic loading is resumed. Furthermore, cyclic pressure fluctuations have been found to lower the threshold stresses for SCC initiation [97]. However, immediate crack growth did not resume in a NNpH environment when the mechanical driving force applied was low. This delayed re-initiation of SCC growth may be caused by initially lower levels of absorbed hydrogen ahead of the crack tip, dictated by the IHAC hydrogen transport mechanism (**Section 2.4.1.1**).

ii. **The role of hydrogen**

The presence of hydrogen is a critical for Stage 2 crack growth. Dormant cracks (Stage 1) do not experience high enough hydrostatic stresses to re-initiate. One of the extrinsic factors governing crack sharpening is the level of hydrogen present ahead of the crack tip in the plastic zone. This mechanism is partially responsible for the crack growth acceleration effect seen in Stage 2 cracking. As hydrogen diffuses to the plastic zone ahead of the crack tip, the threshold for micro-crack initiation is lowered by hydrogen-enhanced decohesion. It has been determined that hydrogen produced by corrosion at the crack tip is secondary in terms of crack growth, as compared with the amount of hydrogen generated on the pipeline surface resulting from general corrosion [96]. As the crack depth increases, the stress intensity ahead of the crack tip increases, increasing segregation of hydrogen to the area, further embrittling the localized area. The rate limiting step in this process is the diffusion of hydrogen from the surface to the plastic zone (IHAC). The critical role played

by diffusible hydrogen is demonstrated by testing CT specimens with varying levels of coating coverage, as shown in **Figure 2.20** [96]. The three specimens had the same crack geometry and loading conditions at $K_{max} = 35.3$ MPa√m, $\Delta K = 12.0$ MPa√m and $f = 0.005$ Hz ($\Delta K^2 K_{max} / f^{0.1} = 8635$ MPa^{3}m$^{3/2}$Hz$^{-0.1}$). Only the uncoated specimen with a bare surface exhibited a sudden increase in crack growth rate after a period attributed to the time required for hydrogen to reach a state of equilibrium throughout the specimen. This incubation time for the CT specimens immersed in C2 solution was found to be approximately 275 hours.
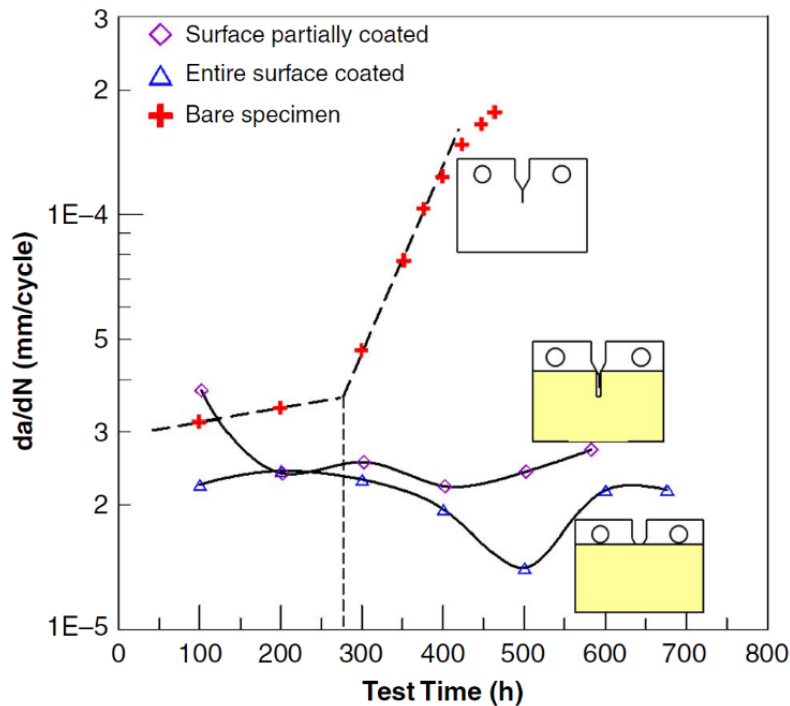
Figure 2.20   Crack growth rates of three CT specimens tested in C2 solution. All the tests were performed at the same starting conditions [86].

2.6.4 FRACTURE SURFACE CHARACTERISTICS

Totally brittle fracture in metals at the microscopic level occurs under certain specific conditions and is called cleavage fracture. More commonly in metals, the fracture surface contains varying amounts of transgranular cleavage and plastic deformation by slip. Grains oriented favourably with respect to the axis of loading may slip and exhibit ductile behaviour, whereas those oriented unfavourably cannot slip and will exhibit transgranular brittle behaviour [102]. When both fracture processes described above operate together, the fracture process is termed quasi-cleavage. The

typical crack morphology for NNpHSCC is characterized by a quasi-cleavage fracture surface [103], with microcracking ahead of the crack tip facilitated by hydrogen embrittlement and corrosion of the side walls and crack tip. Microscopic characteristics of quasi-cleavage include beach marks, river patterns and striations.

Beach marks can form when there is a change in the conditions at the crack tip such as a change in the loading conditions, or a variation in the corrosion rate of the crack tip. For example, when cracks are subjected to the loading cycle of a hydrostatic test, the region of crack growth immediately following the test will exhibit shear ridges or ductile tearing. The morphology of the crack face in this region of growth will appear distinctly different from the crack growth region generated before the hydrotest and after the crack has propagated past the damaged plastic zone.

River patterns are formed when a propagating cleavage crack encounters a grain boundary, where the nearest cleavage plane in the adjoining grain is oriented at a finite twist angle from the current cleavage plane. Initially, the crack accommodates the twist mismatch by forming micro-cracks on several parallel planes. As multiple cracks propagate, they merge by tearing between the planes [104]. The river pattern is indicative of the direction of crack propagation.

Microscopic features on the crack face such as striations are considered evidence of fatigue crack propagation. However, it is difficult to correlate striation spacing to the crack growth rate as each fatigue cycle does not generate a striation, but their average interspacing can provide insight to determine da/dN [95]. Constant amplitude loading cycles have been observed to generate distinct striations with approximately equal spacing (**Figure 2.21a**). When minor cycles are introduced, the large loading cycles still generate large striations, but mini striation are also formed (**Figure 2.21b**). This has been correlated to the contribution of minor cycles to crack propagation [88].
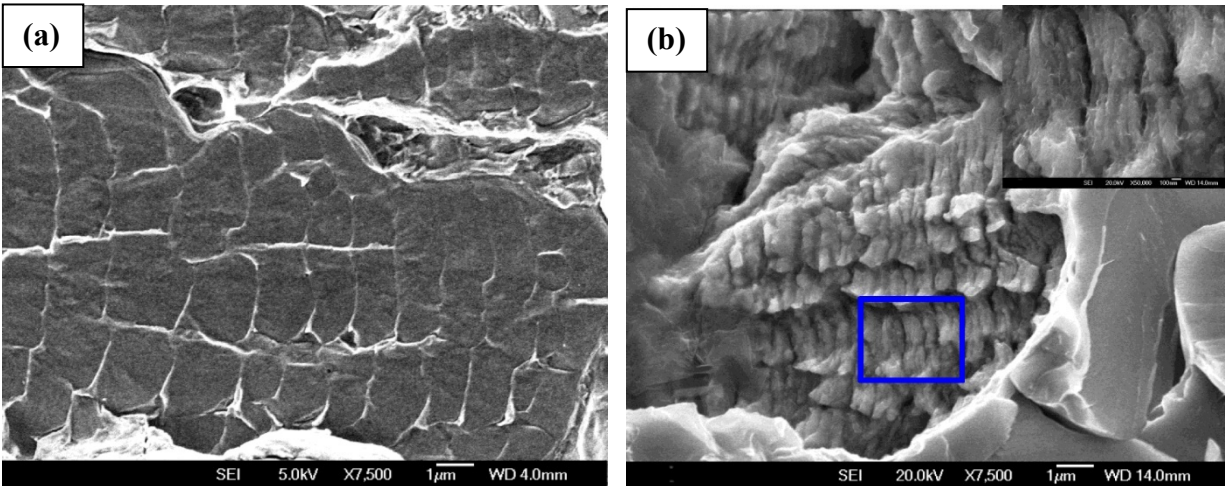
Figure 2.21   Fracture surface morphology of X-60 pipeline steel CT specimens after testing in C2 solution subjected to constant amplitude loading (a) and underload with minor cycle loading (b). Crack propagation is from left to right [42].

2.6.5 NNPH CORROSION FATIGUE MODELS

Clearly, the development of an accurate predictive model for pipeline crack growth in NNpH environments would be of great use to PLI and SCC management programs. However, frequently in experimental studies, crack growth can only be detected under aggressive loading conditions, which are not representative of field conditions [75]. Chen *et al.* [86] have suggested that since pipelines, especially gas transmission lines, are operated under near static condition most of the time, crack growth proceeds by repeated cycles of dormancy and active growth. The active growth cycle in this scenario would exhibit a substantially higher growth rate than that generally estimated for pipelines as these estimations usually do not account for periods of dormancy. According to statistical analysis of SCC data from the field, more than 95 % of SCC consists of dormant blunt-tipped cracks with depths of less than ~1 mm [4].

Appropriate modeling of corrosion fatigue requires the consideration of multiple parameters as discussed in the previous sections: the stress intensity factor range (ΔK), the maximum stress intensity factor (K_{max}), the loading frequency (f) and the effect of hydrogen. The following will introduce the most common corrosion fatigue models used for NNpH and examine their relevance to the current understanding of NNpHSCC growth mechanisms.

2.6.5.1 Paris Law

The Paris Law (**Section 2.3**), described by **Equation 2.4**, can be used to model fatigue crack growth. However, this model only considers the stress intensity range, ΔK. Additionally, this classical model was based on crack growth in an inert environment where the effects of environmentally assisted cracking were not present. As can be seen in **Figure 2.12** and **Figure 2.22**, crack growth in NNpH environments is also sensitive to the loading frequency and K_{max}, respectively, and their effects can not be ignored.

2.6.5.2 Unified Approach

The Unified Approach considerers both the amplitude (ΔK) and peak stress intensity (K_{max}) as key parameters contributing to fatigue crack growth and can be described by the following equation [105-108]:

$$da/_{dN} = C'\Delta K^m K^n_{max} \quad \textbf{Equation 2.8}$$

where C', m and n are material constants. In the Unified Approach, K_{max} is the principal driving force for fatigue crack propagation, while ΔK defines the extent of plastic damage at the crack tip. This model is slightly more relevant to NNpH crack propagation than the Paris Law, but it still does not consider the effect of the loading frequency.

2.6.5.3 Crack Tip Strain Rate Model

The crack tip strain rate model was proposed for cracks subjected to monotonic loading conditions where crack propagation is driven by the repeated film formation and rupture [109]. The crack tip strain rate for NNpH environments is given by [83]:

$$\dot{\varepsilon} \approx C_1 f (1-R) \quad \textbf{Equation 2.9}$$

where $\dot{\varepsilon}$ is the crack tip strain rate, C_1 is a constant, f is the loading frequency and R is the stress ratio ($R = K_{min}/K_{max}$). However, the NNpH corrosive environment is not conducive to the formation of a passive film, as discussed in **Section 2.6.1**, so this model is not commonly used for NNpHSCC.

2.6.5.4 Superposition Model

The superposition model has been designed with the intent to address the fatigue component of crack growth in a NNpH environment as it varies with pressure fluctuations seen in pipeline operation and is expressed as [32, 110]:

$$\left(\frac{da}{dN}\right)_{Total} = \left(\frac{da}{dN}\right)_{Fatigue} + \frac{1}{f}\left(\frac{da}{dt}\right)_{SCC} \quad \textbf{Equation 2.10}$$

where $(da/dN)_{Total}$ is the total crack growth per cycle in a NNpH environment, $(da/dN)_{Fatigue}$ is the crack growth per cycle contribution caused by inert fatigue, f is the frequency of the fatigue cycle and $(da/dt)_{SCC}$ is the crack growth contribution of SCC in terms of time in a NNpH environment.

However, crack propagation in a laboratory NNpH environment has never been observed under a static load. Furthermore, active cracks have been found to enter dormancy under static loading conditions [53, 68, 86, 87, 111]. **Figure 2.22** shows the results of a study by Chen *et al.* [86] that found crack growth arrest under static hold at two K_{max} values. When cyclic loading was resumed, crack growth followed (although it did not occur immediately if the mechanical driving force was low).
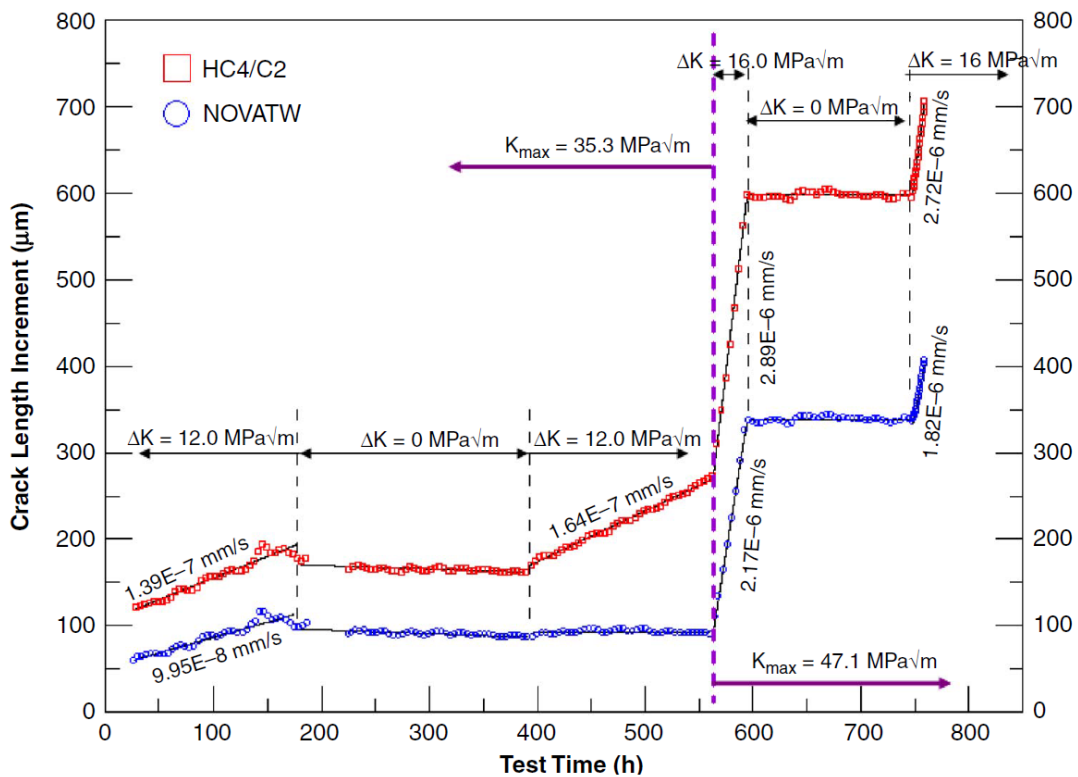
Figure 2.22   CT specimen crack growth rates in two laboratory simulated NNpH environments [86].

2.6.5.5 Combined Factor Model

The combined factor equation governing the Stage 2 crack growth rate in CT specimens in a NNpH environment (C2 solution) subjected to constant amplitude loading, is consistent with true corrosion fatigue and is shown below [85, 86]:

$$\frac{da}{dN} = A\left(\frac{\Delta K^\alpha K_{max}^\beta}{f^\gamma}\right)^n + h \quad \textbf{Equation 2.11}$$

where A, n (=2), α (=0.67), β (=0.33) and γ (=0.033) are all constants for a given material; and f is the loading frequency. The first term, referred to as the combined factor, and the second term (h) are the contribution towards the overall growth rate of corrosion fatigue and the contribution of crack growth by direct dissolution at the crack tip, respectively. The value of h can be determined experimentally and was found to contribute to crack growth about 10 times less than corrosion fatigue [44, 45]. In fact, the corrosion rate of direct dissolution in the Stage 2 NNpH crack growth has been found to be lower than the corrosion rate of bare coupons exposed to NNpH environments [42].

Although **Equation 2.11** agrees with laboratory data for CT specimen crack growth under constant amplitude loading conditions, it does not translate to surface crack growth such as crack growth observed in pipelines operating under variable amplitude pressure fluctuations. Therefore, understanding the load interactions of variable amplitude pressure fluctuations on crack growth in NNpH environments is critical.

The combined factor makes it possible to model crack growth with all the contributing factors included, such as crack dimension, pressure fluctuations, materials and environments. In a NNpH laboratory environment, the threshold value of $\Delta K^2 K_{max}/f^{0.1}$ demarcating the boundary between active crack growth and crack dormancy in a CT specimen was determined to be in the range of ~ 8500 MPa^{3}m$^{3/2}$Hz$^{-0.1}$ [85], as shown in **Figure 2.23**. Additionally, the crack growth rates shown have been subjected to a variety of cyclic frequencies varying from 0.1 to 0.00125 Hz. The application of the combined factor equation to Type I fluctuations requires an acceleration factor to account for the increased crack growth rate compared to Type II fluctuations due to load interactions between the underload and minor cycles. Similarly, Type III fluctuations require a retardation factor to account for the decreased crack growth.
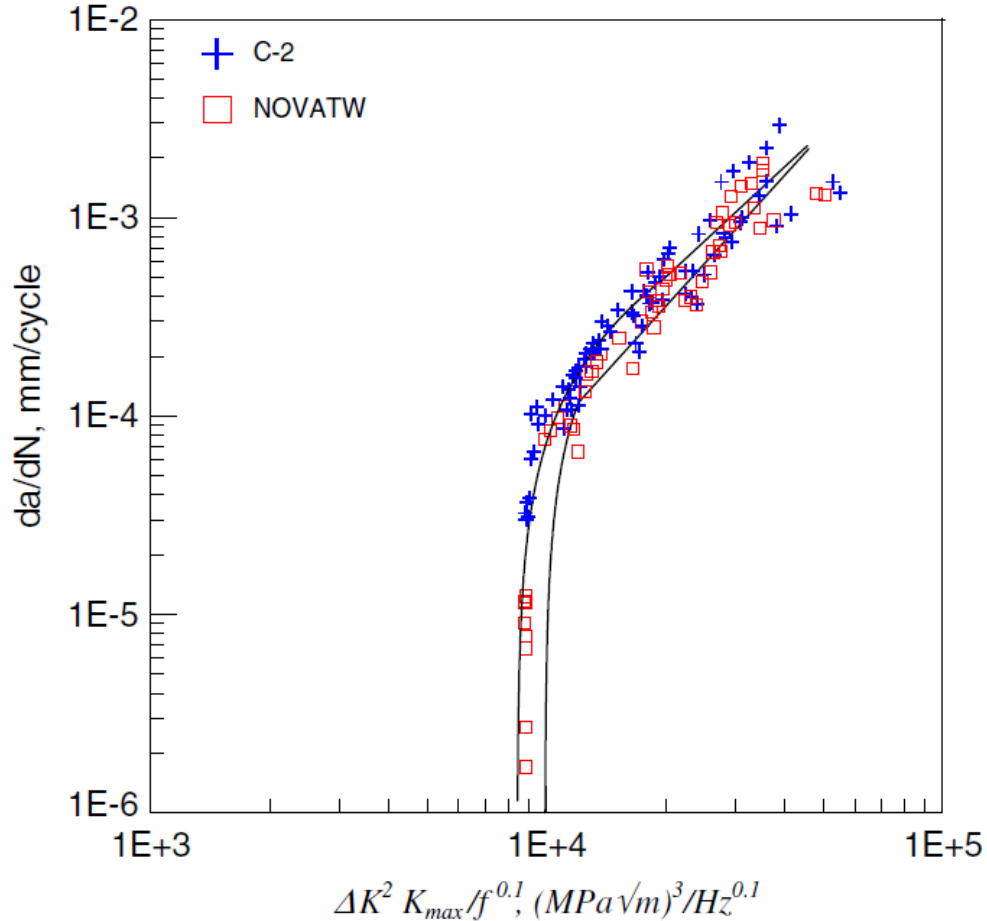
Figure 2.23 Comparison of CT specimen crack growth rate da/dN as a function of the combined factor $\Delta K^2 K_{max}/f^{0.1}$, showing the threshold for crack growth in two different NNpH solutions [85].

It should be noted that there is a breakdown of the frequency term of the combined factor equation (**Equation 2.11**), which predicts that the crack growth is inversely proportional to the loading frequency. However, this has been found experimentally to only be true for frequencies higher than 10^{-3} Hz, as evident in **Figure 2.15**, where the crack growth rates in CT specimens was found to decrease with decreasing f when $f < 10^{-3}$ Hz [77]. This can be explained by relating the two competing mechanisms for crack growth. At frequencies above 10^{-3} Hz, the primary driving force is the hydrogen effects. This mechanism is limited by the diffusion time available for hydrogen between peak stresses of the loading cycle where the maximum embrittlement effect is at 10^{-3} Hz. Once the frequency drops below 10^{-3} Hz, blunting effects due to the corrosive environment begin to lower the stress intensity ahead of the crack tip. This lowers the overall crack growth rate as the crack growth now exhibits blunting and re-initiation type growth.

2.7 RESEARCH OBJECTIVES

Extensive experimental studies have been conducted to investigate near-neutral pH stress corrosion cracking (NNpHSCC) initiation and growth mechanisms. However, conditions in the field are not conducive to controlled loading conditions studied during laboratory simulations. Furthermore, the loading conditions required to achieve NNpHSCC growth in laboratory simulations are more aggressive than the loading conditions in the field that have been found to produce NNpHSCC. The theoretical growth curve of NNpHSCC has been proposed by superimposing two competing mechanisms of crack growth. In Stage 1, crack initiation and initial crack growth are controlled by a dissolution mechanism. In Stage 2, crack growth is governed by a hydrogen-facilitated fatigue mechanism that has been modeled by the combined factor equation.

The objective of this thesis study is to investigate Stage 2 crack re-initiation and growth in a NNpH environment using a full-scale specimen to validate the combined factor model. The entirety of this work will be based a single long-term test conducted on a pipe segment containing dormant cracks initiated in the field under NNpH environmental conditions. The primary objective of this study is to determine the effect of loading conditions on Stage 2 NNpHSCC re-initiation and growth:

i. threshold stress intensity factor for crack re-initiation in a NNpH environment;
ii. crack growth rates under Type I and Type II pressure fluctuations;
iii. the contribution of minor cycles towards crack growth in a full-scale specimen;
iv. and validation of experimental results studying crack growth in SCT and CT specimens.

Additionally, an opportunistic study of Stage 1 crack initiation on dents machined in the full-scale specimen and exposed to the NNpH environment will be conducted.

CHAPTER 3: EXPERIMENTAL METHODS

The following chapter will provide the experimental methods used to obtain the results presented in **Chapter 4**. First, the properties and pre-test preparation of the full-scale specimen will be introduced. Then, the corrosion cell and simulated NNpH environment will be discussed. Next, the mechanical loading conditions and the pressure control system designed to achieve those conditions will be presented. Finally, the end of test procedure and crack characterization will be given in detail.

3.1 MATERIAL AND SPECIMEN

The following sections will introduce the history and material properties of the pipe segment used for the full-scale test. Then, the pre-test preparation including inspection methods, machining of dents, end cap installation and external pipe surface preparation will be discussed.

3.1.1 MATERIAL

The sample used for this study was taken from a pipe cut out during an integrity assessment in February 2015, where excavation of the segment began on February 10th of that year. The spiral double submerged arc welded pipe was part of TC Energy's pipeline network in Alberta. The line contained natural gas and was protected with a single wrap polyethylene tape coating and an impressed current cathodic protection (CP) system. Over 46 years of service (1969-2015) detrimental SCC colonies formed, which were responsible for the removal of the pipe from service. The material specifications of the pipe provided by TC Energy are shown in **Table 3.1**.

The material composition of the X-60 pipeline steel used for this study is shown in **Table 3.2**. The composition was obtained using a laser induced breakdown spectroscopy unit provided by Acuren. The tensile strength of the steel was tested in accordance with ASTM Standard E8 using a 5.55 mm thick rectangular sheet-type sample and a crosshead speed of 0.015 mm/mm/min (Control Method C). The yield strength (at 0.2 % offset strain) and ultimate tensile strength were determined to be 456 MPa and 580 MPa, respectively, using the stress-strain curve shown in **Figure 3.1**. The impact strength of the steel was tested in accordance with ASTM Standard E23 using two different orientations of sub-size specimens. The two specimen sets were machined to test the impact

strength in the longitudinal and hoop directions of the pipe. The average impact strength of the specimen orientation at −19 °C was 35.8 J/m (*n=8*) and 31.8 J/m (*n=8*), respectively.

Table 3.1   Material Specification of the X-60 pipeline steel used in the full-scale test.

OD (mm)	W.T. (mm)	% SMYS	Grade (MPa)	MOP (kPa)	Manufacturer	Year of Construction
457.2	6.35	79.93	414	9193	Ipsco	1969

Table 3.2   Composition of the X-60 pipeline steel determined using laser induced breakdown spectroscopy.

Element	Composition (wt %)
C	0.11
Mn	1.17
Ni	0.53
Cr	0.42
Cu	0.28
Si	0.10
V	0.074
Mo	0.046
Nb	0.023
Pb	0.006
Al	0.001
Ti	0.0002
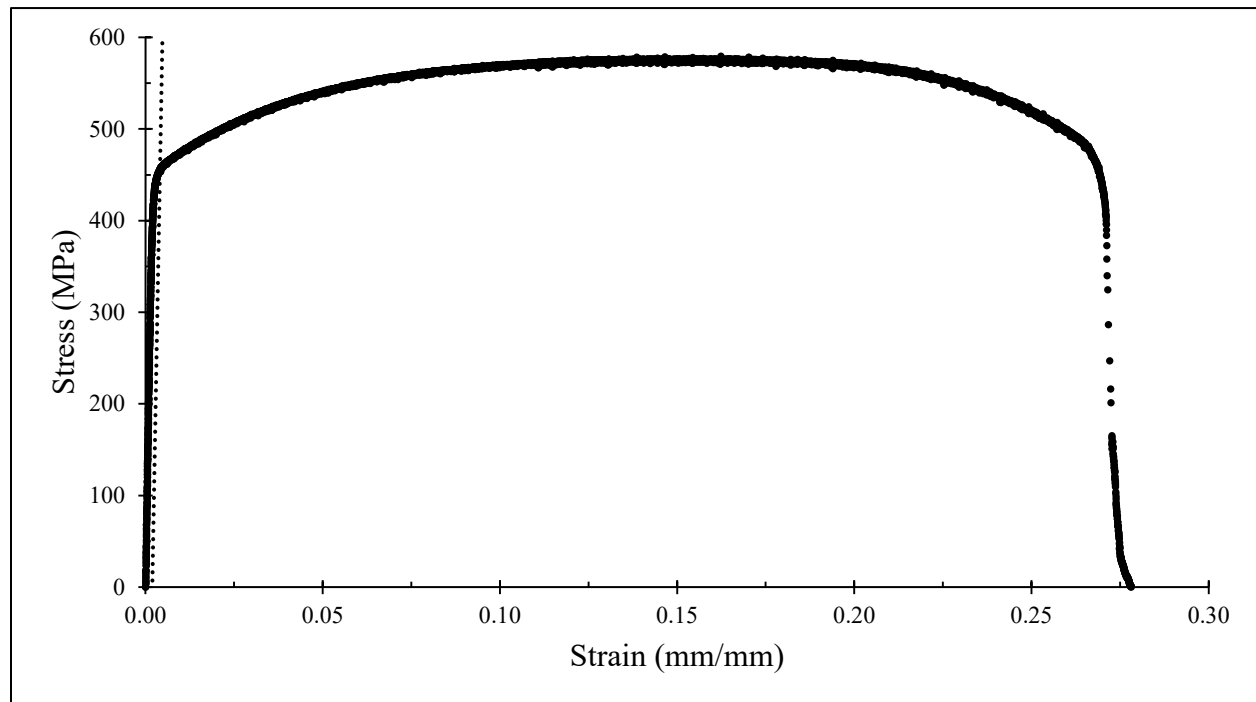
Figure 3.1   The stress-strain curve of the X-60 pipeline steel used for the full-scale test.

3.1.2 FULL-SCALE SPECIMEN

The full-scale specimen was stored outdoors in the Arnett & Burgess (A&B) Pipeliners Ltd. laydown yard in Blackfalds, AB from the time it was removed from service in February 2015 until it was cut and shipped to Edmonton, AB in October 2017. The pipe was wrapped in thin clear plastic to protect it from the elements; however, the wrap was damaged over time and the pipe surface was exposed to rain and snow. The surface condition of the pipe after sitting in the laydown yard is shown in **Figure 3.2**. Prior to shipping the specimen to Edmonton, a 4.77 m segment of the pipe was plasma cut by a A&B welder. The 4.77 m pipe segment was shipped to the I.F Morrison Structures Laboratory at the University of Alberta for temporary storage. The following sections chronologically describe the work done to prepare the pipe segment for the full-scale test.

Figure 3.2   Image of the pipe that was designated for testing, taken before it was cut down to the full-scale specimen length showing the external surface condition.

3.1.2.1 Pre-Test Inspection

The pipe segment was transported from the I.F Morrison Structures Laboratory to the Petro-Line (PL) shop located in Nisku, AB. Upon arrival to the PL shop, the pipe was sandblasted with Enviro-Grit (EG) Glass Abrasive 12-50 [112] to remove the general corrosion that had developed on the pipes outer surface during the time it sat in the A&B laydown yard. Sandblasting is required to prepare the steel surface for non-destructive examination. After sandblasting, the pipe was housed indoors to prevent any further corrosion.

Black on white MPI was performed by a CGSB MT 2 certified technician from IRISNDT to identify the external SCC colonies on the pipe segment. SCC colonies were identified and numbered by the technician. An image of the pipe with these mark-ups is shown in **Figure 3.3**. Finally, a technology using eddy current was used to collect pre-test crack length and depth measurements of the SCC colonies identified by MPI.

Figure 3.3 4.77 m pipe segment after pre-test MPI, with SCC colony borders drawn in red.

3.1.2.2 Dents

Four dents were created in the pipe segment at the twelve O'Clock position to simulate line strike damage from a blunt object. The dents were introduced in areas of the pipe such that they did not interact with any pre-existing cracks or welds. Dents A, B, C and D were generated by a technician at PL by striking selected areas repetitively with a sledgehammer until the dents reached depths of 8, 9, 8 and 8 mm, respectively. This corresponded to a dent depth of 1.7 to 2.0 % of the pipe's nominal outer diameter, which was well within the acceptable limits for a dent to remain in service if it was located in the pipe body and does not interact with a stress concentrator [8]. A simulated disbonded coating was installed on Dent B to study crack initiation on a dent that was shielded from CP.

3.1.2.3 Pipe End Caps

In order to develop internal pressure, end caps were required to be installed at each end of the pipe segment. Standard X-70 end caps were sourced from MRC Global by PL for this purpose. Overmatched material was chosen to mitigate the likelihood of test failure due to complications with the end caps. Prior to welding, the ends of the pipe segment were ground to remove any material that may have been damaged during the plasma-cutting process. An Alberta certified Grade B pressure welder employed by PL welded the end caps to the pipe segment using shielded metal arc welding (SMAW). The electrode used for the root pass was AWS E8010-P1, and the

60

electrode used for the fill and cap of the weld was electrode E8018-C3. The number of fill passes was not provided.

Prior to attaching the end caps to the pipe segment, three half inch diameter holes were machined into one of the end caps such that one hole was placed in the centre of the end cap, and the other two were placed in the twelve and six O'Clock positions. A half inch female NPT thread-o-let was welded over each of the holes by an Alberta certified Grade B pressure welder. Welding procedures were not provided for these welds. The thread-o-lets were used to connect to the inlet, outlet and emergency relief lines of the pressure control system, which will be discussed further in **Section 3.3**.

3.1.2.4 Pipe Surface Preparation

Surface preparation of the sections of the pipe selected for exposure to the NNpH corrosive environment was required. Laboratory grade acetone was used to remove the paint and other surface contaminants left behind from the MPI procedure. Next, the surface was scrubbed with an ethanol-soaked cloth for a final cleaning. Final surface condition is shown in **Figure 3.4**. This procedure served two purposes. First, removal of the surface contaminants ensured integrity of the chemistry of the corrosive environment. Second, a clean metal surface was required to facilitate a reliable water-tight seal between the corrosion cells and the pipe surface.

Figure 3.4 (Top) final metal surface preparation of selected areas of the pipe segment and (bottom) pipe segment during live testing.

3.2 Corrosion Cell and Environemnt

Three areas of the exterior surface of the pipe segment that had dense SCC colonies were selected to be encapsulated in a simulated NNpH environment. This section will describe the corrosion cells, the test solution, the internal pipe fluid, and finally the cathodic protection (CP) system used for the full-scale test.

3.2.1 Corrosion Cell

Three identical corrosion cells, referred to as boxes, were built for the full-scale test by CME machinist technicians at the University of Alberta. The far box, middle box and close box as shown in **Figure 3.4** were named Box A, Box B and Box C, respectively. The boxes were placed at least three pipe diameters away from the end caps in order to achieve uniform pressure in the pipe areas subjected to the external corrosive environment.

A side-by-side comparison of the schematic and real image of Box B is shown in **Figure 3.5**. Each box was fabricated with 2.54 cm thick grey PVC sheet material and glued together with PVC glue, apart from a single viewport consisting of 1.27 cm thick transparent acrylic. The viewport served to position the tip of the salt bridge near the pipe surface.

The internal box dimensions were 55.88 cm tall by 55.88 cm wide by 50.80 cm deep. The boxes consisted of two pieces: a top half and a bottom half. The top half of the box had three auxiliary boxes exposed to the atmosphere attached to it, as well as a gas inlet port, gas outlet port and a salt bridge port. All three auxiliary boxes were connected to the internal box by a 2.54 cm diameter hole near the bottom of each auxiliary box. The level of the NNpH solution surpassed the holes, protecting the internal box from the oxygenated auxiliary boxes. The two larger auxiliary boxes served as anodic chambers for the CP system and will be discussed further in **Section 3.2.2.3**. The third smaller auxiliary box was designed with a removable cap and was used to periodically check on the solution level throughout the test. The bottom half of the box contained a drain port used to take fluid samples for *pH* measurement, and to drain the box of fluid. Diagonal inserts were installed on both sides of the bottom half of the box in order to reduce the internal volume of the corrosion cells. The two halves were connected using two corner butt joints on each side, as shown in **Figure 3.5**.

Each box contained the bulk test solution and was sealed to provide the anaerobic atmosphere required for the corrosive environment. A perfect water-tight seal was achieved by running a 0.95 mm diameter EDPM o-ring along the gaps between the pipe and the box as well as between the two box halves. Then silicone was applied to both sides of the o-ring. Each box weighed approximately 45 kg and contained 55 kg of liquid. This weight was supported by a 2.5-Ton scissor jack in order to protect the o-ring from excessive compression at the twelve O'Clock position, maintaining the integrity of the water-tight seal.
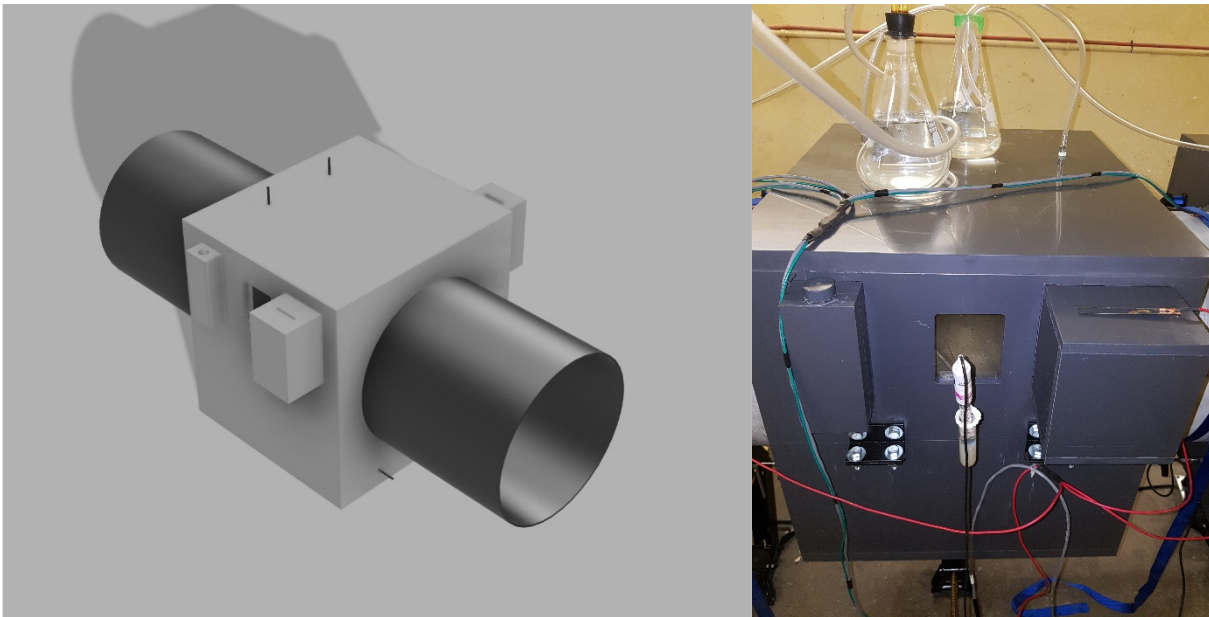
Figure 3.5   (Left) computer rendered drawing of the corrosion cell and (right) the actual corrosion cell in use.

3.2.2 CORROSIVE ENVIRONMENT

This section describes the NNpH solution used inside the corrosion cells, the fluid used to fill the pipe to develop pressure during the test and the CP system.

3.2.2.1 Test Solution

A dilute groundwater solution known as C2 solution was used to simulate the NNpH environment during the full-scale test. The composition of the C2 solution is shown in **Table 3.3**. The solution was prepared with distilled water and lab grade reagents in 60 L batches, using three 20 L white plastic pails with lids that provided an air-tight seal. The inlet and outlet gas lines of the pails were daisy chained such that only one compressed gas cylinder was required to purge all three pails simultaneously. Each 60 L batch filled one of the corrosion cells. Inlet and outlet gas lines were

installed in the lid of each pail with Swagelok bulkhead fittings. During preparation, the pails were placed on magnetic mixing pads and purged with 5 % CO_2 + 95 % N_2 gas mixture for at least 72 hours until a measured *pH* of ~ 6.29 was achieved. The procedure used to perform *pH* measurements can be found in **Section 3.6.5**.

The C2 solution was transferred to the boxes prior to commencing the full-scale test. The first row in **Table 3.4** shows the dates each box was initially filled. During this time, CP was applied and a 5 % CO_2 + 95 % N_2 gas mixture was purged through the corrosion cells. The inlet line of the gas mixture was extended to the bottom of each corrosion cell to ensure complete mixing of the aqueous CO_2. Purging with CO_2 was necessary to ensure an anaerobic environment inside the corrosion cell, as well as to maintain the *pH* of the C2 solution.

Throughout the duration of the full-scale test (July 23, 2018 to October 22, 2018), the *pH* of the C2 solution was measured by taking a sample directly from the boxes. The samples were collected using the drain port near the bottom of each box. The solution was changed when the *pH* increased above 6.40. This occurred once throughout the duration of the full-scale test and the second row in **Table 3.4** shows the dates the C2 solution was replaced in each box.

Table 3.3   Composition of the simulated NNpH solution, C2, used for the full-scale test [113].

Species	Concentration (g/L)
$MgSO_4 \cdot 7H_2O$	0.0274
$CaCl_2$	0.0255
KCl	0.0035
$NaHCO_3$	0.0195
$CaCO_3$	0.0606

Table 3.4   C2 solution changelog: Each date (yyyy-mm-dd) shows when fresh C2 solution was added to the boxes.

Box A	Box B	Box C
2018-07-13	2018-07-16	2018-07-19
2018-08-22	2018-08-28	2018-08-31

3.2.2.2 Internal Fluid

The internal fluid used to develop pressure was City of Edmonton water inhibited with 1.0 % CORTRON R-2383 provided by Nalco Champion. Inhibited fluid was chosen in order to eliminate the risk of failure due to internal corrosion. Liquid media was selected over gas media as the safety risk of a liquid media was determined to be lower than that of a gas media.

3.2.2.3 Cathodic Protection System

Criteria for adequate CP of a metallic piping system is defined in NACE SP0169 as either a minimum of 100 mV of cathodic polarization, or a structure-to-electrolyte potential of -850 mV (or more negative) as measured with respect to a copper – copper (II) sulphate electrode (CSE). A value of -130 mV of cathodic polarization was chosen to be applied to the full-scale test by an impressed current system using a Model 363 Potentiostat-Galvanostat manufactured by Princeton Applied Research. A custom cable connecting the Potentiostat to the full-scale test was built by a University of Alberta CME electronics technician. The cable connected the boxes to the CP system in a parallel circuit. An image of the wiring for the CP system is shown in **Figure 3.7**. CP was applied to the pipe to provide a surplus of aqueous hydrogen in the corrosion cells.

The anodic chamber was connected to the corrosion cell by a 2.54 cm diameter hole near the bottom of the anodic chamber. The hole was situated below the water line in the anodic chamber in order to maintain an anaerobic environment in the bulk solution, while allowing diffusion of electrons from the anode to the cathode. Each box had two anodic chambers constructed on opposing sides. The sacrificial anode used was 304 stainless steel sheet metal manufactured by Maudlin Products and was replaced once during the test. CP readings were taken incrementally over the course of the test and are shown in **Figure 3.6**.
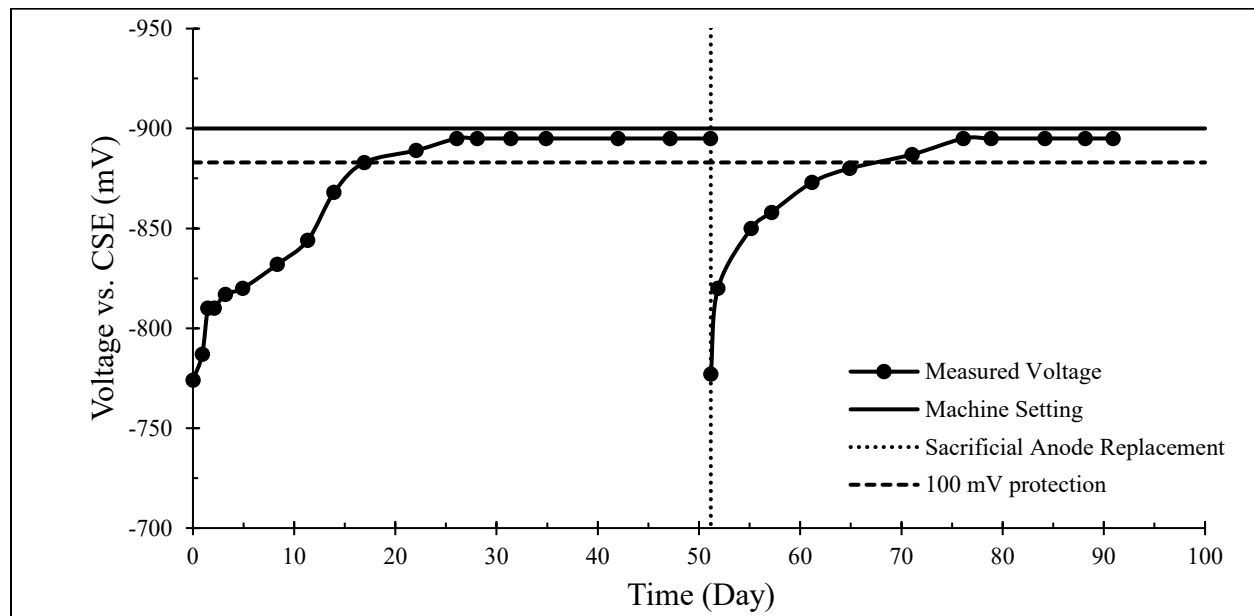
Figure 3.6   Structure-to-electrolyte potential readings with respect to a CSE reference, measured using a digital multimeter.

Cathodic
connection

Anode

Ag/AgCl
reference
electrode

Salt
bridge
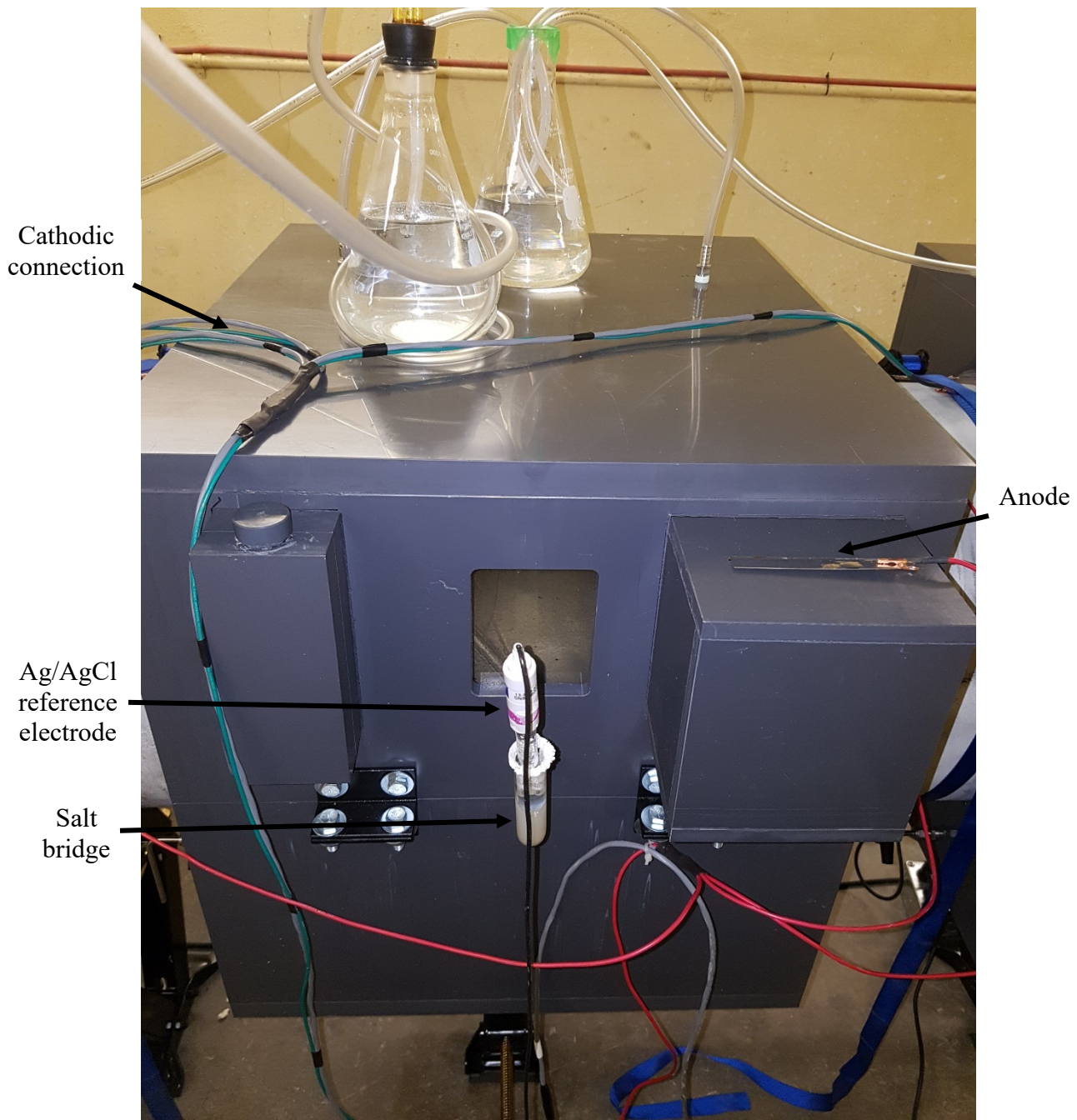
Figure 3.7   Image of Box B with annotations describing the CP system.

3.3 Pressure Control System

Pressure was developed and released using a program designed by a University of Alberta CME electronics technician for the full-scale test and will be referred to as the pressure control system (PCS) throughout this section. The PCS was responsible for sending electronic control signals to the plumbing system and receiving pressure data from the pressure transmitter. The plumbing system was assembled by University of Alberta CME machinist technicians. It was connected to the pipe with three half inch female NPT thread-o-lets welded onto one of the end caps, as shown in **Figure 3.8**. This section will describe the plumbing system used to develop and release pressure during the test, the safety measures put in place for safe operation throughout the test, and finally the hardware and software used to automate and record the pressure fluctuations. Unless otherwise specified, all valves and fittings used in the plumbing system were 316/316L stainless steel NPT connections manufactured by Swagelok.

Figure 3.8 Photograph of the plumbing system built for the full-scale test.

3.3.1 DEVELOPING PRESSURE

Internal pressure was developed using a pneumatic driven liquid Haskell pump. The thread-o-let connection at the six O'Clock position on the end cap was connected to a 1.5 hp single-drive head ASF-35 Haskell pump supplied by Wainbee Limited. A two-way stainless-steel ball valve was installed between the end cap connection and the pump outlet to enable isolation of the pump from the pressurized pipe segment in case emergency pump maintenance was required. The pump was driven with 90 psi compressed air. The air flow was metered using an air-to-open research control valve (Type P78S, S/N 87605). The control valve used was a normally closed valve so in the event of power loss, the Haskell pump would stop throttling. The control valve opening was manipulated using a Moore I/P Transducer Model 77-16, which received signal from the PCS. The pump inlet was supplied with inhibited water from a 208 L unpressurized barrel reservoir and was filtered with a 25-micrometer polypropylene filter to protect the pump from particulate. The tubing used for this section of the plumbing system was 12.7 mm OD, 0.89 mm wall thickness 316/316L stainless steel seamless tubing.

3.3.2 RELIEVING PRESSURE

Pressure was relieved using a needle valve and a solenoid valve. This portion of the plumbing was connected to the pipe at the mid-point of the end cap to minimize the amount of particulate that reached the solenoid valve. The normally closed EH40-08-A120 solenoid valve was manufactured by Clarke Cooper and was supplied by Strata Controls. The solenoid valve received signal from the PCS and vented fluid into the same 208 L barrel reservoir the as pump intake. The needle valve ($Cv = 0.44$) was manufactured by Cole-Parmer and was placed upstream of the solenoid valve in the relief line of the plumbing system. The needle valve was used to reduce the flow rate of high-pressure fluid reaching the solenoid valve, which enabled greater control during the pressure relief process.

Pressure measurements were taken from this line by a pressure transmitter (PT) and were relayed to the PCS for recording. The PT was manufactured by Cole-Parmer (Item # RK-07356-64) and was placed upstream of the needle valve in the pressure relief line. Pressure data was measured by the PT every 0.1 s, and the average of every ten pressure measurements was recorded by the PCS each second. The accuracy of the PT was ± 0.4 % using the best fit straight-line calculation method.

The tubing used for this section of the plumbing system was 12.7 mm OD, 0.89 mm wall thickness 316/316L stainless steel seamless tubing.

3.3.3 EMERGENCY PRESSURE RELIEF

An emergency pressure relief redundancy was built into the plumbing system of the full-scale test to protect the pipe segment from unexpected high pressure. A relief valve capable of a higher flow rate than the maximum pump output was selected to protect the pipe segment against uncontrolled throttling of the pump. The thread-o-let connection at the twelve O'Clock position on the end cap was dedicated to this redundancy. The relief valve used was a V66 Series spring-loaded pressure relief valve supplied by DK-Lok Canada. The RVS-D spring was used, which supported a cracking pressure range of 1,500 to 2,250 psig. The relief valve was calibrated to crack at a pressure of 1,500 psi (90 % SMYS). This pressure was selected as it was above the maximum operating pressure of the full-scale test (1250 psi). Additionally, the selected pressure fell below the yield strength of the pipe, which offered protection against unintended plastic deformation at the crack tips in the event of unexpected high pressure. The relief valve outlet tubing vented into the same 208 L barrel reservoir as the rest of the plumbing. For further safety considerations such as the hierarchy of hazard control implemented, refer to **Appendix B**. The tubing used for this section of the plumbing system was 6.35 mm OD, 0.89 mm wall thickness 316/316L stainless steel seamless tubing.

3.3.4 COMPUTER LOGIC PROGRAM

The pressure control system consisted of a hardware and software component. The hardware was a CompactRIO manufactured by National Instruments and the software was written using National Instruments LabVIEW developing environment. The CompactRIO was provided by the University of Alberta department of CME for the duration full-scale test and the LabVIEW program was written by a University of Alberta CME electronics technician. The full pressure scheme was programmed into the CompactRIO, and electrical signals were sent to the control valve and solenoid valve to manipulate the pressure according to the pressure scheme. The CompactRIO had the ability to process the live pressure data measured by the PT and could apply a differential adjustment to the loading rate if the internal pressure deviated from the programmed value.

3.3.5 UNINTERRUPTIBLE POWER SUPPLY

An uninterruptible power supply (UPS) was required to protect the critical systems controlling the full-scale test from failing in the event of an unexpected power outage. The UPS used was a BR1500G 865 W lead-acid battery unit manufactured by American Power Conservation. In the event of a power outage, the UPS could provide approximately four hours of power to the CompactRIO module, the Potentiostat, the I/P Transducer and the solenoid valve. An emergency notification system was deployed to alert the author of the power outage immediately so that an appropriate course of action could be taken to prevent the critical systems from de-energizing.

3.4 MECHANICAL LOADING CONDITIONS

An abundance of SCC colonies were present in the pipe segment from field service, as previously discussed. Variables $2c$ and a refer to the crack's total surface length and depth length, respectively. Pre-test inspection of the pipe segment (using ECHO-3D technology) indicated that many of the crack depths (a) fell in the range of 0.5 mm < a < 1.2 mm, with occasional deep cracks up to a maximum depth of 2.1 mm.

The full-scale test pressure scheme was designed with four distinct regions. The values for the pressure scheme are shown in **Table 3.5**, and the pressure scheme is visualized in **Figure 3.9**. In order to design a pressure scheme that would generate appropriate crack growth for cracks with initial depths below 1.0 mm without causing critical failure at the worst flaw (2.1 mm depth), a crack growth prediction calculation was conducted using arbitrary crack geometry that fell within the pre-test crack inspection results. A constant maximum stress of 75 % SMYS was applied to all four variable amplitude pressure scheme regions. The maximum stress intensity (K_{max}) values were calculated using the Newman and Raju stress intensity equation for a semielliptical surface flaw in a flat plate for $a \leq c$ [114]. The ΔK values were determined using the stress ratio (R) value of each underload cycle (Regions II & IV), or the R value of the constant amplitude cycle (Regions I & III). A crack growth acceleration factor of 1.2 was used to account for the presence of minor cycles (MC), as the combined factor (CF) equation does not account for this. The results of this calculation are shown in **Table 3.6**.

Two types of cyclic waveforms were used in mechanical testing: Constant Amplitude (CA) and Underload with Minor Cycles (UL&MC). In the following sections, the regions with a CA loading scheme and the regions with a UL&MC loading scheme will be discussed. The actual pressure fluctuation data collected during the full-scale test will be presented in **Chapter 4**.

Table 3.5   Parameters used for the full-scale test pressure fluctuations.

Region	Days	Blocks	R UL	R MC	f (Hz)	Loading Rate (psi/s)
I	5	432	0.50	-	0.001	1.25
II	18	270	0.60	0.90	0.001	1.00
III	3	259	0.60	-	0.001	1.00
IV	65	535	0.80	0.90	0.001	0.50

Table 3.6   Predicted crack growth calculation conducted using arbitrary crack geometry that fell within the crack dimensions reported during the pre-test inspection.

Applied max stress % SMYS	psi	2c mm	a mm	Region I	Region II	Region III	Region IV	Total Growth	Final Depth
					μm			μm	% NWT
75	1250	250	2.1	387	350	476	678	1891	63
75	1250	100	2.1	323	241	257	240	1061	50
75	1250	50	2.1	261	170	159	128	718	44
75	1250	50	1.5	130	77	67	51	326	29
75	1250	20	1.5	106	59	50	37	251	28
75	1250	50	1.0	63	35	29	22	149	18
75	1250	20	1.0	57	31	26	19	133	18
75	1250	50	0.75	40	21	18	13	92	13
75	1250	20	0.75	37	20	17	12	86	13
75	1250	10	0.75	34	18	15	11	77	13
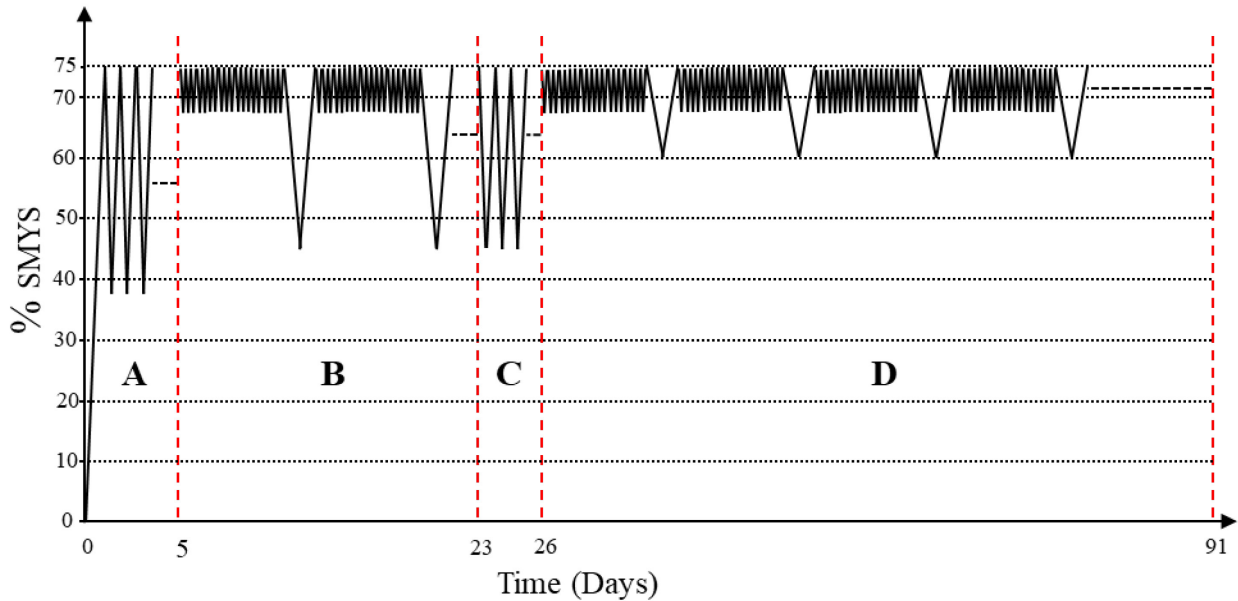
Figure 3.9   Visualization of the variable amplitude pressure scheme used during testing. Sections A, B, C and D correspond to Regions I, II, III and IV respectively.

3.4.1 REGION I & III WAVEFORMS

Region I & III waveforms were designed with CA loading conditions. The goal of these pressure schemes was to quantify the growth rate (da/dt) associated with CA loading conditions. A fixed frequency of 10^{-3} Hz was selected for both regions, as it has been shown that crack growth rates in C2 environments decrease with loading frequencies lower than 10^{-3} Hz [77, 92]. Therefore, the loading rates of the two regions vary to maintain the constant frequency. These regions were divided into blocks, where one block represents one CA cycle. There was a total of 691 blocks for Regions I and III.

Constant amplitude loading conditions can be compared to pressure fluctuations of oil pipelines as the incompressibility of liquid allows for large pressure fluctuations over short periods of time within pipeline sections. An in-depth statistical analysis of the loading and unloading frequencies of underload cycles in oil pipelines showed a frequency at the 50 accumulative percentage of 3.7 $\times 10^{-4}$ and 8.0×10^{-4} Hz, respectively, for loading and unloading cycles [79]. Using these loading characteristics, the 691 blocks run during the full-scale test translate to 15.8 days of service for oil-transmission pipeline operation.

3.4.2 REGION II & IV WAVEFORMS

Region II & IV waveforms were designed with UL&MC loading conditions. The goal of these pressure schemes was to study the enhancement of the crack growth rate (da/dt), if any, caused by the minor cycles. The number of MC per underload (n) was chosen to be 19, which was the value found to be the number of MC at the 80 accumulative percentage for gas pipelines [79]. A fixed frequency of 10^{-3} Hz was selected for the UL pressure fluctuation in both regions II & IV. Due to limitations of the pressure control system, the loading rate could not be manipulated within a region, thus the frequency of the minor cycles was fixed by the loading rate of the UL. These regions were divided into blocks, where one block represents one UL and the accompanying MCs ($n=19$). There was a total number of 805 blocks for Regions II and IV.

Underload and Minor Cycle loading conditions can be compared to pressure fluctuations of gas pipelines as gas media is compressible, thus pipeline sections remain at higher overall pressure with minor pressure fluctuations and only occasional underloading events occur. An in-depth statistical analysis of the loading and unloading frequencies of underload cycles in gas pipelines showed a frequency at the 50 accumulative percentage of 1.9×10^{-6} and 1.6×10^{-5} Hz,

respectively, for loading and unloading cycles [79]. Using these loading characteristics, the 805 blocks run in the full-scale test translate to 7.5 years of service for gas-transmission pipeline operation. This duration is largely skewed from the 83-days of testing time that these regions took as the loading rate used for the full-scale test was limited to 10^{-3} Hz by design. In addition to the explanation in **Section 3.4.1** above, a slower loading rate for the full-scale test was not possible as it would have increased the test duration beyond the time constraints available for the project.

3.5 END OF TEST PROCEDURE

The full-scale test was designed to ensure qualified personnel were present upon its completion. At the end of the test, the PCS was programmed to vent the pressure at a rate of 0.5 psi/s to prevent rapid depressurization. Once the pressure was safely relieved, the internal fluid was drained from the pipe. Throughout this procedure, a constant supply of CO_2 was purged through the boxes to maintain the anaerobic environment. The flow rate of CO_2 was greatly increased for this portion of the test to maintain positive pressure within the corrosion cells.

The boxes were emptied and removed from the pipe one at a time. First, the box was drained to create enough space for ethanol to be poured inside. The ethanol floated on top of the water, and as the box was drained from the bottom, the ethanol removed a significant amount of the water from the surface of the steel, inhibiting oxidation. While the C2 solution drained from the box, CO_2 flow was increased to maintain positive pressure inside the box, which prevented oxygen from entering and causing unwanted oxidation. When the water level reached the bottom of the pipe, the box was removed, and the pipe surface was rinsed with ethanol for several minutes and then was left to dry. This process was carried out for each box.

Once the boxes were removed, the pipe was transported to Petro-Line (PL) in Nisku, AB. Upon arrival to PL, the pipe was sandblasted with Enviro-Grit (EG) Glass Abrasive 12-50 to prepare the surface for ECHO-3D inspection and MPI. After sandblasting, the pipe was housed indoors to prevent any further corrosion.

ECHO-3D inspection was conducted prior to MPI as per the request made by Athena Industrial Services. The magnetic particulate used during MPI was known to interfere with the precision of ECHO-3D testing as it is an EMF-based technology. Next, black on white MPI was performed by a CGSB MT 2 certified technician from IRISNDT to re-locate the external SCC colonies on the pipe segment and inspect the dents for any external cracks. SCC colonies that were identified and numbered prior to the full-scale test were re-drawn on the pipe. An image of the pipe at this stage in the post-test analysis is shown in **Figure 3.10**. Finally, the pipe was cut into pieces weighing approximately 25 kg, as shown in **Figure 3.11**, and transported back to the University of Alberta for characterization.

Figure 3.10   Pipe segment after post test NDE.

Figure 3.11   Pipe segment cut into small sections after completion of the full-scale test.

3.6 CHARACTERIZATION

The following section describes the methods and equipment used to characterize the cracks in the pipe segment before and after testing.

3.6.1 PRE-TEST CRACK IDENTIFICATION

Previously it was stated that the pipe segment was cut-out after an integrity assessment in February 2015. During the integrity assessment, 40 SCC colonies were identified on the 13.61 m joint. Of these colonies, seven were identified as significant SCC and were ground out for depth collection; the remaining colonies were left in the joint. A 4.77 m section was cut from the joint and 13 SCC colonies were identified using MPI and were mapped out on the pipe. The location of the SCC colonies are shown in **Figure 3.12**. SCC colonies 2 – 5 and 7 – 11 were then inspected by ECHO-3D. SCC colonies 1, 6, 12 and 13 were not inspected as they were located within three pipe diameters of the end caps. The results of the pre-test inspection are summarized in **Table 3.7**.

Table 3.7　　　　Pre-test SCC colony depths collected during the ECHO-3D inspection.

SCC Colony	Maximum Crack Depth (mm)
2	2.0
3	0.8
4	0.58
5	1.3
7	2.1
8	1.2
9	0.68
10	0.64
11	0.51

3.6.2 POST-TEST CRACK IDENTIFICATION

After the full-scale test was completed and the pipe was transported to Petro-Line, the pipe was sandblasted, and another round of ECHO-3D inspection was carried out to identify areas of crack growth in the pipe segment.

Unfortunately, the Athena Industrial Services technician conducted the post-test inspection before the pipe was marked up with the SCC colony boundaries used in the pre-test inspection. This resulted in a large degree of uncertainty when comparing the pre-test inspection data with the post-test inspection data as it was unclear if the scan areas in the post-test inspection were the same as
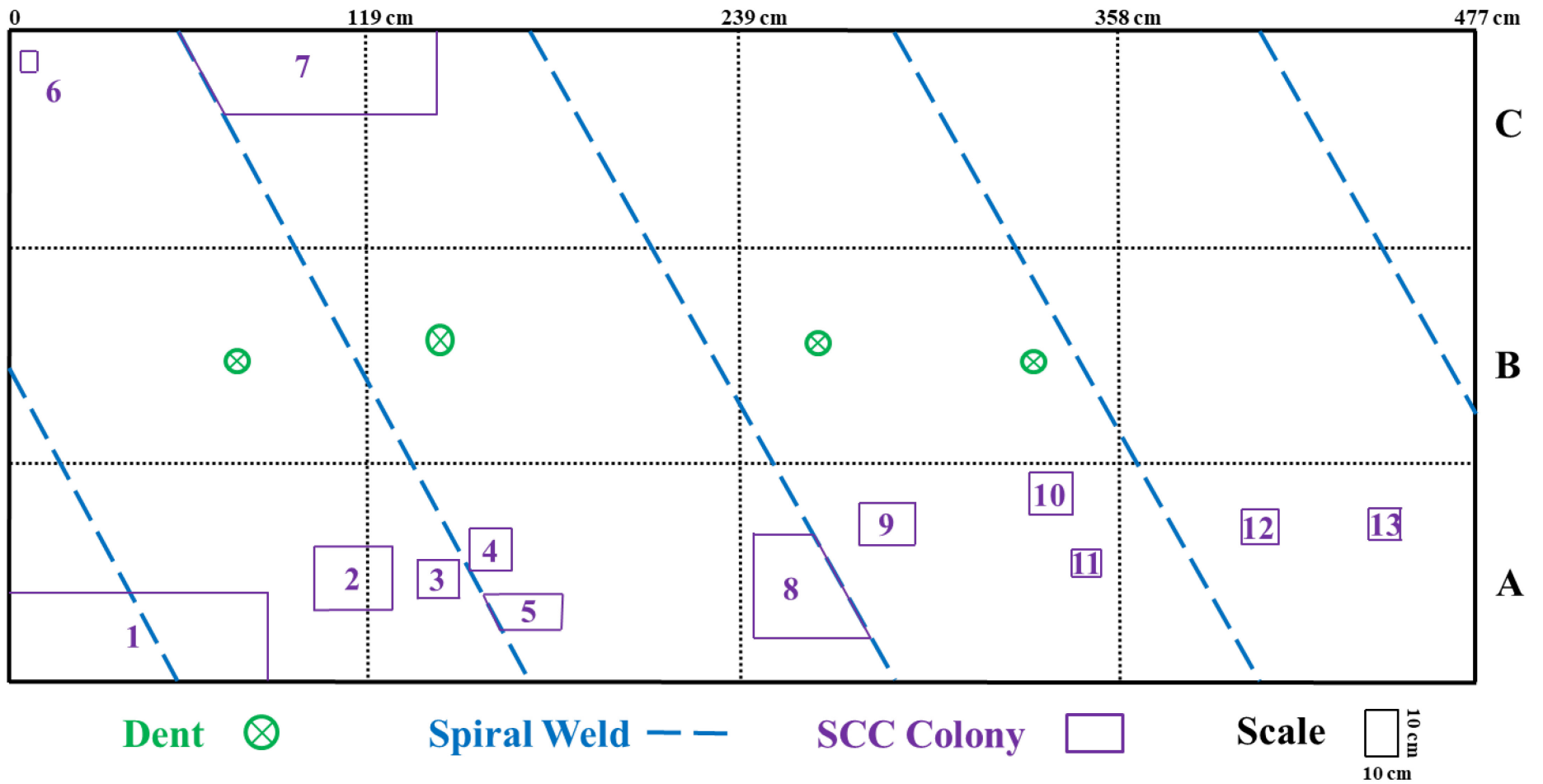
Figure 3.12 Diagram of the pipe outer surface illustrating the boundaries of the SCC colonies and dents.

79

the original scan areas. Additionally, the post-test inspection report was provided two months after the post-test inspection. Therefore, some samples were prepared prior to the receiving the report. Consequently, this form of non-destructive examination was inconclusive in determining if any areas of crack growth were present.

After the ECHO-3D inspection was conducted, MPI was performed and the SCC colonies identified prior to the full-scale test were mapped on the pipe. The pipe was cut into multiple sections, as described in **Section 3.5**, and the SCC colonies were visually examined to determine which cracks would be selected for further characterization. The cracks were marked into sections and sent to the University of Alberta CME machine shop to be cut using a band saw as seen in **Figure 3.13** prior to cutting. After the marked-up sections were cut from the pipe, they were further reduced using a Cantek UE-712 horizontal metal cutting bandsaw to prepare the samples for cross-sectional analysis. An individual sample at this stage of analysis is shown in **Figure 3.14**. Cracks exposed to the corrosive environment and the atmospheric environment were selected for characterization.
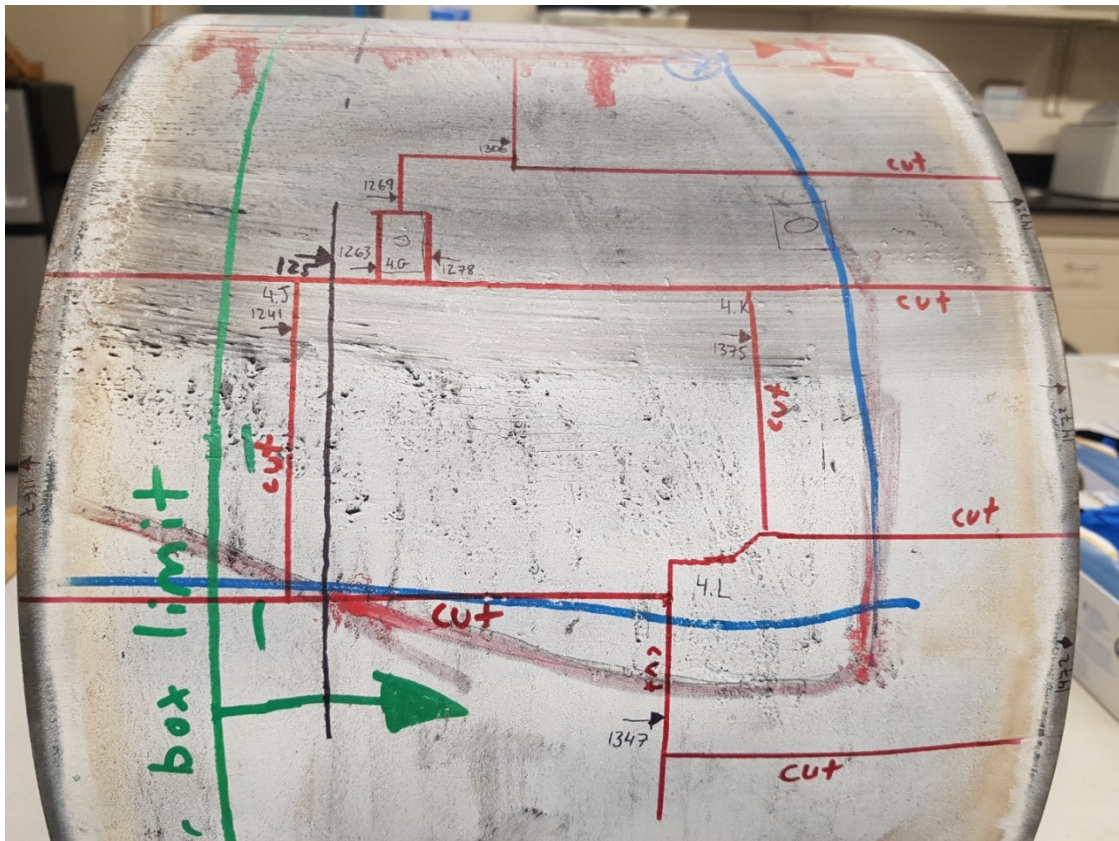
Figure 3.13   Post-test section of pipe after MPI, multiple SCC colonies marked up for cutting.
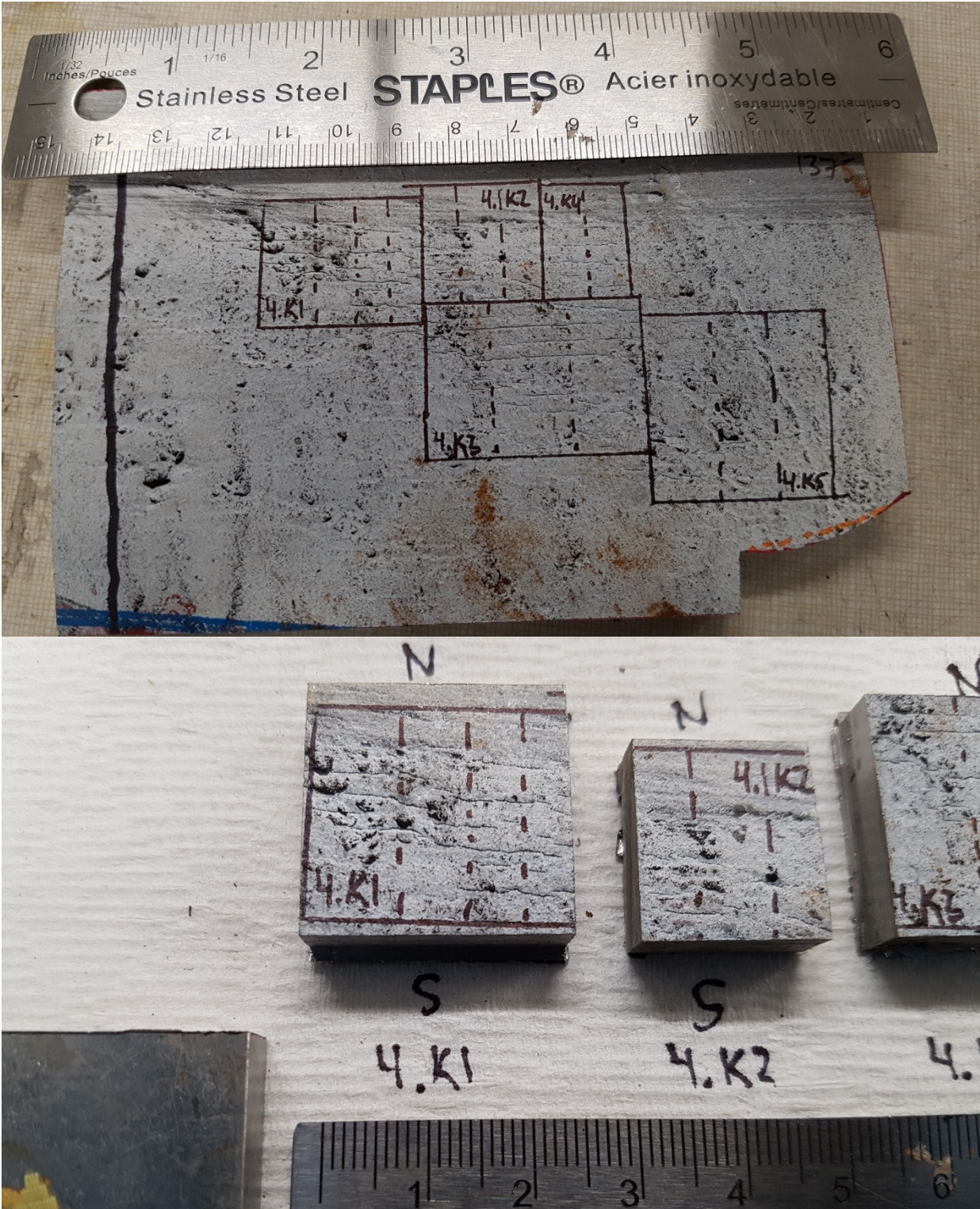
Figure 3.14 (Top) a group of cracks cut out using a commercial band saw and (bottom) individual cracks prior to cross-sectional analysis.

3.6.3 CROSS SECTION CHARACTERIZATION

To characterize the depth of the cracks, the samples were sectioned perpendicular to the crack length using a Mecatome T180 precision micro-cutting machine mounted with an IsoCut Cubic Boron Nitride wafer blade manufactured by Buehler (Item # 115265) capable of a cutting width of 0.4 mm. Effort was made to avoid cutting the cracks at their deepest point by offsetting the cut from the centre of the crack length. The cross-sectional surfaces were then ground with increasing grits of SiC grinding paper in a criss-cross pattern to an 800-grit finish to prepare the surface for low-magnification imaging. The grinding was done dry without lubricant to prevent oxidation. The final grinding direction was made perpendicular to the cracks. Before and after width measurements of the samples were taken to determine the amount of material loss from the blade during cutting and material loss from grinding. Total material loss from cutting the sample with the precision cutter and grinding both surfaces was 0.54 ± 0.07 mm using the mean and the standard deviation of the measured material loss of all prepared samples (*n=52*).

After grinding, the cracks were cleaned to remove the paint, magnetic particle slurry, and other contaminates from the steel surface by placing them in an acetone ultrasonic bath for one hour. The cracks were then moved into an ethanol bath for at least 24 hours. In the ethanol bath, the specimens were placed diagonally, and the cracks were oriented downwards so that any remaining acetone or contaminants remaining in the crack opening could be removed by gravity. Finally, the samples were dried using compressed air and periodically sprayed with ethanol to remove any films left behind during the evaporation process.

After cleaning, the crack cross sections were imaged along the entire cross section using a Zeiss Sigma 300 VP – FESEM at low magnifications in secondary electron (SE) imaging mode. The individual images were stitched together using Image J-2. A sample cross-sectional image after stitching is shown in **Figure 3.15**. Cracks selected for further analysis were chosen based on their observed depth and their distance relative to each other within the cross-section.
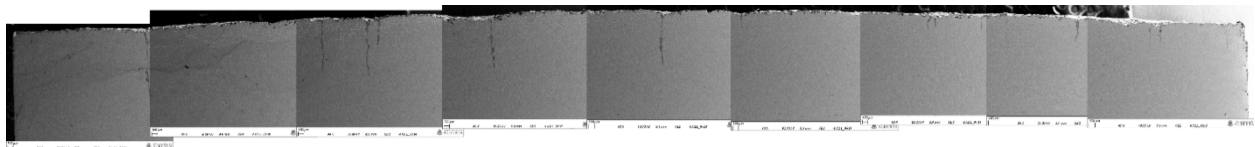
Figure 3.15   Cross-sectional SEM image of SCC taken in SE mode.

3.6.4 FRACTURE SURFACE CHARACTERIZATION

To characterize the fracture surface, the cracks had to be carefully split open. First, to facilitate a clean fracture, the specimen dimensions were limited to a minimum 2.5 to 1 length to width ratio. The crack selected for fracture also had to be located at least 5 mm from the specimen's edge. The selected crack also required a minimum spacing from any other cracks equal to its depth. The specimens were then slotted from the inner diameter (ID) pipe surface to ensure a flat fracture. Then, the samples were placed in liquid nitrogen for at least three hours, removed and immediately fractured open by striking the ID slot with a cold chisel. The two halves were immediately placed in an ethanol bath to minimize oxidation of the crack face.

The two crack faces were imaged at low magnification using a Zeiss Sigma 300 VP – FESEM in both SE and backscattered electron (BSE) modes. The first goal with this imaging was to photograph the entire crack face to observe its dimensions and obtain the aspect ratio. The second goal was to locate and image any striations that were present on the crack face of both the samples exposed to the corrosive environment and the samples exposed to atmospheric conditions to identify crack growth regions that occurred when the pipe was in service. The third goal was to locate and image the crack growth regions unique to the samples exposed to the corrosive environment and measure the growth contribution that each of the four loading conditions made on the overall crack growth during the full-scale test.

After the initial imaging described above was complete, the corrosion products were gradually removed from the crack face by etching. The goal of this process was to remove the thin corrosion product that formed on the new crack growth region during the full-scale test, without removing the thick corrosion product that formed during field service. This was done by dipping the fracture surface into a mixture of 6N HCl + 3.5 g/L hexamethylene tetramine, a solution commonly used for steel corrosion product removal that can be found in ASTM Standard G1-03 [115]. The samples were quickly submerged in the solution and immediately removed and immersed in an ethanol bath. Care was taken in this step as any length of holding period in the acidic solution was found to cause significant damage to the steel crack surface. It was determined that three to six submersions with no holding period were enough to remove the newly formed corrosion product and begin to expose the bare metal surface without damaging that surface.

Attempts were made to characterize the corrosion products on the fracture surface using energy dispersive X-ray spectroscopy (EDS) chemical analysis. A Zeiss Sigma 300 VP – FESEM equipped with a Bruker EDS system with dual silicon drift detectors, each with an area of 60 mm^2 and a resolution of 123 eV, was used with an accelerating voltage of 20.0 kV. Point analysis and area mapping of the corrosion products on the crack face were conducted; however, no significant variation in the composition of the corrosion product layers could be determined.

3.6.5 TEST SOLUTION ANALYSIS

The *pH* measurements were performed using a Fisher Scientific Ag/AgCl liquid-filled *pH*/ATC epoxy body combination electrode (Model # 13-620-530A) and a Fisher Scientific XL60 *pH* meter (Model # 13-636-XL60). Prior to each measurement, the meter was calibrated using 4, 7 and 10 *pH* standard buffer solutions. Measurements were taken prior to adding solution to the boxes, throughout the test at an interval of five days, and at the end of the test. The *pH* measurements were taken immediately after removing a 10 mL sample from the anerobic environment, as the *pH* of the solution would increase rapidly once it was removed from the anaerobic environment. The *pH* electrode was rinsed between each measurement to prevent cross-contamination of the buffer solutions and the test solutions.

CHAPTER 4: RESULTS

The following chapter will present the results of the full-scale test that will be used for discussion in **Chapter 5**. First, the pressure data that was collected throughout the full-scale test will be examined. Next, the results of crack initiation on the dents will be briefly presented. Finally, the crack depths, sidewall morphology and growth rates will be characterized.

4.1 TEST PRESSURE DATA

The full-scale test was divided into four pressure fluctuation regions defined in **Table 3.5** and the instantaneous pressure (P_{ins}) was recorded each second for the duration of the full-scale test using the equipment described in **Section 3.3**. The pressure data spanning the full test duration, sampled at 30 second intervals and converted to % SMYS is plotted in **Figure 4.1**. Plots of the pressure data over the full test duration using smaller time intervals can be found in **Appendix A**. Conversion of P_{ins} to % SMYS was done using the following equations:

$$\sigma_h = \frac{P_{ins}d}{2t} \quad \textbf{Equation 4.1}$$

$$\% \, SMYS = \frac{\sigma_h}{\sigma_{SMYS}} \quad \textbf{Equation 4.2}$$

where σ_h is the hoop stress, d is the pipe OD, t is the pipe wall thickness and σ_{SMYS} is the specified minimum yield strength or the material. For a closer look at the pressure fluctuation data, each region is plotted in **Figure 4.2-Figure 4.5**, where a ten-hour sample of pressure data that conforms to the target pressure (P_t) with a five second sampling interval is used.
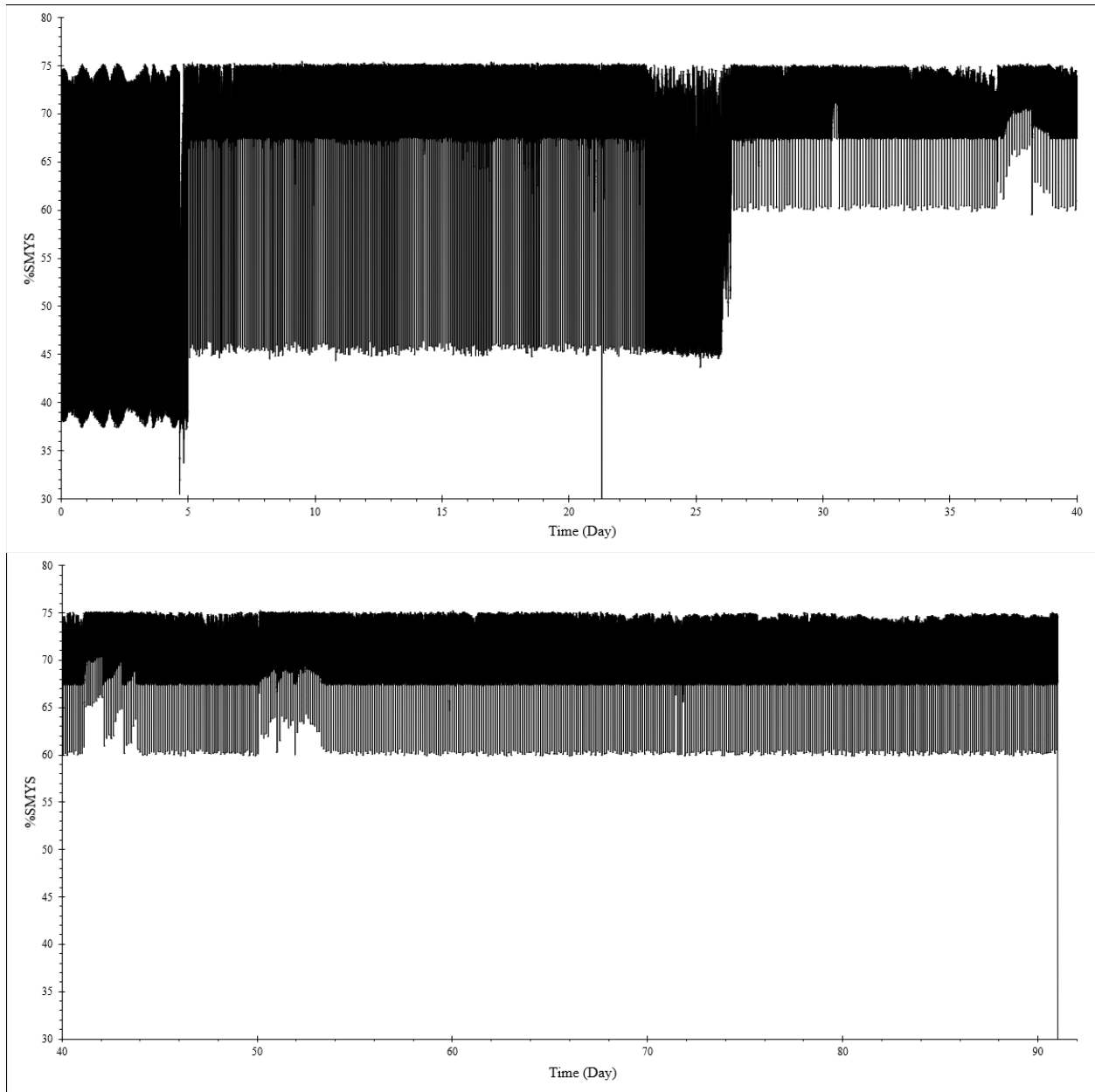
Figure 4.1   Pressure data collected during the full-scale test for (top) day 0–40 and (bottom) day 40–91. The dark black zones of the plot are the areas of CA fluctuation or zones of MC. The UL fluctuations can be seen in the areas of Region II and IV below 67.5 % SMYS.
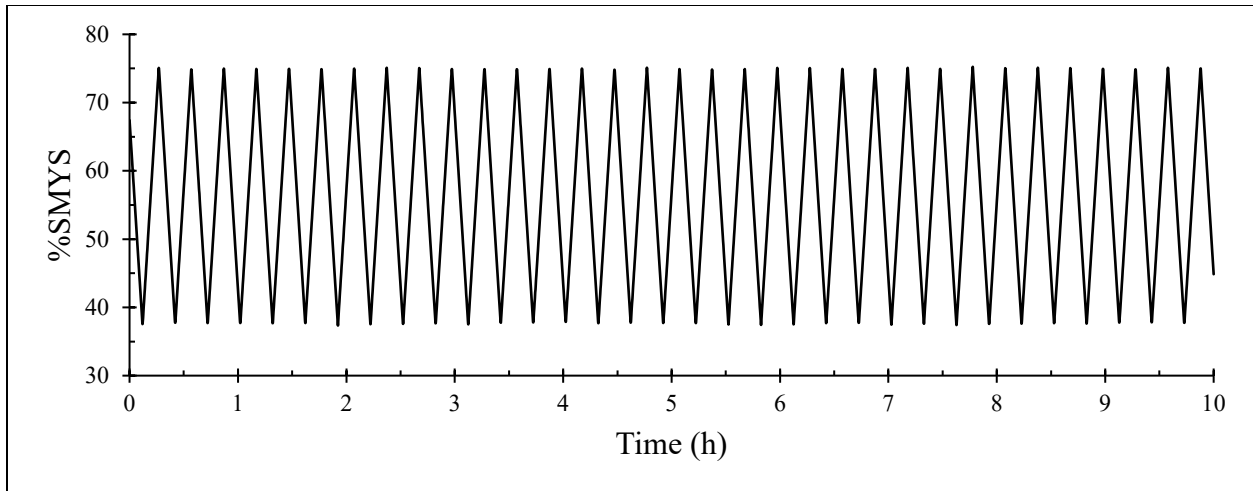
Figure 4.2   Ten-hour sample of Region I pressure data from the full-scale test using a five second sampling interval (P_{max} = 8.62 MPa, f = 0.001 Hz and R = 0.5).
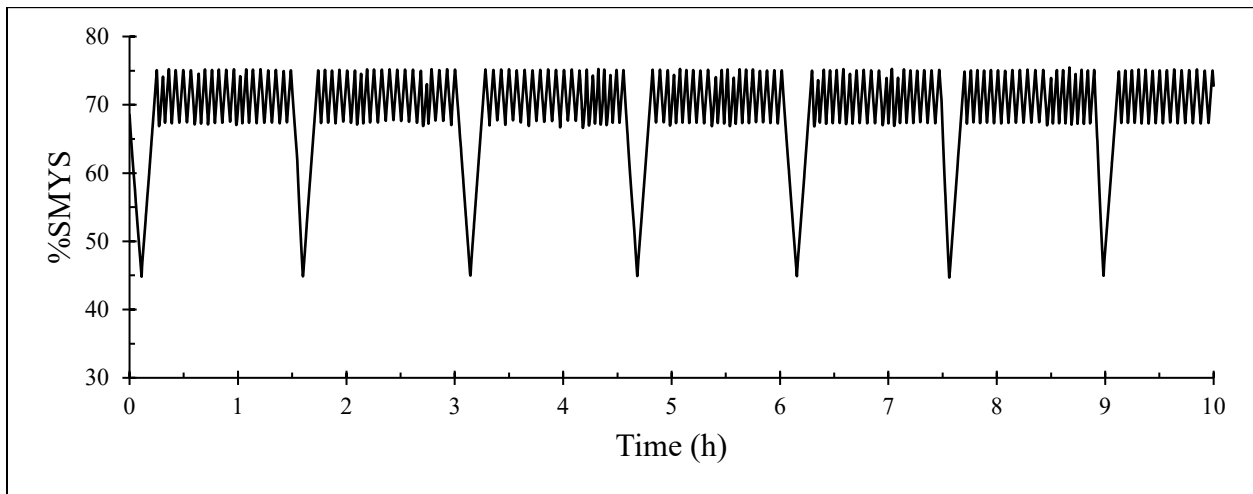
Figure 4.3   Ten-hour sample of Region II pressure data from the full-scale test using a five second sampling interval (P_{max} = 8.62 MPa, f_{UL} = 0.001 Hz, R_{UL} = 0.6 and R_{MC} = 0.9).
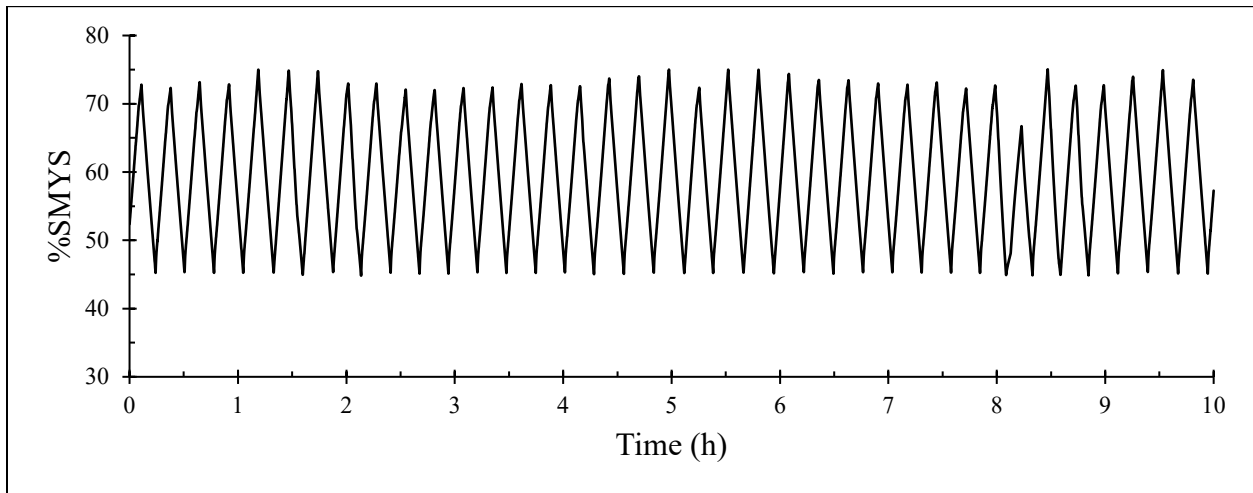
Figure 4.4   Ten-hour sample of Region III pressure data from the full-scale test using a five second sampling interval (P_{max} = 8.62 MPa, f = 0.001 Hz and R = 0.6).

87
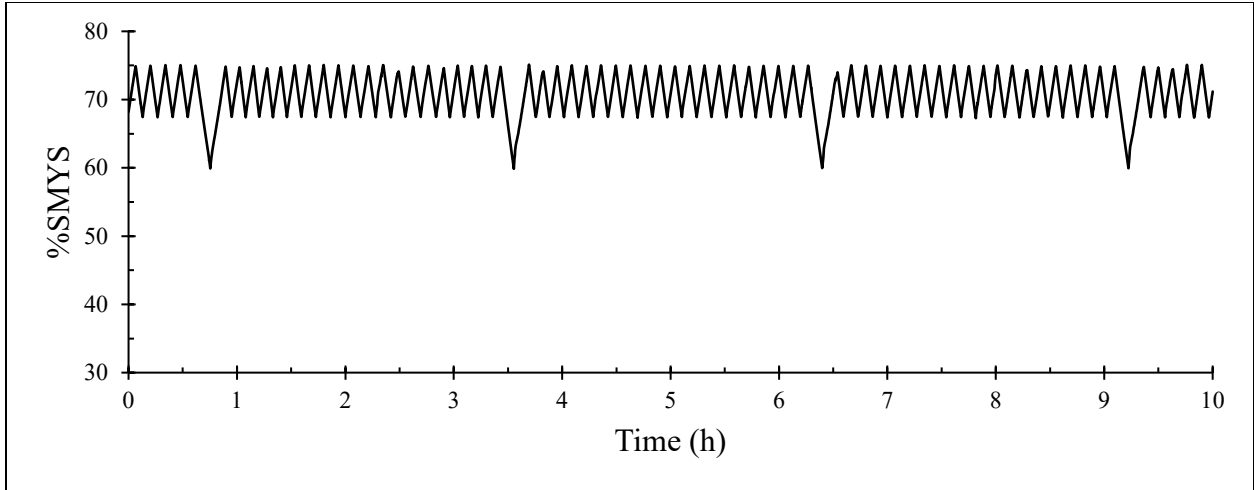
Figure 4.5 Ten-hour sample of Region IV pressure data from the full-scale test using a five second sampling interval (P_{max} = 8.62 MPa, f_{UL} = 0.001 Hz, R_{UL} = 0.8 and R_{MC} = 0.9).
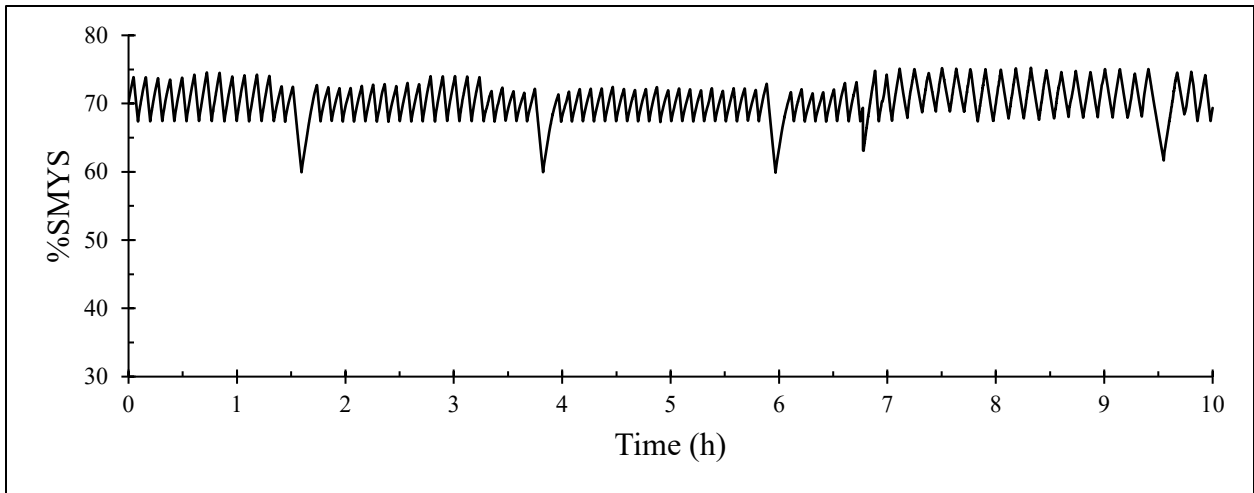
Figure 4.6 Ten-hour sample of Region IV pressure data using a five second sampling interval showing deviation from the target pressure (P_t) in the first eight hours.
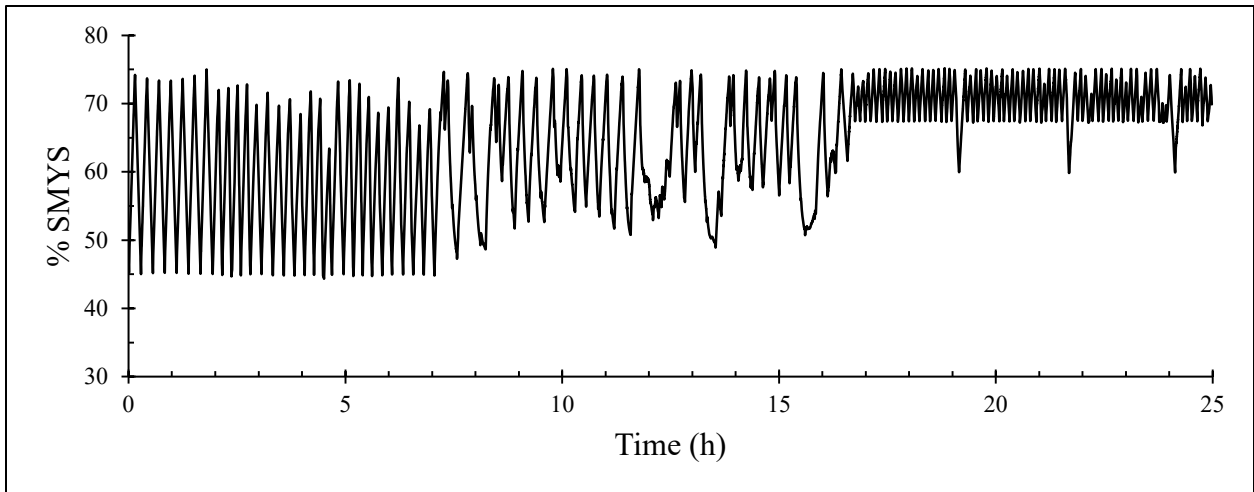
Figure 4.7 One-day sample of pressure data using a five second sampling interval showing deviation from P_t caused by the transition from Region III to Region IV.

88

The pressure control system was designed to maintain the interval between each target P_{max} and P_{min} at all costs. As a result, if the loading rate fell behind the target rate for that loading or unloading event, P_{ins} would not reach P_t in the allotted time for that cycle. Analysis of the pressure data shows that $P_{ins} = P_t$ was achieved for > 95 % of the test time. Occasionally, the pressure control system would not maintain the loading or unloading rate, as can be seen through careful examination of **Figure 4.1** (and is evident in **Appendix A**). A closer look at two test intervals where $P_{ins} \neq P_t$ are shown in **Figure 4.6-Figure 4.7**. The transition from Region III to Region IV (**Figure 4.7**) caused the pressure control system some difficulty, potentially related to the sudden change in loading rate (Region IV had a 50 % slower loading rate than Region III). Additionally, there were two scenarios responsible for the desired pressure deviation throughout the test:

i.   The air-driven pump was known to occasionally stall during operation. Specifically, the piston in the pump would lock at the top of its revolution within the cylinder, not fully thrusting to produce the required flow rate and pressure gain. This was mostly observed in Region IV of the test and was attributed to the low air flow throughput at the pump intake required for the lower loading rate. This could be prevented in future work by either altering the test design to accommodate higher air flow rates or choosing a pump that can operate at a lower air flow rate. This series of events occurred to cause the pressure deviation shown in **Figure 4.6**, when the pressure control system could not maintain the target loading rate.

ii. The solenoid valve controlling the depressurisation would get stuck in the open position, and the pump was not able to provide enough pressure to compensate. This occurred most often towards the end of Region I and sporadically throughout Regions II and III. The cause could be attributed to the more aggressive loading rates of these regions. It was likely that the accumulation of small particulate in the valve prevented it from fully closing. Emergency maintenance of the pressure control system was required to remediate this problem on day 21, which involved full depressurization of the system. This problem could be prevented in future work by substituting the solenoid valve for an air-to-open research control valve (with an appropriate C_v), as used in this test to control the air supply to the pump.

4.2 DENT CHARACTERIZATION

Four dents were machined into the pipe segment and information regarding the dents is presented in **Table 4.1**. Dents A, B and C were located within the corrosion cells and exposed to NNpH environmental conditions. Dent D was on a portion of the pipe exposed to the atmospheric environment and was visible throughout the test. After the test was initiated and internal pressure had developed, Dent D immediately rebounded to such an extent that it was no longer visible. When the internal pressure of the test was relieved Dent D became visible again but did not return to its original depth. All four dents exhibited rebound with final depths ranging 61 – 67 % of their respective initial depths; therefore, it is reasonable to assume the other three dents (hidden from view) fully rebounded to the same extent as Dent D during testing. After the test had run its course and was de-pressurized, magnetic particle inspection was carried out on the dents. External surface breaking flaws were not detected near any of the dents from this inspection.

Table 4.1   Dent environment, coating and depth information.

Data Type	Dent A	Dent B	Dent C	Dent D
Environment	NNpH	NNpH	NNpH	Air
Simulated disbonded coating (Y/N)	N	Y	N	N
Pre-test dent depth [mm (% OD)]	8 (1.7)	9 (2.0)	8 (1.7)	8 (1.7)
Post-test dent depth [mm (% OD)]	5.1 (1.1)	6.0 (1.3)	4.9 (1.1)	5.2 (1.1)

4.3 CRACK CHARACTERIZATION

The SCC colonies studied in this work initiated and grew while the pipe segment was in gas transmission field operation for 46 years. The following sections will present the characterization of the cracks taken from the full-scale test pipe body. The fracture surface will be examined, and the regions of the fracture surface attributed to crack growth in the field will be established. Next, the region attributed to crack growth during the full-scale test will be shown. Finally, the total number of cracks analyzed, and their dimensions will be given.

4.3.1 INITIAL CRACK ANALYSIS

Low magnification SEM images of the fracture surface of cracks exposed to the NNpH environment and atmospheric conditions throughout the full-scale test are shown in **Figure 4.8a** and **Figure 4.8b**, respectively. Each image contains three crack growth zones, separated by distinctive bands in the corrosion product, and the fracture surface produced by brittle fracture in liquid nitrogen can be seen.
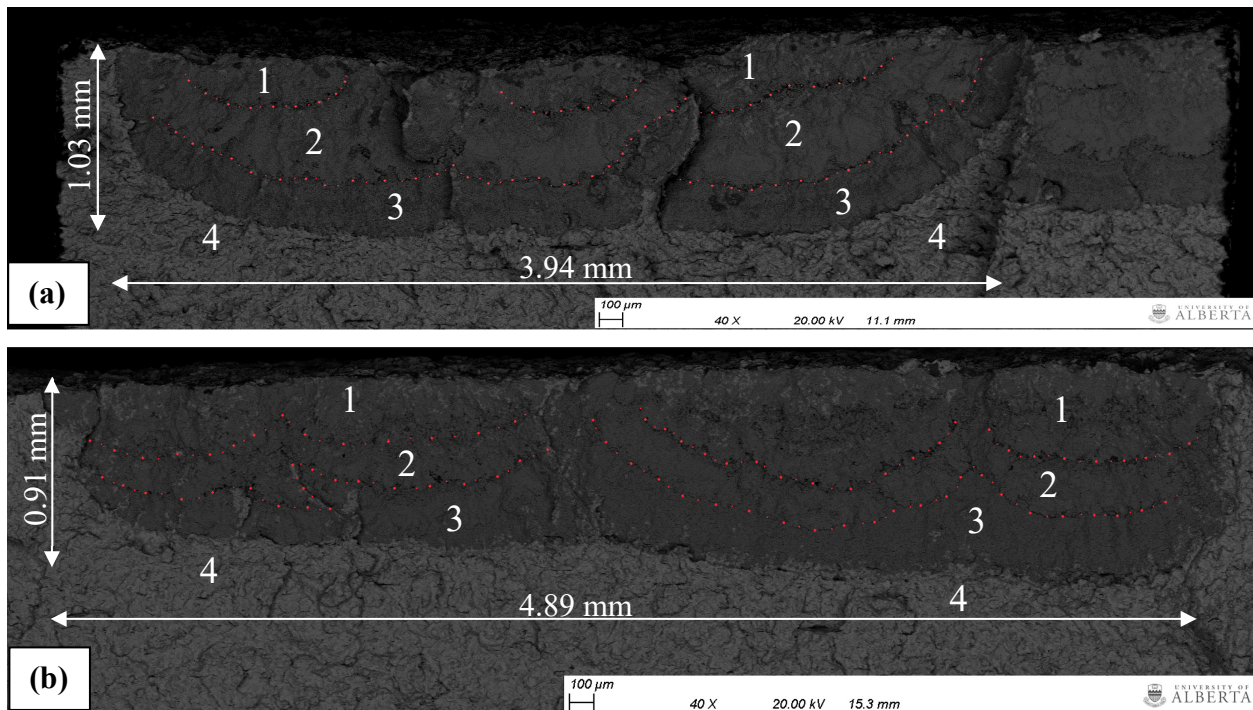
Figure 4.8 SEM images of the crack fracture surface exposed to (a) the NNpH environment and (b) atmospheric conditions during testing. The regions identified in both images are: three crack growth zones attributed to growth in the field, denoted 1-3, and the brittle fracture surface produced from fracture in liquid nitrogen, denoted 4. The crack growth zones are separated by bands enhanced with red dotted lines.

It should be noted that cracks fractured open and found with depths less than 0.5 mm were discarded and not considered for further analysis. after this criterial was applied, 57 cracks were analyzed, and their dimensions are plotted in **Figure 4.9**. Of these cracks, 56 were found with three crack growth zones (or less for very shallow cracks). The three growth zones were common to the cracks subjected to both environments and across a wide range of crack dimensions; therefore, all three were attributed to crack growth in the field prior to the full-scale test and if growth occurred during the test a fourth band would be visible. The fracture surface of all 57 cracks were analyzed to locate a fourth growth zone, and one crack was found. The image of the crack face with corrosion product on the surface can be seen in **Figure 4.10**.

It was theorized that the corrosion product covering the growth developed in the field was significantly thicker than any that would have formed during full-scale testing due to the short exposure time of the new growth to the corrosive environment. Etching was performed to remove the thin layer of corrosion product covering the new crack growth. Unfortunately, this specimen was damaged during the etching process and high-resolution images of the crack face morphology were unable to be obtained.

As the only images available for this crack face were low resolution shots of the fracture surface with corrosion product, unique morphologies that could be attributed to the four pressure fluctuation regions of the full-scale test could not be determined. Division of the growth zone was found to be largely user dependent and strongly subject to interpretation, consequently introducing a significant error bias. Additionally, it was unclear at what moment during the full-scale test the re-initiation and growth of the crack occurred. Therefore, the total growth zone was evenly attributed to all four pressure fluctuation regions and it was assumed that crack growth began at the start of the test and continued at a steady state throughout the test. Discussion regarding this assumption including its justifications and limitations are given in **Section 5.1.5**.
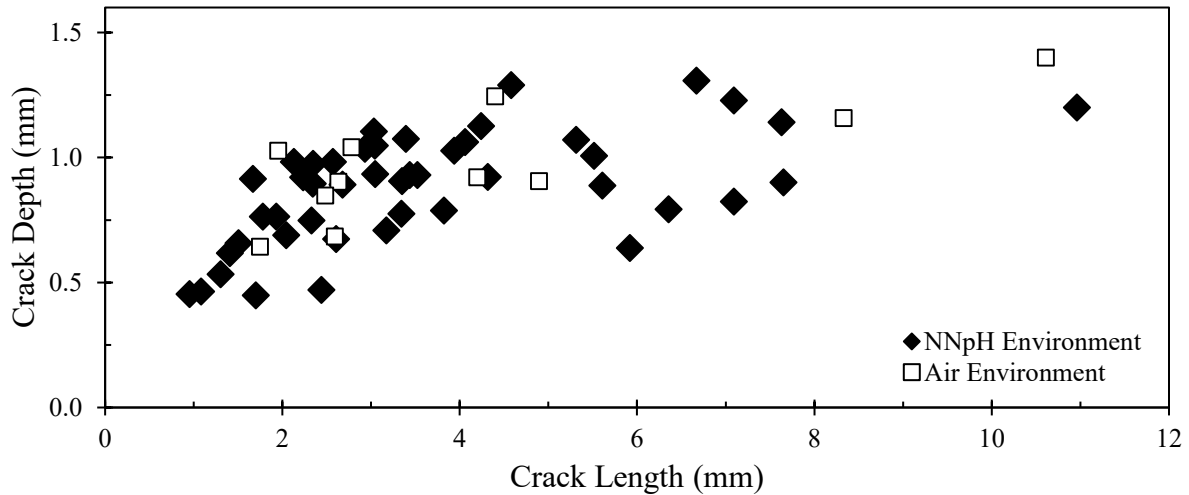
Figure 4.9   Individual crack depth as a function of crack length for the 57 cracks analyzed after testing.
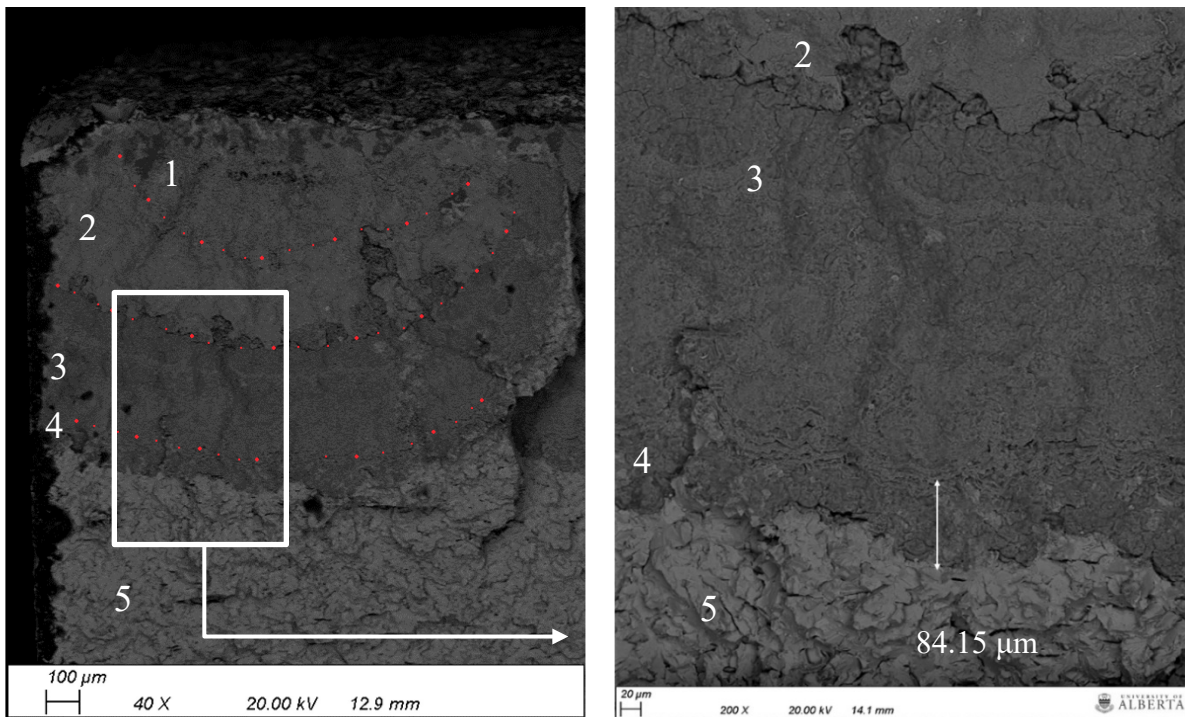
Figure 4.10   Crack fracture surface exposed to the NNpH environment during testing. Three crack growth zones attributed to growth in the field (1-3); one crack growth zone attributed to growth during the full-scale test (4); and brittle fracture in liquid nitrogen (5). The crack growth zones are separated by bands enhanced with red dotted lines.

4.3.2 ADDITIONAL CRACK ANALYSIS[1]

Additional crack analysis was undertaken to locate other cracks that experienced growth during the full-scale test. 186 cracks were analyzed following the procedure given in **Section 3.6.4** and

---

[1] Results presented in this section were obtained by Dr. Zhezhu Xu.

93

five cracks were found with a fourth distinctive crack growth zone, for example, as shown in **Figure 4.11**. Even though the etching process was successful, it was still not possible to separate the growth zone into the four pressure fluctuation regions. Therefore, the assumption introduced in **Section 4.3.1** was adopted for all cracks that were found with growth during testing.

Due to the unpredictable nature of the brittle fracture method used when opening the cracks to view the fracture surface, sometimes only part of the fracture surface would be exposed. These partial cracks were removed from the crack size data. Additionally, representative cracks were selected from crack groupings with similar dimensions to reduce the data contained within the plot. The crack dimensions selected as an accurate representation of the total dataset are shown in **Figure 4.12**.
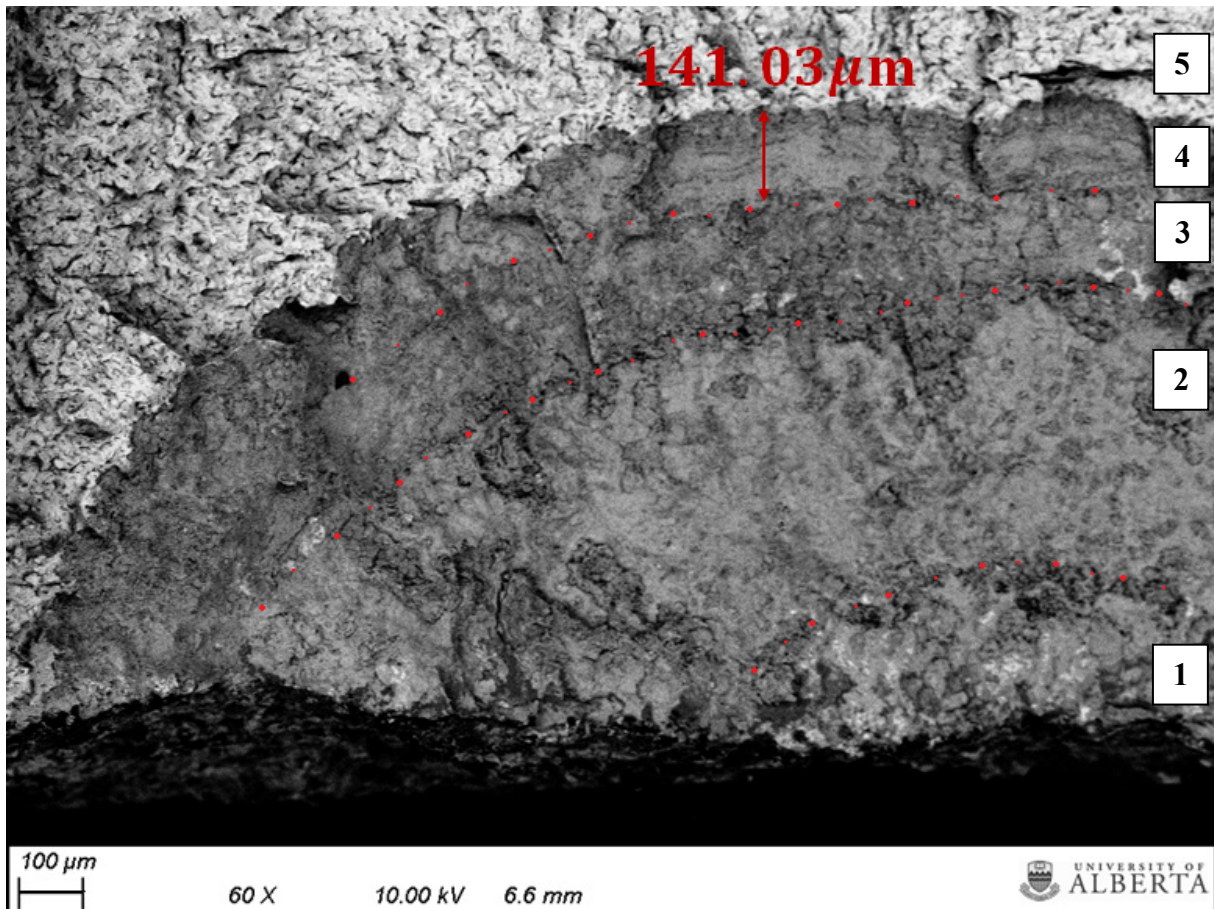
Figure 4.11 Etched crack fracture surface exposed to the NNpH environment during testing. Three crack growth zones attributed to growth in the field (1-3); one crack growth zone attributed to growth during the full-scale test (4); and brittle fracture in liquid nitrogen (5). The crack growth zones are separated by bands enhanced with red dotted lines.
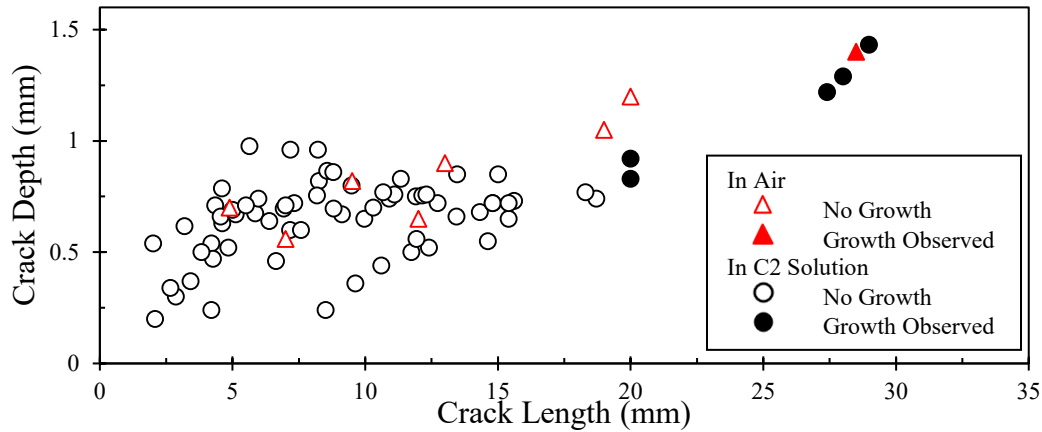
Figure 4.12   Crack dimensions of the cracks analyzed from the full-scale test.

4.3.3 CRACK SIZING SUMMARY

During controlled laboratory testing, cracks are carefully initiated, and crack coalescence is not of concern. When considering crack coalescence, ideally cracks coalesce on one longitudinal plane. However, crack coalescence in the field is an uncontrolled process, leading to the formation of cracks in orientations deviating slightly from the longitudinal direction. When fracturing the cracks from the full-scale specimen in liquid nitrogen, some cracks arbitrarily fractured in a way that only partially exposed the fracture surface. This occurred when the path of least resistance to the brittle fracture was not in-line with the full length of the crack.

A total of 243 cracks were analyzed in **Section 4.3.1** and **Section 4.3.2** and six (2.5 % of the total cracks) were found with growth attributed to the full-scale test. Unfortunately, two of the cracks were only partially fractured so their lengths were assumed to be 20 mm as there were so few cracks found with growth that none could be discarded. The final crack lengths ($2c$), depths (a), environments, and their growth (Δa) attributed to the full-scale test are shown in **Table 4.2**.

Table 4.2   Final crack dimensions, measured growth and testing environment.

Crack	$2c$ (mm)	a (mm)	Δa (mm)	Testing Environment
1	27.40	1.22	0.141	C2 Solution
2	28.98	1.43	0.119	C2 Solution
3	20.0[2]	0.83	0.111	C2 Solution
4	20.0[3]	0.92	0.084	C2 Solution
5	28.00	1.29	0.090	C2 Solution
6	28.50	1.40	0.046	Air

[2] This was a partial crack with a measured length of 8.49 mm. A total length of 20 mm was assumed.
[3] This was a partial crack with a measured length of 9.12 mm. A total length of 20 mm was assumed.

95

CHAPTER 5: DISCUSSION

Crack growth during the full-scale test did not occur as expected. Consequently, the discussion regarding Stage 2 crack re-initiation and conclusions that can be made are limited. The following chapter will discuss the results of the full-scale test that led to the conclusions listed in **Chapter 6**. First, the full-scale test design will be reviewed, and improvements will be recommended. Next, there will be a short discussion regarding the results on the study of crack initiation in dents. Finally, discussion regarding the limited results of the full-scale test will be presented.

5.1 TEST DESIGN

The following sections will discuss the experimental methods of the full-scale test. Recommendations for improving these procedures will also be provided where applicable. Additionally, the assumptions made during the design of the test and that were used for the limited discussion will be given.

5.1.1 FULL-SCALE SPECIMEN

During the test design, two assumptions were made regarding the pre-existing longitudinal SCC in the full-scale specimen:

i. *Mechanically short cracks*

Cracks observed by destructive testing were usually less than 1 mm deep. Cracks with depths less than 1 mm are usually not a concern to the integrity of pipeline steels, and crack detection at these depths is not reliable with current ILI technology [116]. These cracks are categorized as mechanically short cracks according to fracture mechanics theory [117]. Fracture mechanics can be used to predict the growth of mechanically short cracks, and the growth is usually found to be faster than long cracks subjected to the same loading conditions [118]. To simplify this problem, the growth behaviour governing long cracks was applied to the growth behaviour of short cracks and it was assumed that crack growth was in the Stage 2 regime of hydrogen-dominant continuous growth.

ii. *Different stress states*

The plastic zone ahead of the crack tip for surface cracks and through-thickness cracks are subject to different stress states. As the surface cracks of the full-scale specimen are not through-thickness, the plastic zone should be entirely in a plane strain stress state. Conversely, CT specimens consist of through-thickness cracks that are in a plane strain stress state. The maximum stress in the plastic zone for the surface cracks (plane strain) and through-thickness cracks (plane stress) reaches $3\sigma_{YS}$ and σ_{YS}, respectively [119]. However, the plastic zone size of the plane strain state is $\sim$ 1/6 the size of the plastic zone in plane stress state, causing less overall hydrogen accumulation in the plastic zone of the former. Therefore, despite the lower maximum stress created in the plastic zone of CT specimens, fracture is mechanically more favourable than the fracture of surface cracks for a given K_{max} due to the effect of hydrogen. This theory is physically demonstrated by comparing the crack growth rates of CT and SCT specimens in **Figure 2.16**.

To predict the crack growth of the full-scale test, a crack growth model developed for NNpH environments was required and the combined factor equation was selected. This empirical equation was modeled using crack growth in CT specimens under constant amplitude loading [85, 86]. Therefore, it was necessary to assume that the longitudinal surface cracks in the pipe would exhibit similar crack growth rates as the through-thickness CT specimen crack.

Neither the Stage 2 regime assumption, nor the stress state assumption could be dismissed when considering factors that affected the test results. The former caused a lower predicted crack growth rate than expected, while the latter predicted the opposite effect. Therefore, it was difficult to confirm the impact of the assumptions on the full-scale test results.

Additional consideration was made regarding the effect of sandblasting on surface crack initiation and pre-existing crack re-initiation in the full-scale specimen. After sandblasting, the steel surface is damaged by erosion, which causes minor plastic deformation in the material [120]. However, the damage is mitigated by the compressive residual stresses introduced due to local irreversible deformation from the high velocity impact of the media [121-123]. The exponential decay of defect concentration with increasing depth from the surface is observed in many materials after sandblasting. This defected zone thickness can be used to determine the depth of the compressive

residual stress. For example, the defected zone of stainless steel after sandblasting was reported to be less than 1 μm below the surface [124, 125]. The defected zone of pure aluminum and 6082-T6 aluminum alloy was found to reach 300 μm below the surface [126]. Another method used in the literature to quantify the depth of the affected material is to measure the micro-hardness of the material. Using this method, Ding *et al.* [127] found that the maximum deformed thickness for carbon steel after sandblasting was 45 ± 10 μm.

Clearly, the depth that the compressive residual stress penetrates the thickness is highly dependent on the material and is also affected by the sandblasting media particulate size, air pressure and impact angle used. As discussed in **Section 2.6.3.1**, SCC is known to favourably initiate in areas of high tensile residual stress. Therefore, the overall effect of sandblasting improves the surface resistance of steel to SCC initiation. If the compressive residual stress penetrates the specimen deep enough to reach the plastic zone ahead of the pre-existing crack tips, crack re-initiation would have certainly been affected. However, based on the discussion above, the extent of affected material does not extend further than 100 μm. Therefore, sandblasting is unlikely to affect crack re-initiation at crack depths greater than 0.1 mm.

5.1.2 CORROSION CELL AND ENVIRONMENT

The effectiveness of the corrosion cells (boxes) used to seal the contents from atmospheric conditions, contain the C2 solution and support CP was evaluated by monitoring three factors:

i. *Gas flow rate*

Each box was its own self-contained anaerobic environment. The de-oxygenated state within the boxes was maintained by bubbling a 5 % CO_2 + 95 % N_2 gas mixture. It was critical to maintain a positive pressure inside the boxes to prevent any oxygen from entering through a crack in the seals. This was monitored by observing the gas bubble rate, ensuring the rate did not decrease as the pressure inside the gas cylinders decreased steadily over time. Attempts were made to daisy-chain the gas inlet and outlet lines between each box. However, the required pressure to achieve gas flow was too high and caused leaking to occur, so the decision was made to use one gas cylinder per box.

The *pH* of the C2 solution was measured periodically throughout the full-scale test. The solution was changed once due to a rise in the *pH* level of the solution. This likely occurred from the lack of mixing in the corrosion cell due to its large internal volume. This caused the P_{CO2} to decrease over time in portions of the C2 solution located farthest from the CO_2 source. This effect may not be observed in corrosion cells designed for CT specimens or surface crack tension (SCT) specimens as the volume of C2 solution contained within these cells is over one order of magnitude less than what was required for the boxes used in this work.

iii. *Anaerobic environment*

A critical pre-requisite of the NNpH environment is the anaerobic properties of the electrolyte. If oxygen is introduced into the system, the iron will oxidize, and the CO_2 corrosion mechanism will de-stabilize. Direct monitoring of the anaerobic environment can be achieved by observing the colour of the solution through the view port installed in each of the boxes. If the colour shifts from clear to orange, clearly the anaerobic environment is compromised. As the solution maintained a transparent colouring throughout the test, the boxes were successful in maintaining the anaerobic environment.

In addition, the CP level was monitored throughout the test. A value of -130 mV of cathodic polarization was applied to the exposed pipe surface. The measurements over the test duration are shown in **Figure 3.6**. The sacrificial anodes were replaced once when they had been nearly consumed. The anodes exhibited an aggressive dissolution rate as the ratio of the surface area of the cathode (exposed pipe surface) to the surface area of the anode was relatively high.

It was noted that the steel surface required ~ 15 days to fully polarize. This was likely due to the low current available from the impressed current system. The Model 363 Potentiostat-Galvanostat had a maximum DC current output of 1.0 A. This window of insufficient CP could be reduced by increasing the surface area of the anodes or using a system with higher current capabilities. There was potential for corrosion to occur within the window where the pipe surface was not fully protected by CP. During the time without full protection, the assumption of hydrogen-dominant continuous growth was no longer considered valid as there was a strong likelihood for crack tip

dissolution; thereby causing crack tip blunting. The error introduced by the potential crack tip blunting effect was difficult to quantify, however was still considered.

5.1.3 PRESSURE CONTROL SYSTEM

Discussion regarding the effectiveness of the pressure control system was provided in **Section 4.1**. There, two scenarios were identified that caused the instantaneous pressure to deviate from the target pressure. Additionally, improvements to the system to prevent those scenarios from occurring in future work were suggested. Overall, the ability of the pressure control system to maintain the target pressure was a success.

Over the course of the 91-day full-scale test a pressure reading was recorded each second, generating over 7 800 000 data points. To determine a more appropriate data collection interval, a five-hour section of Region II pressure fluctuations was plotted in **Figure 5.1** using various sampling intervals. Little error was introduced when the sampling interval was increased from 1 to 30 s. However, a slight error was introduced at a 60 s interval and accurate representation of the data became problematic at a 100 s interval, where the minimum and maximum pressures were rarely accurately represented. Therefore, it is recommended that future full-scale work studying crack growth under a constant loading rate uses a sampling interval where a datapoint is recorded every 30 s, with a maximum sampling interval of 60 s. Implementation of a 30 s sampling interval would reduce the amount of data collected by 97 % without introducing significant error bias.

Supervisory Control and Data Acquisition (SCADA) is a system used by pipeline operators to monitor and record the pressure fluctuations in the pipeline. For the purpose of making remaining life predictions based on pressure fluctuations, the history of the pressure variations within the pipeline segment must be captured accurately to include all pressurization and de-pressurization events that could contribute to crack growth [79]. According to a recent study, the recommended maximum SCADA data sampling interval for gas pipelines and oil pipelines is 2 h and 1 min, respectively [128]. While the former interval is large due to the compressibility of the transport media (and does not apply to this work as liquid media was used); the maximum recommended sampling interval for the latter was in excellent agreeance with the discussion above.
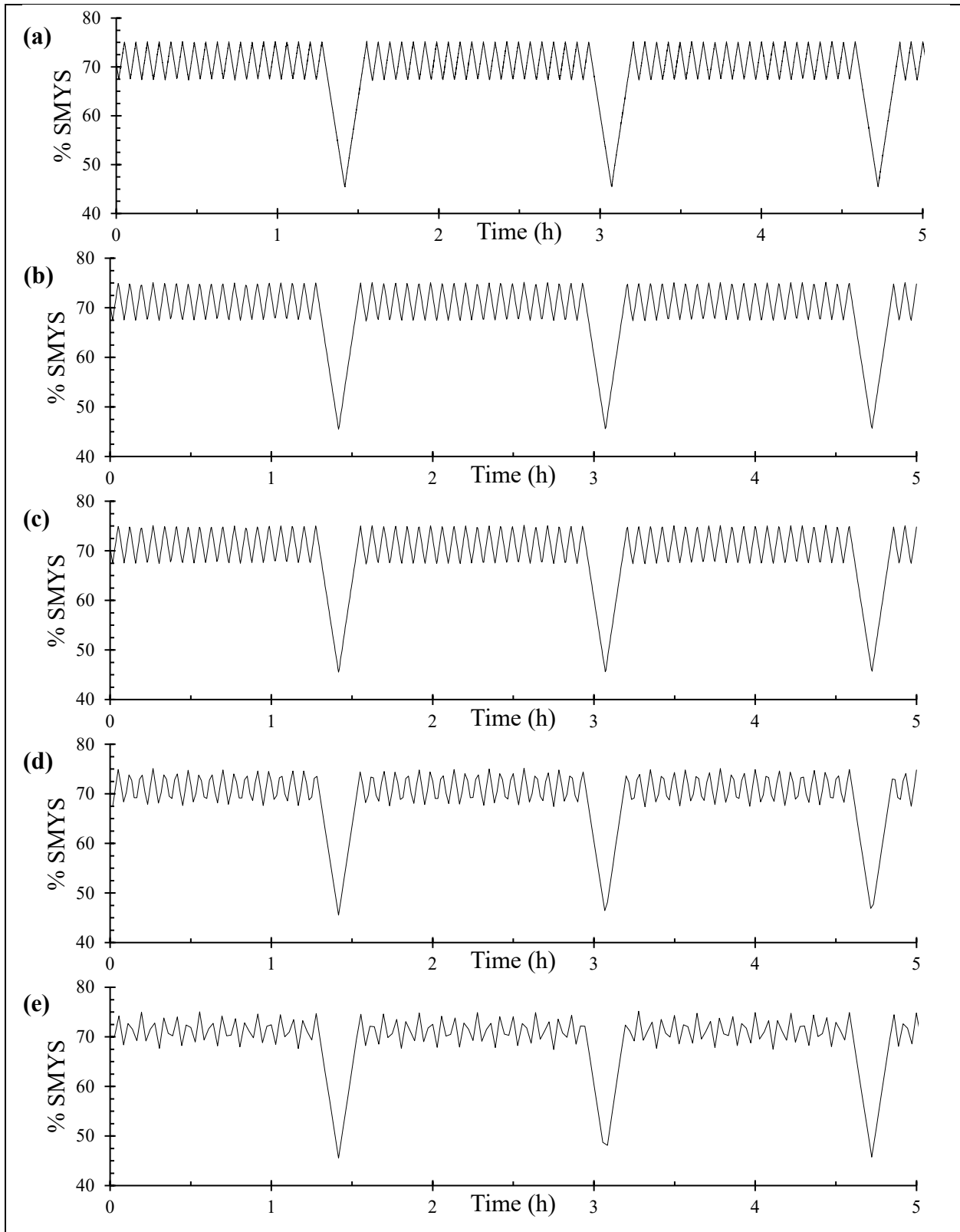
Figure 5.1   Five-hours of test data collected during Region II of the full-scale test plotted using a data sample interval of (a) 1 s, (b) 15 s, (c) 30 s, (d) 60 s and (e) 100 s.

5.1.4 MECHANICAL LOADING CONDITIONS

The mechanical loading conditions used to generate crack growth were produced by internal pressure fluctuations of the pipe segment. The pressure fluctuations chosen for the full-scale test were developed using the pre-test ECHO-3D inspection data. Safe implementation of the loading conditions created by the pressure fluctuations throughout the full-scale test was critical. This required careful consideration of the most severe flaw reported during the inspection, as rupture of the pipe was a major safety concern. The growth prediction was done under the assumption that the cracks were sharp stress concentrators and growth would begin when the test was underway. This was a necessary conservative assumption as immediate crack initiation may have occurred, thus the loading conditions produced by the pressure fluctuations were required to generate a safe levels of crack growth throughout the full duration of the test. The calculation was done using the combined factor equation, which was modeled based on experimental crack growth data from CT specimens under constant amplitude loading conditions. Full explanation of the calculation is given in **Section 3.4**.

As mentioned above, the initial crack dimensions were obtained from the ECHO-3D inspection. The manufacturer of the technology claimed the tool could detect cracks longer than 19 mm with depths of $0 - 6$ mm $\pm$ 10 % [27]. The accuracy of the tool was given little consideration during test design but was found to be a critical contributing factor to the limited success of the full-scale test. The most severe cracks reported in the pre-test inspection, alongside the acceptable error according to manufacturer specification, are shown in **Table 5.1**. Dimensions of the three deepest cracks found by destructive testing after test completion are shown in **Table 5.2**. The three deepest cracks found after testing all exhibited crack growth, so the initial crack depths are calculated to compare with the depths reported by ECHO-3D. The initial depths of the deepest cracks measured destructively are $30 - 40$ % shallower than what was predicted by ECHO-3D.

After test completion, growth was reported by ECHO-3D in a crack colony that was subjected to the NNpH environment. Two cracks with identical initial depths of 0.8 mm were reported with final depths of 1.99 and 1.55 mm (1.19 and 0.75 mm growth, respectively). Based on the crack growth predictions in **Table 3.6**, this level of crack growth during the test was unlikely for cracks with initial depths less than 1.0 mm. In fact, the largest amount of crack growth found with destructive testing was 0.14 mm, significantly less than the growth values reported by ECHO-3D.

Table 5.1　　Crack dimensions of the two most severe cracks reported by ECHO-3D during pre-test inspection.

Crack Length (mm)	Crack Depth (mm)	Depth range considering ± 10 % error (mm)
> 150	2.11	1.90 – 2.32
> 140	2.00	1.80 – 2.20
Unreported	1.71	1.54 – 1.88

Table 5.2　　Crack dimensions of the deepest cracks measured using destructive testing techniques after completion of the full-scale test.

Crack Length (mm)	Final Crack Depth (mm)	Crack Growth During Test (mm)	Initial Crack Depth (mm)
28.98	1.43	0.119	1.31
28.50	1.40	0.046	1.35
28.00	1.29	0.090	1.20

Therefore, considering the discussion above, it can be concluded that ECHO-3D inspection technology has a significantly higher margin of error than reported by the manufacturer. Caution should be taken when using the crack depth results from this inspection method for crack trending, or remaining life calculations as there appears to be an excessively significant amount of conservatism and inaccuracy with the inspection results.

An additional contributing factor to the limited success of the full-scale test was its test length. Initially, the proposed test duration was six months. That duration was deemed unacceptable by one of the financial sponsors, and a non-negotiable maximum test length of three months was required. As mentioned previously, the crack tips were assumed to be sharp and would experience Stage 2 continuous crack growth. The stress intensity level at the crack tip was designed to be high enough to maintain growth under that assumption. However, the crack dimensions used for these calculations were based on cracks 30 – 40 % deeper than what was present in the pipe segment. Additionally, the assumption of sharp crack tips was incorrect as crack tip blunting occurred due to exposure the elements for ~ 2.5 years from the time the pipe was excavated to when the full-scale test began. Therefore, the stress intensity factor experienced by the blunt crack tips was much lower than the values calculated for sharp crack tips and crack dimensions reported by ECHO-3D. This was likely the cause of unfavourable stress levels for continuous crack growth. Instead, the discontinuous crack growth was observed due to the lower stresses, whereby repeated crack dormancy and active growth occurred [96]. As discontinuous crack growth is a time dependent process, it is likely that a longer test duration may have produced more significant crack growth.

5.1.5 CRACK CHATACTERIZATION

The full-scale test consisted of four unique loading regimes. The purpose of multiple pressure fluctuation regions was to study the effect of various loading conditions, and to maximize the results obtained from one test. Separation of the loading regions can be achieved by generating a beach mark on the crack face by applying a high-frequency fatigue cycle for a short period of time. This method has been implemented successfully in many NNpHSCC laboratory studies using CT specimens [42, 86, 88] and SCT specimens [72, 73, 93].

As discussed in **Section 4.3.1**, it was not possible to separate the crack growth by region due to the lack of defining fracture surface characteristics. This was partially due to the small amount of growth produced throughout the test, as discussed in the sections above. Another possible cause was that full-scale testing was more difficult to control than small-scale testing; especially protecting the crack faces from oxidation throughout the end of test procedure (**Section 3.5**). Cracks were exposed to atmospheric conditions for up to 12 months after completion of the test prior to characterization. During this time, exposure to atmospheric humidity may have contributed to oxidation of the crack faces. Additionally, as it has been hypothesized that the cracks were experiencing a discontinuous growth mechanism, it was unclear when crack growth started and if the cracks experienced any periods of dormancy and re-initiation. Therefore, accurate estimation of blunt crack re-initiation and growth could not be made with any level of confidence. To facilitate basic discussion in the following sections, it was assumed that crack re-initiation occurred at the start of the test and was evenly distributed over the four loading regions.

5.2 STAGE 1 CRACK INITIATION IN DENTS

A dent is defined as a depression caused by mechanical damage that produces a visible disturbance in the curvature of the wall of the pipe without reducing the wall thickness. It is not of great interest to study the effects of environmentally assisted cracking and pressure cycling on dents that are considered a defect as they require immediate repair in the field. However, a deeper understanding of the threshold for crack initiation in dents considered acceptable to remain in service would be valuable to the field. Furthermore, at times, the pipeline operator may choose to repair dents using criteria more conservative than that defined in standards such as CSA Z662. For example, dents are known to obstruct ILI tools if they cause the pipe to deviate significantly from round. As ILI tools are a critical component of pipeline integrity programs, dents causing blockage must be repaired. A dent is considered an imperfection of sufficient magnitude to warrant rejection from continued service (i.e. a defect) if certain criteria are met including [8]:

i.   dents interacting with a weld that exceed 2 % of the OD in pipe larger than 323.9 mm OD;

ii. dents located on the pipe body that exceed a depth of 6 % of the OD in pipe larger than 101.6 mm OD.

iii. dents that contain corrosion causing greater than 40 % nominal wall loss;

iv. and dents that contain stress concentrators (gouges, grooves, arc burns, cracks, etc.).

The initial depths of the dents in this study were chosen such that they would be considered a significant threat to the integrity of the pipe segment but would not meet any of the above criteria to be deemed unfit for service. Four dents were machined in areas of the pipe body with clean metal (no external corrosion) and where cracking was not present, to satisfy requirements $i - iv$ above. Dents A, B, C and D were machined into the pipe segment with an initial depth of $1.7 - 2.0$ % of the pipe OD to study crack initiation under the environmental and loading conditions of the full-scale test. Three of the dents were submerged in the NNpH environment. Dents A and C were completely exposed to the electrolyte, simulating a coating holiday; while Dent B was covered by a simulated coating disbondment. Dent D was left exposed to air to act as a control and to facilitate visual examination throughout the test.

After the test was complete, MPI was conducted on the pipe body and no cracking was found near the dents. As MPI cannot reliably detect cracks shorter than $2 - 3$ mm in length [22], cracks with

dimensions smaller than the detection threshold of MPI may have formed. Further advanced techniques, such as cross-sectional analysis, were not used to locate microcracks as it was not related to the primary research objective of this work. The following will discuss the lack of crack initiation in the dents.[4]

i. The primary consideration for the absence of crack initiation was that the loading conditions were not aggressive enough. As previously stated, the pressure fluctuations were designed to promote crack growth in pre-existing cracks. Therefore, the loading conditions were not designed to generate crack initiation at the dents over the course of the test.

ii. The pipe was sandblasted twice prior to the full-scale test; once during the field assessment prior to its removal from service in February 2015 and a second time during pre-test inspection in March 2018. Sandblasting creates a compressive residual stress on the pipe surface, improving resistance to pitting and SCC initiation [53, 54].

iii. CP was applied Dents A and C and the electric path was not blocked by any simulated coating disbondments. Effective CP reaching the metal surface inhibits corrosion and the formation of micro-pits. Therefore, NNpHSCC initiation was unfavourable for these dents.

iv. Crack initiation in Dent D was not expected as it was exposed to atmospheric conditions and crack initiation was governed by pure mechanical fatigue. The loading conditions of the test were not favourable for fatigue driven crack initiation.

v. Dent B was most likely to exhibit crack initiation as it was underneath a simulated coating disbondment in the NNpH environment and shielded from CP; increasing the probability of local micro-pit formation. However, micro-pits have been shown to form in areas of high tensile residual stress and the pipe surface was likely in a state of compressive residual stress due to sandblasting [53, 54]. With that in mind, it is reasonable to conclude that the compressive residual stresses present at the dents may have lowered the potential for micro-pit initiation, and by extension Stage 1 crack initiation. Additionally, it has been shown that longer test times allow for additional cracks to nucleate and grow via Stage 1 growth [65]. Therefore, the test duration may have been too short for the processes of micro-pit formation and subsequent dissolution driven crack growth to occur.

---

[4] It should be noted that this discussion was based on the assumption that microcracks below the detection limit of MPI did not form.

106

5.3 STAGE 2 CRACK RE-INITIATION AND GROWTH

The environmental and mechanical conditions required for NNpHSCC to occur in the field have been thoroughly discussed in **Chapter 2**. There are three common methodologies used to study the effects of NNpHSCC in the literature [6, 7, 77]:

i.   *Fatigue-only case*

Experimental studies where cracks were exposed to atmospheric conditions (i.e. air) have been used to simulate mechanically driven fatigue crack growth. Extensive studies [33, 97, 114, 117] using this technique have led to many significant findings, such as the Paris Law, which introduced a new fracture mechanics paradigm in research. This experimental method has also been used to successfully isolate the effect of certain variables on the crack growth rate, such as the effect of the number of minor cycles on underload-type pressure fluctuations [42]. Cracks exposed to air can be compared to cracks in pipeline steel that have been re-coated after integrity assessments. However, models developed using these results have limited application to SCC management programs as they do not account for the effects of corrosion or environmentally assisted cracking (EAC) on mechanical fatigue driven crack growth.

ii.   *Dissolution and hydrogen case*

Full exposure of cracks at open circuit potential (OCP) to a simulated NNpH environment is used to study NNpHSCC, while considering the effects of corrosion and EAC on crack growth that are overlooked in the point above. To study crack growth in a NNpH environment without introducing simulated coating disbondments, specimens fully exposed to a NNpH solution at OCP conditions can be used. This is an acceptable substitute as the cathodically shielded environment underneath a coating disbondment is similar to the environment produced by OCP conditions.

Figure 2.18 shows the competing mechanisms responsible for NNpHSCC, as discussed in **Section 2.6.3**. The life cycle of NNpHSCC is complex as two competing crack growth mechanisms are present: dissolution driven crack growth and hydrogen-assisted crack growth. Understanding the effect and magnitude of these competing mechanisms on NNpHSCC is critical for development of crack growth prediction models. It is hypothesized that Stage 2

crack growth in the field follows a discontinuous growth mechanism when the stress intensity level is above a threshold for growth but has not reached a secondary threshold intensity required for continuous growth [6, 116]. Consequently, total crack growth over time in the field may be substantially lower than the periods of active crack growth when periods of dormancy are removed from consideration.

The advantage to this methodology is that the environmental conditions reflect the overall NNpH conditions seen in the field. However, for the purposes of developing crack growth prediction models, it is desirable to isolate active Stage 2 crack growth caused by hydrogen effects from the periods of dormancy.

iii.   *Hydrogen-only case*

Development of Stage 2 NNpHSCC growth models requires isolation of the hydrogen-facilitated fatigue crack growth. A common practice used in the literature is to apply a coating to the portion of a specimen where the crack is located, and the remainder of the sample is left exposed to the simulated NNpH environment at OCP. This prevents the electrolyte from reaching the crack, mitigating the effects of dissolution crack growth; while allowing the production of hydrogen at the surface of the bulk material and diffusion throughout the specimen. Typically, a 275 h period of incubation corresponding to the generation of hydrogen at the sample surface and the time required to achieve a state of hydrogen equilibrium throughout the specimen is required [86]. This methodology allows the effect of steady-state hydrogen facilitated crack growth to be studied.

The cracks were fully exposed to the electrolyte, with applied CP, throughout the full-scale test, thereby creating the hydrogen only condition. The decision to not apply a coating was made as the results of the test would have been subjective to the specific coating used. Therefore, CP was implemented to prevent corrosion and isolate the effects of hydrogen-facilitated fatigue crack growth. The effect of CP on crack growth required consideration as deviation from OCP conditions could affect the ability to apply the results of the full-scale test to experimental hydrogen only crack growth results. Findings have shown that steel is more susceptible to failure at slightly cathodic potentials than when under OCP conditions, likely caused by the higher concentrations of hydrogen present in the bulk solution due to presence of CP [68].

A total of 243 cracks were analyzed and their depths are summarized in **Figure 5.2**. Unfortunately, due to the limited results of the test, the effect of Type I and Type II fluctuations on full-scale crack growth could not be determined. Assuming crack re-initiation occurred at the start of the test and the crack growth was uniform throughout the full-scale test, the crack growth rate was $1.1 - 1.8 \times 10^{-8}$ mm/s and 0.6×10^{-8} mm/s for cracks exposed to the NNpH environment and atmospheric conditions, respectively.
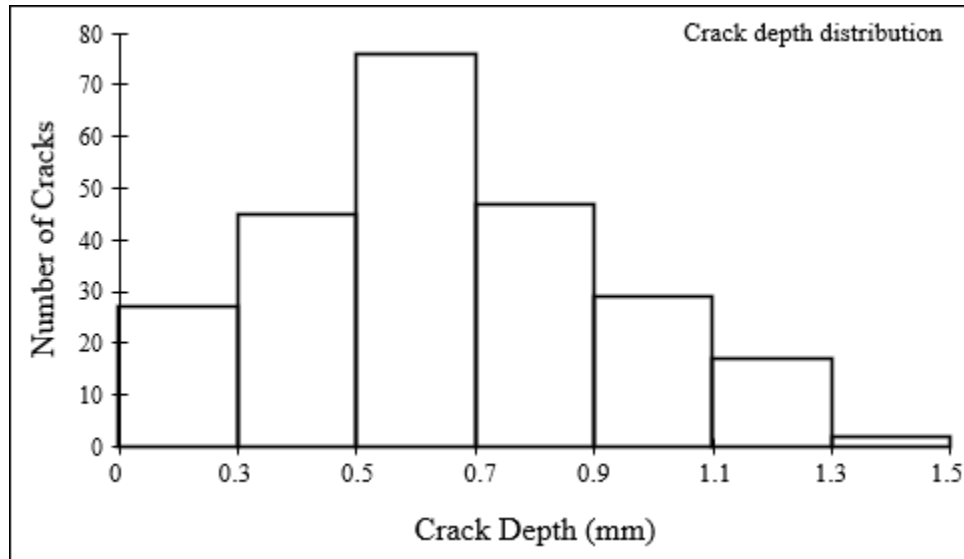

Figure 5.2   Analyzed total crack depth distribution measured using destructive testing techniques. The pipe segment was in service for 46 years prior to being cut-out and tested for 91 days. Crack depths were measured after testing was complete.

To determine a threshold stress intensity factor (K_{th}) for crack initiation in air and NNpH environments, the maximum stress intensity factor (K_{max}) of the cracks shown in **Figure 4.12** was calculated using the Newman and Raju stress intensity equation for a semielliptical surface flaw in a flat plate for $a \leq c$ [114], with a maximum stress value of 75 % SMYS ($\sigma_{max} = 310$ MPa). The K_{max} values were plotted as a function of crack length and crack depth in **Figure 5.3a** and **Figure 5.3b**, respectively. K_{th} in air and in the NNpH environment was determined to be ~ 25 and ~ 18 MPa√m, respectively.
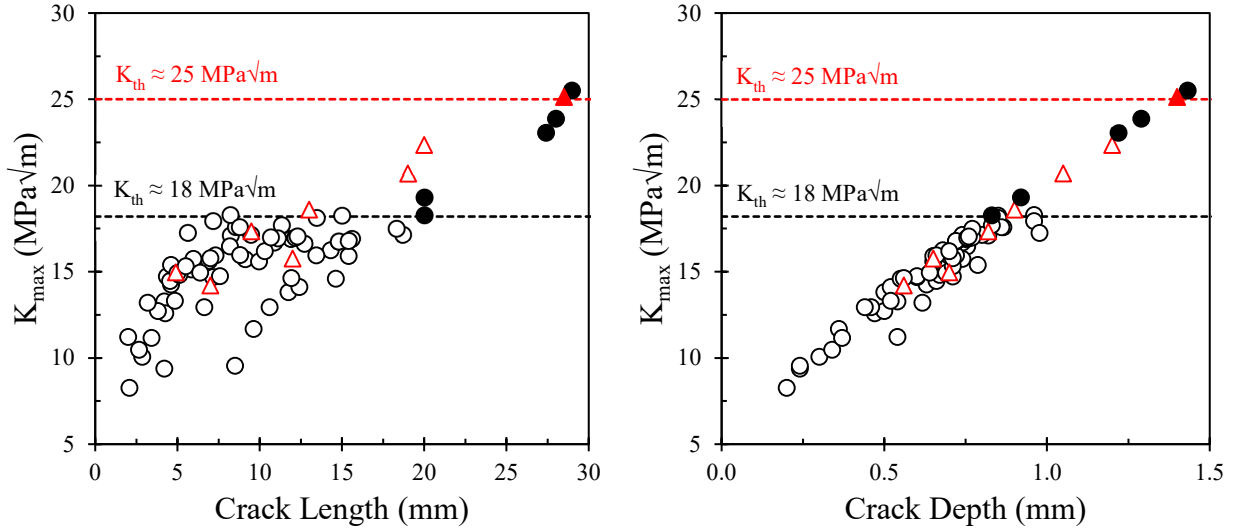
Figure 5.3 K_{max} in the depth direction versus (left) the crack length and (right) the crack depth for the cracks analyzed after completion of the full-scale test (σ_{max} = 310 MPa). K_{th} for crack re-initiation in air and in C2 solution was found to be ~ 25 and ~ 18 MPa√m, respectively.

It should be noted that the K_{th} values are only valid for the loading conditions of the full-scale test. It has been shown that crack initiation and growth is tied to the combined factor (CF) [85, 86], which depends on K_{max}, the stress intensity factor range (ΔK) and the frequency of the pressure fluctuations. As the K_{th} values discussed above only represent one of the three variables, the K_{th} determined is only valid for the loading conditions of the full-scale test. For example, non-propagating high R-ratio minor cycles will contribute significantly less to crack growth than low R-ratio underloads with the same $K_{max.}$

A CF threshold value for the full-scale crack growth could be determined if the moment of crack initiation was known. However, as that moment was uncertain, discussion regarding a CF threshold would have severe limitations. Additionally, the CF model can only account for constant amplitude loading conditions and its application regarding load interactions (variable amplitude conditions) is limited. Considering the above, the accuracy of the CF relating to the pressure fluctuations of the full-scale test would be ambiguous. Therefore, discussion regarding a threshold CF value will not be given.

110

CHAPTER 6: CONCLUSIONS AND RECOMMENDATIONS

The objective of this investigation was to determine the effects of loading conditions on Stage 2 near-neutral *pH* stress corrosion cracking (NNpHSCC) re-initiation and growth. The specimen used was a 4.77 m long section of NPS 18, X-60 steel line pipe that had developed SCC colonies over 46 years of gas transmission service. These SCC colonies on the full-scale specimen were immersed in a simulated NNpH environment and the remainder were left exposed to the atmospheric environment (air). To simulate the NNpH environment, a novel corrosion cell was developed to encapsulate portions of the pipe. A custom impressed current cathodic protection (CP) system was designed and -130 mV of cathodic polarization was applied to mitigate the effects of corrosion and facilitate the study of hydrogen-only fatigue crack growth. The loading conditions studied were underload with minor cycle (Type I) fluctuations and constant amplitude (Type II) fluctuations, designed to simulate internal gas and liquid media, respectively. Loading conditions were optimized to promote safe crack growth without causing rupture by performing remaining life calculations on the pre-test crack dimensions. Additionally, dents were machined in the full-scale specimen to opportunistically study crack initiation in dents subjected to NNpH conditions.

From the results of this study, the threshold stress intensity factor (K_{th}) for crack initiation under the loading conditions of the full-scale test was determined for cracks exposed to the NNpH environment and to air. However, it was not possible to conduct a study comparing the crack growth of the full-scale test with results from the literature using compact toughness (CT) specimens or surface crack tension (SCT) specimens due to the inability to separate the measured crack growth into the contribution made by each loading regime.

During the design of the pressure fluctuations, it was assumed that the cracks were sharp, and that growth would occur immediately once the test was underway. This assumption proved to be incorrect as it was determined that crack blunting occurred after the pipe segment was cut-out, before full-scale testing. Additionally, there was significant uncertainty regarding the moment of crack re-initiation and whether the growth was intermittent or continuous. This uncertainty was identified as the primary factor contributing to the limited results of the full-scale test. Secondary causes can be attributed to insufficient test time due to project timeline constraints enforced by a financial sponsor, loading conditions unfavourable for crack growth due to incorrect initial crack

sizing data and the invalid assumption that crack tips were sharp and growth would occur continuously throughout the test.

6.1 CRACK ANALYSIS

After completion of the 91-day full-scale test, a total of 243 cracks were analyzed using destructive techniques. Crack growth attributed to the full-scale test was found in five cracks exposed to the NNpH environment and one crack exposed to air, or 2.5 % of the total cracks analyzed.

1. The average crack growth rate (normalized over the full duration of the test) was 2 – 3 times larger in the NNpH environment than the average crack growth rate in air under the same conditions. However, the accuracy of this acceleration factor is undetermined as the moment of individual crack re-initiation is uncertain.

2. The threshold stress intensity factor (K_{th}) required for crack re-initiation in the NNpH environment was found to be lower than the K_{th} required for crack re-initiation in air due to the effects of environmentally assisted cracking. As the moment of crack re-initiation was uncertain, discussion relating crack growth to the combined factor could not be given and discussion regarding K_{th} was only applicable to the loading conditions of the full-scale test.

3. The dents manufactured in the pipe completely rebounded during testing and after de-pressurization, they did not return to their original depths. Magnetic particle inspection (MPI) was conducted in the areas of the dents and crack initiation was not observed. However, the absence of cracks too small to be resolved by MPI was not confirmed.

6.2 RECOMMENDATIONS FOR FUTURE WORK

While the full-scale test did not produce the desired results, the novel test design was effective. Suggested improvements to the experimental procedure for future work are as follows:

1. During the test design phase, accurate sizing of the pre-existing cracks is critical. Use of ECHO-3D inspection technology is not recommended as the inspection results contained excessive conservatism resulting in reported crack depths 30 – 40 % deeper than what was found using destructive testing methods.

2. Appropriate pump selection is critical as the pump is responsible for generating the loading conditions of the test. It is recommended that the air flow rate required to create the desired pressure gain is approximately 50 % of the allowable maximum flow to prevent the pump from stalling at low flow rates.

3. A control valve with an appropriate C_v should be used in place of a solenoid valve to control the de-pressurization portions of the loading scheme as the latter did not perform optimally.

4. Accurate collection of the pressure fluctuation data is critical. A sensitivity analysis was performed on the data sampling interval of the pressure fluctuations. It was determined that increasing the data sampling interval to 30 seconds would significantly reduce the volume of data collected without introducing additional error.

5. The conditions at the crack tip are more difficult to control for full-scale testing than for experimental work using small-scale CT or SCT specimens. The current work attempted to study the crack growth rate of multiple waveforms in one test. It is recommended that future work limits the scope of each test to one wave form, until successful methods are developed to reliably separate the growth zones of multiple fluctuations. Adaptation of this approach would reduce the uncertainty of the contribution of multiple waveforms.

BIBLIOGRAPHY

[1]   J. T. Justice and J. D. Mackenzie, "Progress in the Control of Stress Corrosion in a 914 MM O.D. Gas Transmission Pipeline," *7th Biennial Joint Meeting on Line Pipe Research,* 1988.

[2]   B. Delanty and J. O'Beirne, "Major Field Study Compares Pipeline SCC with Coatings," *J. Oil & Gas,* vol. 90, no. 24, pp. 39-44, 1992.

[3]   CEPA Recommended Practices, "Managing Near-neutral pH Stress Corrosion Cracking, 3rd edition," 2015.

[4]   R. R. Fessier and K. Krist, "Research challenges regarding stress-corrosion cracking of pipelines," in *Corrosion 2000*, NACE International, 2000, Paper no. 00370.

[5]   CEPA Recommended Practices, "Stress Corrosion Cracking, 2nd Edition," 2007.

[6]   W. Chen, "Chapter 30: Modeling and prediction of stress corrosion cracking of pipeline steels," in *Trends in Oil and Gas Corrosion Research and Technologies: Production and Transmission*, 2017, pp. 707-748.

[7]   W. Chen, J. Zhao, J. Been, K. Chevil, G. Van Boven, and S. Keane, "Update of Understanding of Near-Neutral pH SCC Crack Growth Mechanisms and Development of Pipe-Online Software for Pipeline Integrity Management," in *11th IPC*, Calgary AB, 2016.

[8]   CSA Standard Z662-19, "Oil and Gas Pipeline Systems," June 2019.

[9]   U.S. Department of Energy, "International Energy Outlook 2019," Washington D.C. September 24, 2019, Available: https://www.eia.gov/outlooks/ieo/.

[10]   Statistics Canada. (2019, Oct 19). *Exports and imports of goods and services, quarterly, Canada, (NAPCS 2017) (x 1,000,000). Table 12-10-0134-01*.

[11]   Statistics Canada. (2019, Oct 19). *Gross domestic product (GDP) at basic prices, by industry, annual average (x 1,000,000). Table 36-10-0434-03*.

[12]   Alberta Energy Regulator. (2019, Oct 19). *Pipeline Performance Report*.

[13]   Canada Energy Regulator. (2019, Oct 19). *2018 Marketable Natural Gas Production in Canada*. Available: www.cer-rec.gc.ca/nrg/sttstc/ntrlgs/stt/mrktblntrlgsprdctn-eng.html

[14]   Canada Energy Regulator. (2019, Oct 19). *2018 Estimated Production of Canadian Crude Oil and Equivalent*. Available: www.cer-rec.gc.ca/nrg/sttstc/crdlndptrlmprdct/stt/stmtdprdctn-eng.html

[15]   Canada Energy Regulator. (2019, Oct 19). *2016 Estimated Production of Canadian Crude Oil and Equivalent*. Available: www.cer-rec.gc.ca/nrg/sttstc/crdlndptrlmprdct/stt/archive/stmtdprdctnrchv-eng.html

[16]   Canada Energy Regulator. (2019, Oct 19). *2016 Marketable Natural Gas Production in Canada*. Available: www.cer-rec.gc.ca/nrg/sttstc/ntrlgs/stt/archive/mrktblntrlgsprdctnrchv-eng.html

[17]   Government of Canada. (2018). *NEB Event Reporting Guidelines 2018*.

[18]   National Energy Board. (2014, March 17). *Ruptures on NEB-regulated pipelines*. Available: https://www.cer-rec.gc.ca/sftnvrnmnt/sft/pplnrptr/index-eng.html

[19]   W. Chen and R. Sutherby, "Laboratory simulation of hydrostatic test in near-neutral PH soil environments," in *6th IPC*, Calgary AB, 2007, vol. 2, pp. 711-724.

[20]   F. King, "Development of guidelines for identification of scc sites and estimation of re-inspection intervals for scc direct assessment," Integrity Corrosion Consulting Ltd. 2010.

[21]   L. Cartz, "Chapter 5: Magnetic Particle Inspection," in *Nondestructive Testing*: ASM International, 1995, pp. 141-172.

[22]   K. G. Bøving, "Chapter 17 - Magnetic particle examination," in *NDE Handbook*, 1989, pp. 171-188.

[23]   NACE Standard No. 2/SSPC-SP 10, "Joint Surface Preparation: Near-White Metal Blast Cleaning," *Item No. 21066,* 2000.

[24]   L. Cartz, "Chapter 2: Radiography," in *Nondestructive Testing*: ASM International, 1995, pp. 15-80.

[25]   L. Cartz, "Chapter 6: Eddy Current," in *Nondestructive Testing*: ASM International, 1995, pp. 173-188.

[26]   M. Trimm, "An overview of nondestructive evaluation methods," *J. Fail. Anal. Prev.,* vol. 3, no. 3, pp. 17-31, 2003.

[27]   Authors Unknown. (2019, Nov 9). *About ECHO-3D, Principles of Operation*. Available: https://www.echo-3d.com/

[28]   L. Cartz, "Chapter 3: Ultrasonic Testing," in *Nondestructive Testing*: ASM International, 1995, pp. 81-125.

[29]   F. C. Campbell, "Optical Emission Spectroscopy," in *Inspection of Metals - Understanding the Basics, Chapter 7*: ASM International, 2013.

[30]   Authors Unknown. (2019, Nov 11). *Laser Induced Breakdown Spectroscopy*. Available: https://www.sciaps.com/libs-handheld-laser-analyzers/carbon-testing/

[31]   R. O. Ritchie, "Mechanisms of fatigue-crack propagation in ductile and brittle solids," *Int. J. Fract.,* vol. 100, no. 1, pp. 55-83, 1999.

[32]   T. L. Anderson, "Chapter 11: Envronmentally Assisted Cracking in Metals," in *Fracture Mechanics: Fundamentals and Applications, 4th Edition*, 2017, pp. 537-580.

[33]   P. C. Paris and F. Erdogan, "A critical analysis of crack propagation laws," *J. Basic Eng.,* vol. 85, no. 4, pp. 528-534, 1963.

[34]   K. Sadananda, A. K. Vasudevan, R. L. Holtz, and E. U. Lee, "Analysis of overload effects and related phenomena," *Int. J. Fatigue,* vol. 21, no. Supplement 1, pp. S233-S246, 1999.

[35]   A. Bacila, X. Decoopman, G. Mesmacque, M. Voda, and V. A. Serban, "Study of underload effects on the delay induced by an overload in fatigue crack propagation," *Int. J. Fatigue,* vol. 29, no. 9, pp. 1781-1787, 2007.

[36]   A. G. Mazel, "On stress corrosion cracking of gas pipelines, Reliability and safety of gas pipelines subject to stress corrosion cracking," STP 2-4, Moscow, RAO Gazprom, pp. 11-22, 1993.

[37]   R. Wang, "Effects of hydrogen on the fracture toughness of a X70 pipeline steel," *Corro. Sci.,* vol. 51, no. 12, pp. 2803-2810, 2009.

[38]   R. W. Stahle, J. Hochmann, R. D. McCright, J. E. Slater, and S. R. Shatynski, "Stress corrosion cracking and hydrogen embrittlement of iron base alloys," *J. Electrochem. Soci.,* vol. 126, no. 5: 215C, 1979.

[39]   R. P. Gangloff, "Hydrogen-assisted Cracking," in *Comprehensive Structural Integrity*, vol. 6, 2003, pp. 31-101.

[40]   Y. Katz, N. Tymiak, and W. W. Gerberich, "Nanomechanical probes as new approaches to hydrogen/deformation interaction studies," *Eng. Fract. Mech.,* vol. 68, no. 6, pp. 619-646, 2001.

[41]   H. K. Birnbaum and P. Sofronis, "Hydrogen-enhanced localized plasticity-a mechanism for hydrogen-related fracture," *Mater. Sci. Eng. A,* vol. 176, no. 1-2, pp. 191-202, 1994.

[42]   M. Yu, "Crack Growth Behavior of Pipeline Steels under Variable Pressure Fluctuations in a Near-Neutral pH Environment," 2015.

[43]   A. R. Troiano, "The role of hydrogen and other interstitials in the mechanical behavior of metals," *Metallography, Microstructure, and Analysis,* vol. 5, no. 6, pp. 557-569, 2016.

[44]   J. Zhao *et al.*, "Crack Growth Modeling and Life Prediction of Pipeline Steels Exposed to Near-Neutral pH Environments: Dissolution Crack Growth and Occurrence of Crack Dormancy in Stage I," *Metall. Mater. Trans. A,* vol. 48, no. 4, pp. 1629-1640, 2017.

[45]   J. Zhao *et al.*, "Crack Growth Modeling and Life Prediction of Pipeline Steels Exposed to Near-Neutral pH Environments: Stage II Crack Growth and Overall Life Prediction," *Metall. Mater. Trans. A,* vol. 48, no. 4, pp. 1641-1652, 2017.

[46]   J. A. Beavers, J. T. Johnson, and R. L. Sutherby, "Materials factors influencing the initiation of near-neutral pH SCC on underground pipelines," in *3rd IPC*, Calgary AB, 2000, vol. 2, pp. 979-988.

[47]   R. N. Parkins, "A review of stress corrosion cracking of high pressure gas pipelines," in *Corrosion 2000*, NACE International, 2000, paper no. 00363.

[48]   J. A. Beavers and B. A. Harle, "Mechanisms of high-pH and near-neutral-pH SCC of underground pipelines," *J. Offshore Mech. Arct.,* vol. 123, no. 3, pp. 147-151, 2001.

[49]   J. F. Kiefner and M. J. Rosenfeld, "The role of pipeline age in pipeline safety," INGAA Foundation Final Report No 2012.04, 2012.

[50]   J. M. Leeds and S. S. Leeds, "Coating properties and test procedures," *Pipeline & Gas J.,* vol. 273, no. 3, 2010.

[51]   D. M. Berger, "Electrochemical and galvanic corrosion of coated steel surfaces," *J. Chem. Eng.,* vol. 89, no. 13, pp. 109-112, 1982.

[52]   J. A. Beavers and N. Thompson, "External corrosion of oil and natural gas pipelines," *ASM Handbook,* vol. 13C, no. 05145, 2006.

[53]   G. Van Boven, W. Chen, and R. Rogge, "The role of residual stress in neutral pH stress corrosion cracking of pipeline steels – Part I: Pitting and cracking occurrence," *Acta Mater.,* vol. 55, no. 1, pp. 29-42, 2007.

[54]   W. Chen, G. Van Boven, and R. Rogge, "The role of residual stress in neutral pH stress corrosion cracking of pipeline steels – Part II: Crack dormancy," *Acta Mater.,* vol. 55, no. 1, pp. 43-53, 2007.

[55]   J. A. Beavers, "2013 Frank Newman speller award lecture: Integrity management of natural gas and petroleum pipelines subject to stress corrosion cracking," *Corrosion,* vol. 70, no. 1, pp. 3-18, 2014.

[56]   Z. Qin *et al.*, "Localized Dissolution of Millscale-Covered Pipeline Steel Surfaces," *Corrosion,* vol. 60, no. 10, pp. 906-914, 2004.

[57]   Authors Unknown, "Final Staff Report on Investigation of Tennessee Gas Transmission Company Pipeline No. 100-1 Failure near Natchitoches, Louisiana, March 4, 1965," Federal Power Commission, Bureau of Natural Gas, Washington, D.C. 1965.

[58]   J. A. Beavers and R. G. Worthingham, "The influence of soil chemistry on scc of underground pipelines," in *4th IPC*, Calgary, AB, 2002, pp. 1671-1678.

[59]   H. Niazi, K. Korol, H. Zhang, and W. Chen, "High pH crack growth sensitivity to underload-type of pressure fluctuations," in *12th IPC*, Calgary AB, 2018.

[60]   N. Leis and R. N. Parkins, "Mechanics and material aspects in predicting serviceability limited by stress-corrosion cracking," *Fat. Fract. Eng. Mater. Struct.,* vol. 21, no. 5, pp. 583-601, 1998.

[61]   P. L. Andresen and F. Peter Ford, "Life prediction by mechanistic modeling and system monitoring of environmental cracking of iron and nickel alloys in aqueous systems," *Mater. Sci. Eng. A,* vol. 103, no. 1, pp. 167-184, 1988.

[62]   P. L. Andresen and F. P. Ford, "Fundamental modeling of environmental cracking for improved design and lifetime evaluation in BWRs," *Int. J. Pres. Ves. Pip.,* vol. 59, no. 1, pp. 61-70, 1994.

[63]   R.N. Parkins, "The controlling parameters in stress corrosion cracking," *5th Symp. Line Pipe Research,* no. L30174, 1974.

[64]   R.R. Fessler, "Stress corrosion cracking temperature effects," *6th Symp. Line Pipe Research,* 1979.

[65]   R. N. Parkins, "Factors influencing stress corrosion crack growth kinetics," *Corrosion,* vol. 43, no. 3, pp. 130-139, 1987.

[66]   R. N. Parkins, "Strain rate effects in stress corrosion cracking," *Corrosion,* vol. 46, no. 3, pp. 178-189, 1990.

[67]   R. N. Parkins, "The application of stress corrosion crack growth kinetics to predicting lifetimes of structures," *Corro. Sci.,* vol. 29, no. 8, pp. 1019-1038, 1989.

[68]   W. Chen, F. King, T. R. Jack, and M. J. Wilmott, "Environmental aspects of near-neutral ph stress corrosion cracking of pipeline steel," *Metall. Mater. Trans. A,* vol. 33, no. 5, pp. 1429-1436, 2002.

[69]   S. Nesic, "Carbon Dioxide Corrosion of Mild Steel," *Uhlig's Corrosion Handbook, Third Edition,* 2011.

[70]   S. L. Asher, B. Leis, J. Colwell, and P. M. Singh, "Investigating the mechanism of transgranular stress corrosion cracking in near-neutral ph environments on buried fuel transmission pipelines," *Corrosion,* vol. 63, no. 10, pp. 932-939, 2007.

[71]   K. Chevil, "Investigation of Corrosion and Crack Morphology Behavior under Disbonded Coatings on Pipelines," MSc, Department of Chemical and Materials Engineering, University of Alberta, 2015.

[72]   D. Engel, "Investigation of Surface Crack Growth Behaviour Under Variable Pressure Fluctuations in Near-Neutral PH Environments," MSc, Department of Chemical and Materials Engineering, University of Alberta, pp. 115-121, 2017.

[73]   A. Egbewande *et al.*, "Transgranular crack growth in the pipeline steels exposed to near-neutral pH soil aqueous solutions: Discontinuous crack growth mechanism," *Corrosion,* vol. 83, pp. 343-354, 2014.

[74]   R. N. Parkins, W. K. Blanchard Jr, and B. S. Delanty, "Transgranular stress corrosion cracking of high-pressure pipelines in contact with solutions of near neutral pH," *Corrosion,* vol. 50, no. 5, pp. 394-408, 1994.

[75]   W. Chen, R. L. Eadie, and R. L. Sutherby, "Environmental effects on near-neutral pH stress corrosion cracking in pipelines," in *Environment-Induced Cracking of Materials*: Elsevier, 2008, pp. 211-220.

[76]   R. P. Gangloff, "Corrosion fatigue crack propagation in metals," *NASA-CR-4301,* 1990.

[77]   M. Yu *et al.*, "Corrosion fatigue crack growth behavior of pipeline steel under underload-type variable amplitude loading schemes," *Acta Mater.,* vol. 96, pp. 159-169, 2015.

[78]   J. Zhao, W. Chen, G. V. Boven, S. Keane, and J. Been, "Development and validation of load-interaction based models for crack growth prediction," in *10th IPC*, Calgary, AB, 2014.

[79]   J. Zhao *et al.*, "Statistical analysis on underload-type pipeline spectra," *J. Pipeline Syst. Eng.,* vol. 7, no. 4, 2016.

[80]   S. J. Haider, S. Textor, A. Sutton, and Y. Hubert, "Managing a new pressure cycling reality in liquid pipelines," in *10th IPC*, Calgary AB, 2014.

[81]   J. A. Beavers, W. E. Berry, and R. N. Parkins, "Standard test procedure for stress corrosion cracking threshold stress determination," *Mater. Perform.,* vol. 25, no. 6, p. 9, 1986.

[82]   M. Elboujdaini, Y. Z. Wang, R. W. Revie, R. N. Parkins, and M. T. Shehata, "Stress corrosion crack initiation processes: Pitting and microcrack coalescence," in *Corrosion 2000*, NACE International, 2000, Paper no. 00379.

[83]   R. N. Parkins and J. A. Beavers, "Some effects of strain rate on the transgranular stress corrosion cracking of ferritic steels in dilute near-neutral-pH solutions," *Corrosion,* vol. 59, no. 3, pp. 258-273, 2003.

[84]   T. M. Ahmed, S. B. Sutherby, and A. Plumtree, "Cyclic Crack Growth rates of X-60 Pipeline Steel in a Neutral Dilute Solution," *Corrosion,* vol. 53, no. 7, pp. 581-590, 1997.

[85]   W. Chen and R. L. Sutherby, "Crack growth behavior of pipeline steel in near-neutral pH soil environments," *Metall. Mater. Trans. A,* vol. 38, no. 6, pp. 1260-1268, 2007.

[86]   W. Chen, R. Kania, R. Worthingham, and G. V. Boven, "Transgranular crack growth in the pipeline steels exposed to near-neutral pH soil aqueous solutions: The role of hydrogen," *Acta Mater.,* vol. 57, no. 20, pp. 6200-6214, 2009.

[87]   B. Y. Fang, R. L. Eadie, W. X. Chen, and M. Elboujdaini, "Pit to crack transition in X-52 pipeline steel in near neutral pH environment: Part 1 - Formation of blunt cracks from pits under cyclic loading," *Corros. Eng. Sci. Technol.,* vol. 45, no. 4, pp. 302-312, 2010.

[88]   O. Tehinse, W. Chen, K. Chevil, E. Gamboa, and L. Lamborn, "Influence of mean load pressure fluctuations on crack growth behavior in steel pipelines," in *12th IPC*, Calgary AB, 2018.

[89]   M. Yu, W. Chen, K. Chevil, G. Van Boven, and J. Been, "Retarding crack growth by static pressure hold for pipeline steel exposed to a near-neutral pH environment," in *11th IPC*, Calgary AB, 2016.

[90]   M. Yu, W. Chen, R. Kania, G. Van Boven, and J. Been, "Underload-induced crack growth behaviour of minor cycles of pipeline steel in near-neutral pH environment," *Fatigue Fract. Eng. M.,* vol. 38, no. 6, pp. 681-692, 2015.

[91]   Y. Kang, W. Chen, R. Kania, G. V. Boven, and R. Worthingham, "Simulation of crack growth during hydrostatic testing of pipeline steel in near-neutral pH environment," *Corro. Sci.,* vol. 53, no. 3, pp. 968-975, 2011.

[92]   M. Yu, W. Chen, R. Kania, G. Van Boven, and J. Been, "Depressurization-induced crack growth enhancement for pipeline steels exposed to near-neutral pH environments," in *10th IPC*, Calgary AB, 2014.

[93]   Z. Xu, A. Daniel, K. Chevil, E. Gamboa, and W. Chen, "Differences in near-neutral pH crack growth behavior between oil pipelines and gas pipelines and corresponding crack growth mitigation strategies," in *12th IPC*, Calgary AB, 2018.

[94]   R. A. Oriani, "Whitney Award Lecture—1987: Hydrogen—The Versatile Embrittler," *Corrosion,* vol. 43, no. 7, pp. 390-397, 1987.

[95]   T. L. Anderson, "Chapter 10: Fatigue Crack Propagation," in *Fracture Mechanics: Fundamentals and Applications, 4th Edition*, 2017, pp. 471-536.

[96]   W. Chen, "An Overview of Near-Neutral pH Stress Corrosion Cracking in Pipelines and Mitigation Strategies for Its Initiation and Growth," *Corrosion,* vol. 72, no. 7, pp. 962-977, 2016.

[97]   R. R. Fessler and T. J. Barlo, "Threshold stress determination using tapered specimens and cyclic stresses," in *Environmental Sensitive Fracture: Evaluation and Comparison of Test Methods*, 1984, pp. 368-382.

[98]   F. King, R. Given, and W. Chen, "Detailed characterization of SCC cracks from the Nordegg rupture site and their mechanistic implications," Internal Report #01442. Nova Research & Technology Corp. 2000.

[99]   W. Chen, M. J. Wilmott, and T. R. Jack, "Hydrogen permeation behaviour of X-70 pipeline steel in NS4 neutral pH environment," in *2nd IPC*, Calgary AB, 2000, pp. 953-960.

[100]   L. Lei, F. Wang, Y. Gao, and Y. Du, "Studies on the construction parameter of an artificial occluded cell for in-situ inspection of the propagation rate of localized corrosion," *J. Mater. Sci. Technol.,* vol. 17, no. 3, pp. 355-358, 2001.

[101]   B. T. Lu, J. L. Luo, and P. R. Norton, "Environmentally assisted cracking mechanism of pipeline steel in near-neutral pH groundwater," *Corro. Sci.,* vol. 52, no. 5, pp. 1787-1795, 2010.

[102]   A. F. Liu, "Chapter 2: Deformation and Fracture Mechanisms and Static Strength of Metals," in *Mechanics and Mechanisms of Fracture: An Introduction*, 2005, pp. 62-84.

[103]   S. L. Asher and P. M. Singh, "Role of stress in transgranular stress corrosion cracking of transmission pipelines in near-neutral pH environments," *Corrosion,* vol. 65, no. 2, pp. 79-87, 2009.

[104]   T. L. Anderson, "Chapter 5: Fracture Mechanisms in Metals," in *Fracture Mechanics: Fundamentals and Applications, 4th Edition*, 2017, pp. 229-266.

[105]   K. Sadananda, A. K. Vasudevan, and I. W. Kang, "Effect of superimposed monotonic fracture modes on the K and Kmax parameters of fatigue crack propagation," *Acta Mater.,* vol. 51, no. 12, pp. 3399-3414, 2003.

[106] K. Sadananda and A. K. Vasudevan, "Crack tip driving forces and crack growth representation under fatigue," *Int. J. Fatigue,* vol. 26, no. 1, pp. 39-47, 2004.

[107] A. K. Vasudeven, K. Sadananda, and N. Louat, "A review of crack closure, fatigue crack threshold and related phenomena," *Mater. Sci. Eng. A,* vol. 188, no. 1, pp. 1-22, 1994.

[108] A. K. Vasudevan and K. Sadananda, "Application of unified fatigue damage approach to compression-tension region," *Int. J. Fatigue,* vol. 21, no. Supplement 1, pp. S263-S273, 1999.

[109] L. M. Young, P. L. Andresen, and T. M. Angeliu, "Crack Tip Strain Rate: Estimates Based on Continuum Theory and Experimental Measurement," in *Corrosion 2001*, NACE International, 2001, paper no. 01131.

[110] X. Y. Zhang, S. B. Lambert, R. Sutherby, and A. Plumtree, "Transgranular Stress Corrosion Cracking of X-60 Pipeline Steel in Simulated Ground Water " *Corrosion,* vol. 55, no. 3, pp. 297-305, 1999.

[111] B. Y. Fang, R. Eadie, W. X. Chen, and M. Elboujdaini, "Passivation/immersion method to grow pits in pipeline steel and a study of pit nucleation and growth resulting from the method," *Corros. Eng. Sci. Technol.,* vol. 44, no. 1, pp. 32-42, 2009.

[112] Target Products Ltd., "Enviro-Grit Glass Abrasive data sheet," Data Sheet February 18 2018, Available: https://www.targetproducts.com/UserContent/SpecSheets/enviro-grit.pdf, Accessed on: February 24, 2019.

[113] W. Chen, R. L. Eadie, and R. L. Sutherby, "- Environmental effects on near-neutral pH stress corrosion cracking in pipelines," in *Environment-Induced Cracking of Materials*, S. A. Shipilov, R. H. Jones, J. M. Olive, and R. B. Rebak, Eds. Amsterdam: Elsevier, 2008, pp. 211-220.

[114] J. C. Newman and I. S. Raju, "An empirical stress-intensity factor equation for the surface crack," *J. Eng. Fract. Mech.,* vol. 15, no. 1, pp. 185-192, 1981.

[115] ASTM Standard G1, "Practice for Preparing, Cleaning, and Evaluating Corrosion Test Specimens," 2017.

[116] W. Chen, J. Zhao, K. Chevil, E. Gamboa, and B. Alvarado, "Threshold geometrical dimensions of stage II cracks versus required resolution of crack-detection techniques," in *12th IPC*, Calgary AB, 2018.

[117] K. Tanaka and Y. Nakai, "Propagation and non-propagation of short fatigue cracks at a sharp notch," *Fatigue Eng. Mater. Struct.,* vol. 6, no. 4, pp. 315-327, 1983.

[118] M. H. El Haddad, T. H. Topper, and K. N. Smith, "Prediction of non propagating cracks," *Eng. Fracture Mech.,* vol. 11, no. 3, pp. 573-584, 1979.

[119] T. L. Anderson, "Chapter 2: Linear Elastic Fracture Mechanics," in *Fracture Mechanics: Fundamentals and Applications, 4th Edition*, 2017, pp. 25-108.

[120] X. Li, J. Ye, H. Zhang, T. Feng, J. Chen, and X. Hu, "Sandblasting induced stress release and enhanced adhesion strength of diamond films deposited on austenite stainless steel," *Applied Surface Science,* vol. 412, pp. 366-373, 2017.

[121] O. Bouledroua, M. Hadj Meliani, Z. Azari, A. Sorour, N. Merah, and G. Pluvinage, "Effect of Sandblasting on Tensile Properties, Hardness and Fracture Resistance of a Line Pipe Steel Used in Algeria for Oil Transport," *J. Fail. Anal. Prev.,* vol. 17, no. 5, pp. 890-904, 2017.

[122] R. K. Chintapalli, F. G. Marro, E. Jimenez-Pique, and M. Anglada, "Phase transformation and subsurface damage in 3Y-TZP after sandblasting," *Dental Materials,* vol. 29, no. 5, pp. 566-572, 2013.

[123] R. K. Chintapalli, A. Mestra Rodriguez, F. Garcia Marro, and M. Anglada, "Effect of sandblasting and residual stress on strength of zirconia for restorative dentistry applications," *J. Mech. Behav. Biomed. Mater.,* vol. 29, pp. 126-137, 2014.

[124] P. Horodek, M. K. Eseev, and A. G. Kobets, "Studies of stainless steel exposed to sandblasting," (in English), *Nukleonika,* vol. 60, no. 4, pp. 721-724, 2015.

[125] Y. C. Wu and Y. C. Jean, "Hydrogen-damaged defects near the surface in heavily deformed iron and steels investigated by slow positron annihilation spectroscopy," *Phys. Status Solidi (c),* vol. 4, no. 10, pp. 3506-3509, 2007.

[126] E. Dryzek, "Defect depth profiling after sphere indentation and blasting in aluminum and aluminum alloy detected by positron annihilation," *J. Mater. Sci.,* vol. 38, no. 18, pp. 3755-3763, 2003.

[127] L. Ding, H. Torbati-Sarraf, and A. Poursaee, "The influence of the sandblasting as a surface mechanical attrition treatment on the electrochemical behavior of carbon steel in different pH solutions," *Surface and Coatings Technology,* vol. 352, pp. 112-119, 2018.

[128] J. Zhao, K. Chevil, L. Lamborn, G. Van Boven, E. Gamboa, and W. Chen, "Pipeline SCADA Data Recording, Storing, and Filtering for Crack-Growth Analysis," *J. Pipeline Syst. Eng.,* vol. 10, no. 4, 2019.

APPENDIX A: PRESSURE FLUCTUATION DATA

In **Chapter 4**, pressure fluctuation data was presented for discussion in **Chapter 5**. Throughout the duration of the 91-day full-scale test, a pressure reading was recorded each second. As there were over 7 800 000 data points generated from this data collection procedure, the sheer volume of data was not practical to present in the body of this work. The following contains the pressure readings plotted over time, where each four day interval is shown in **Figure A.1 – Figure A.23**. It should be noted that the data sampling interval used to generate these plots was intentionally reduced to a 30 second interval as a sensitivity analysis showed that reduction to this data sampling interval did not introduce significant error.
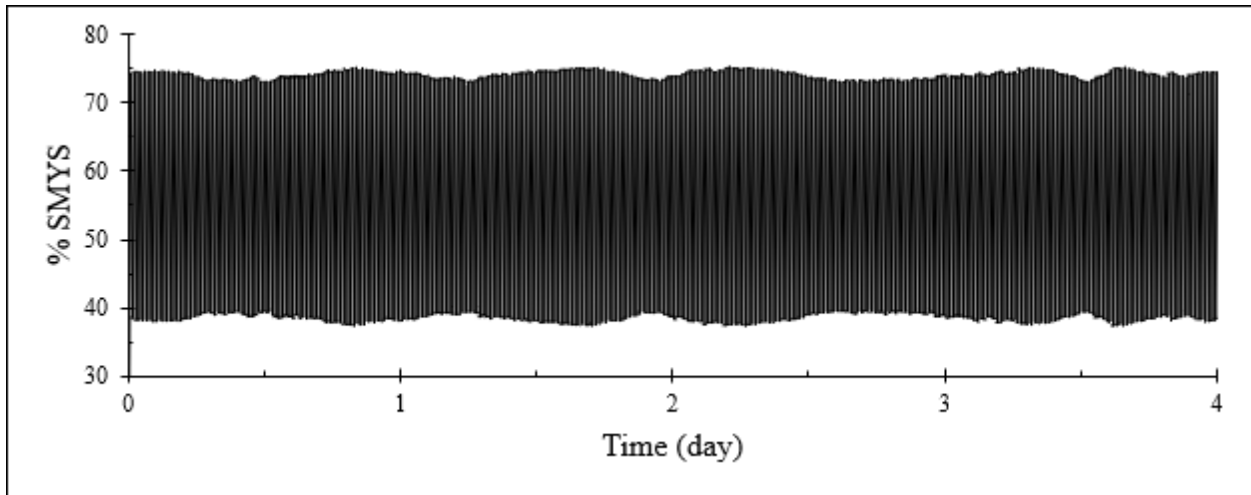
Figure A.1   Pressure fluctuations over time for day 0 – 4 of the full-scale test.
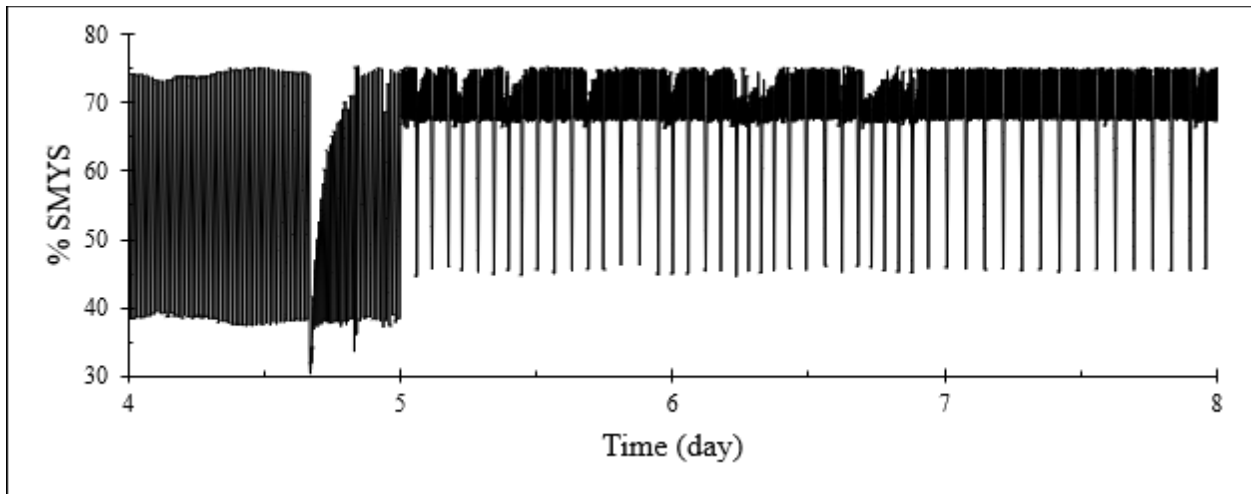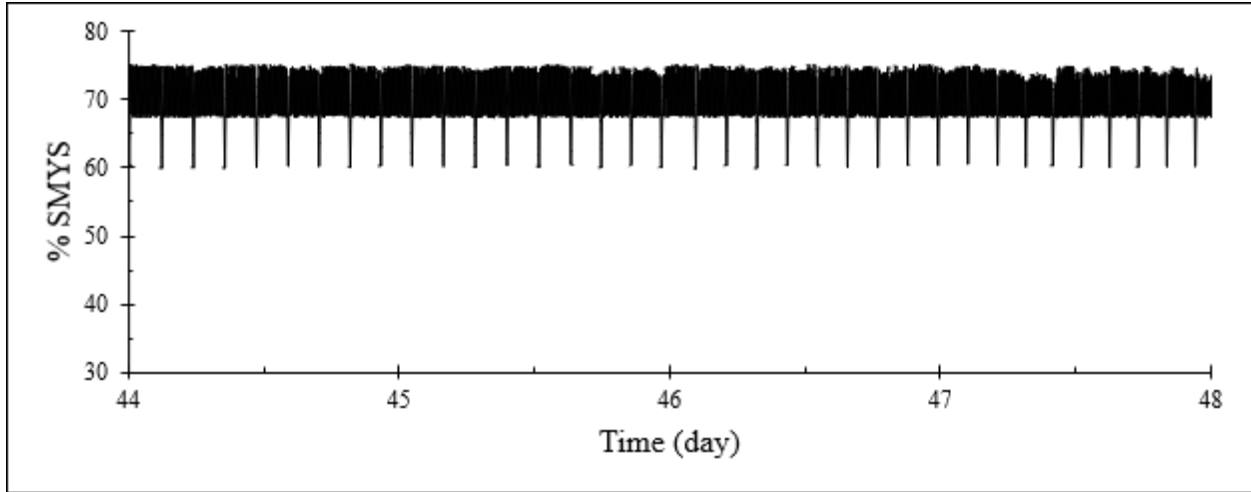

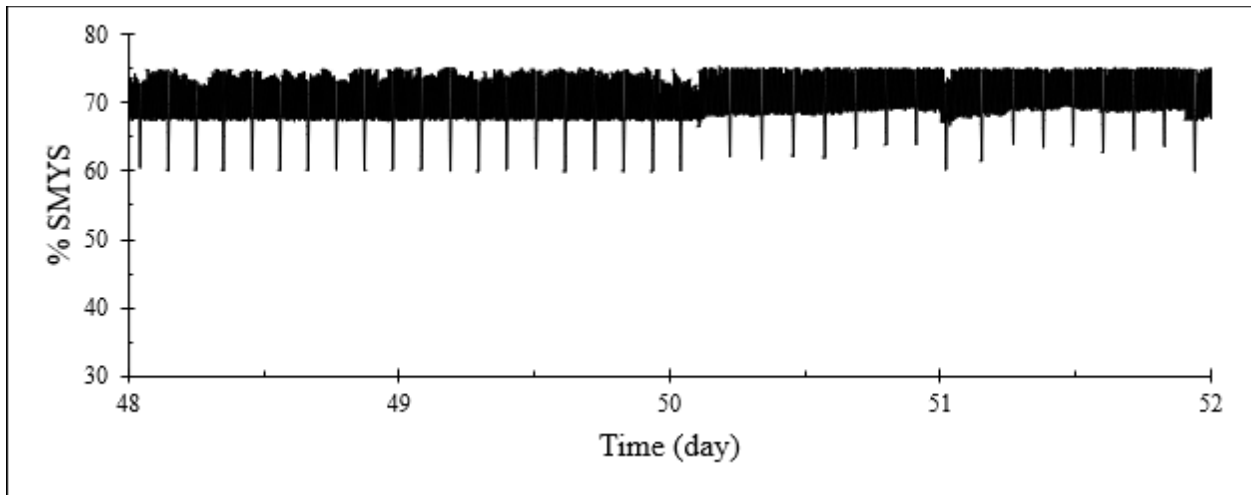**Figure A.2**   Pressure fluctuations over time for day 4 – 8 of the full-scale test.
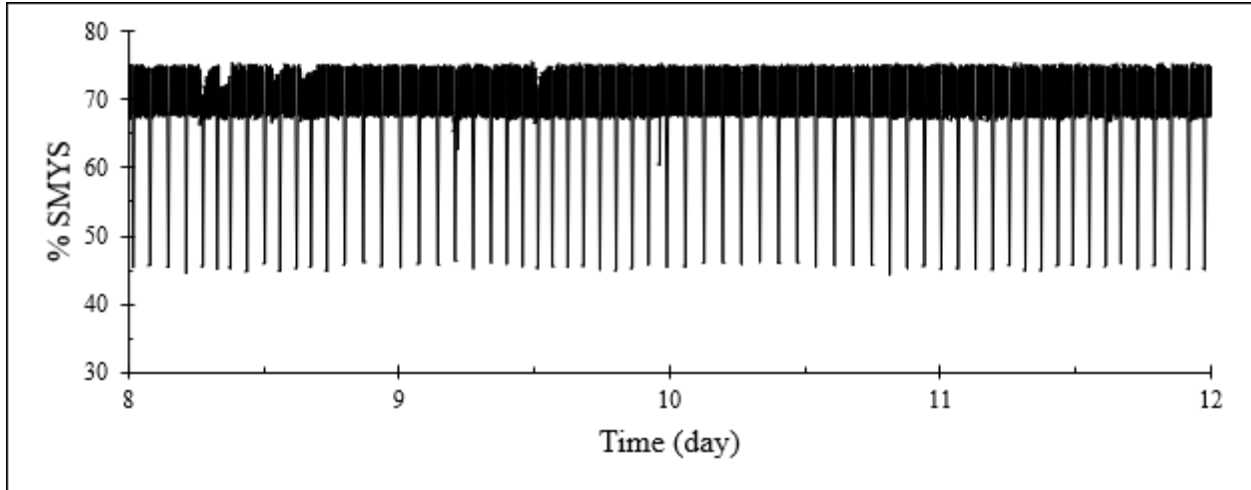
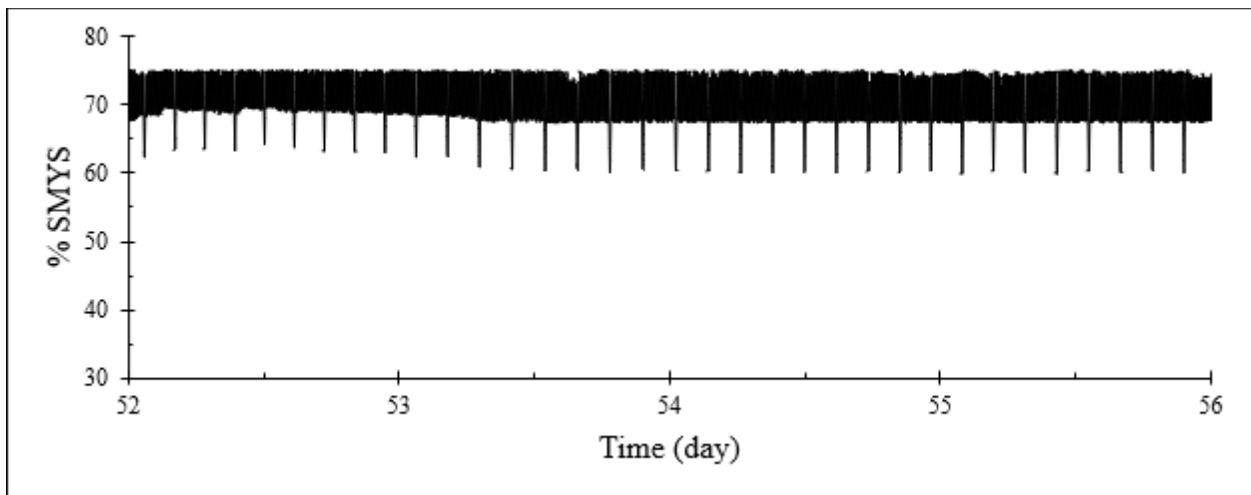**Figure A.3**   Pressure fluctuations over time for day 8 – 12 of the full-scale test.
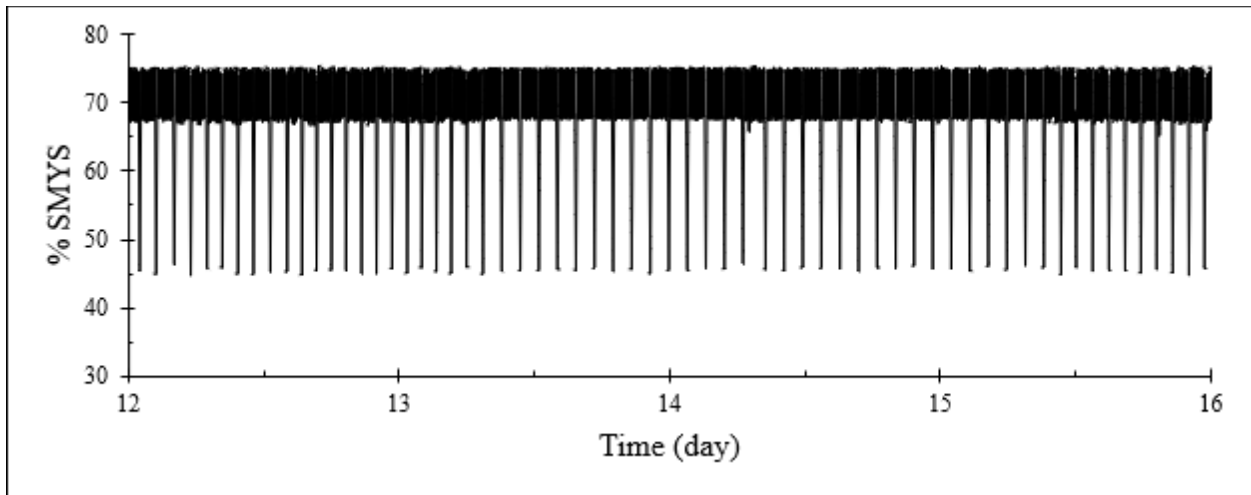
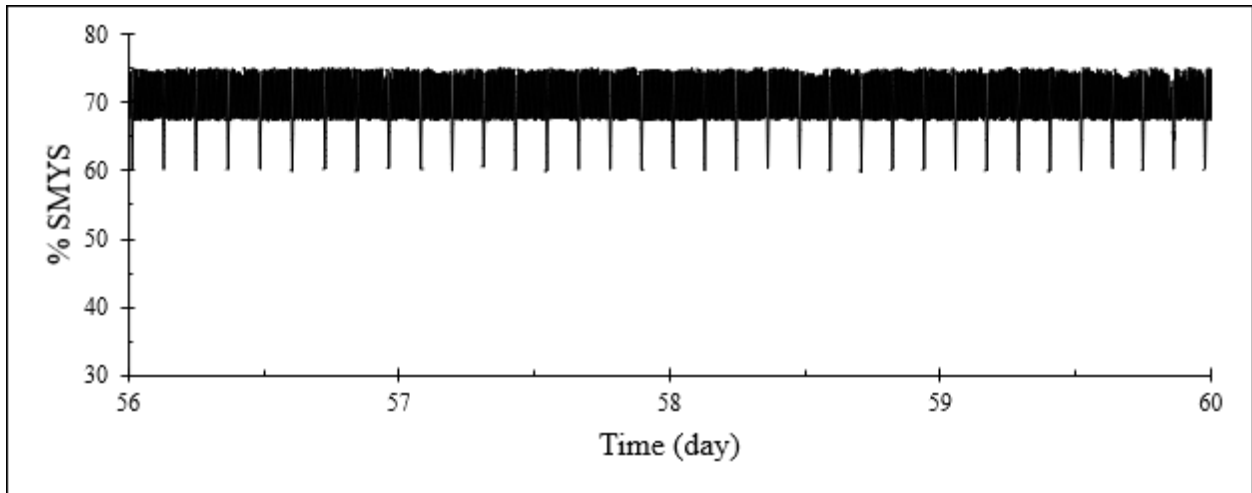**Figure A.4**   Pressure fluctuations over time for day 12 – 16 of the full-scale test.
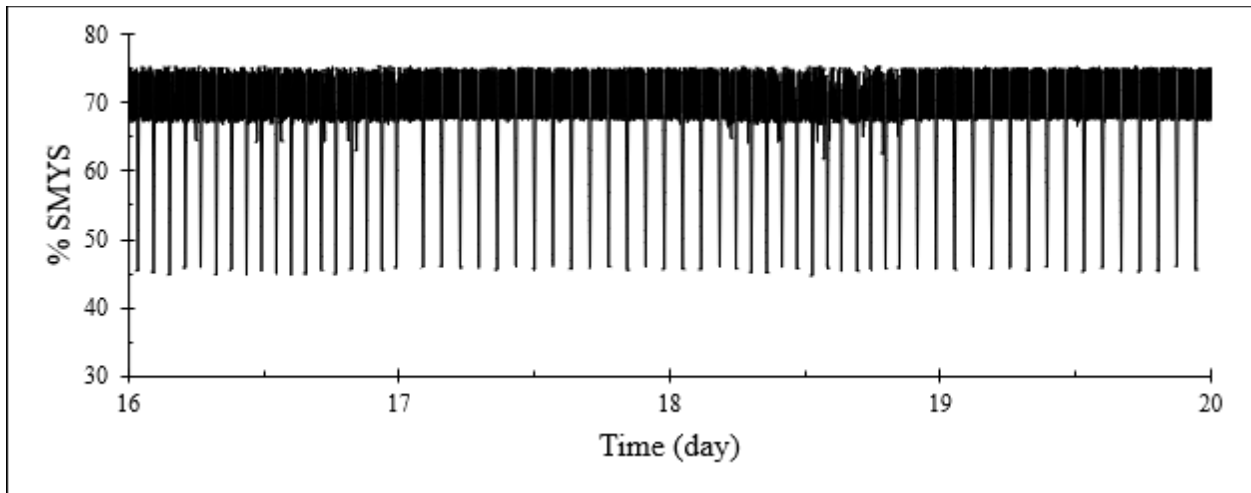
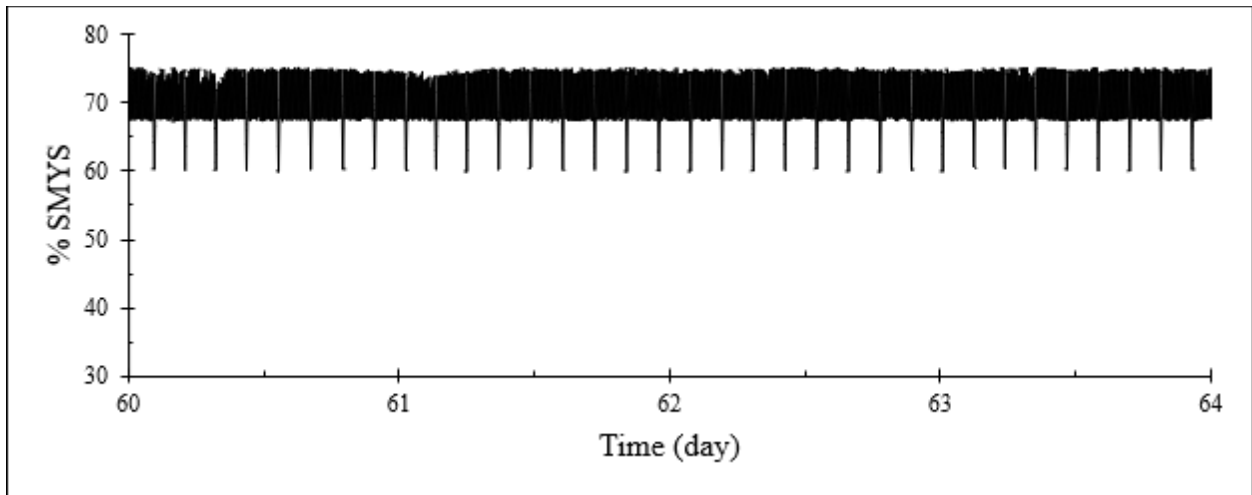**Figure A.5**   Pressure fluctuations over time for day 16 – 20 of the full-scale test.
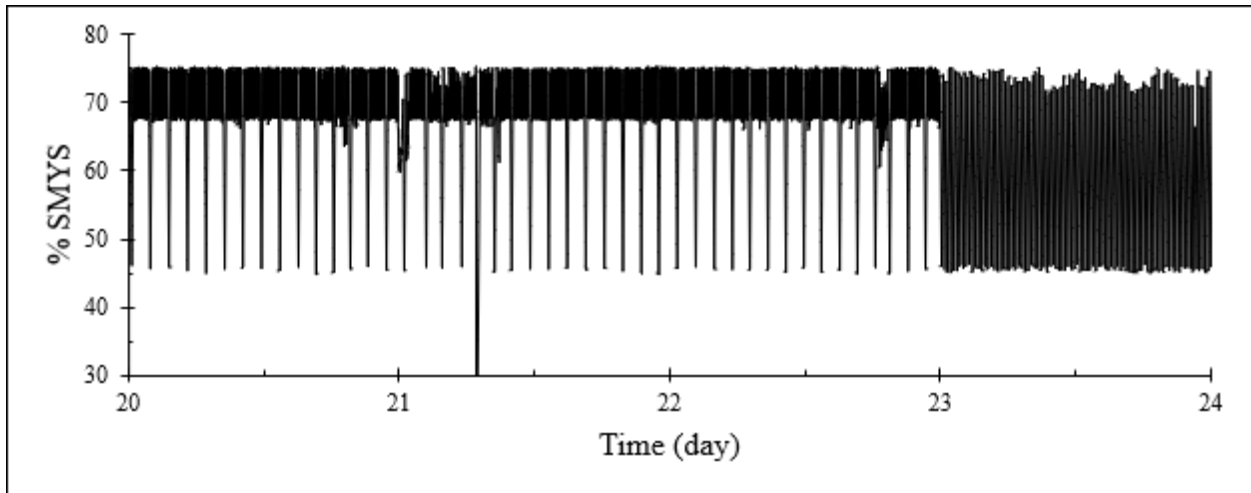
Figure A.6 Pressure fluctuations over time for day 20 – 24 of the full-scale test.
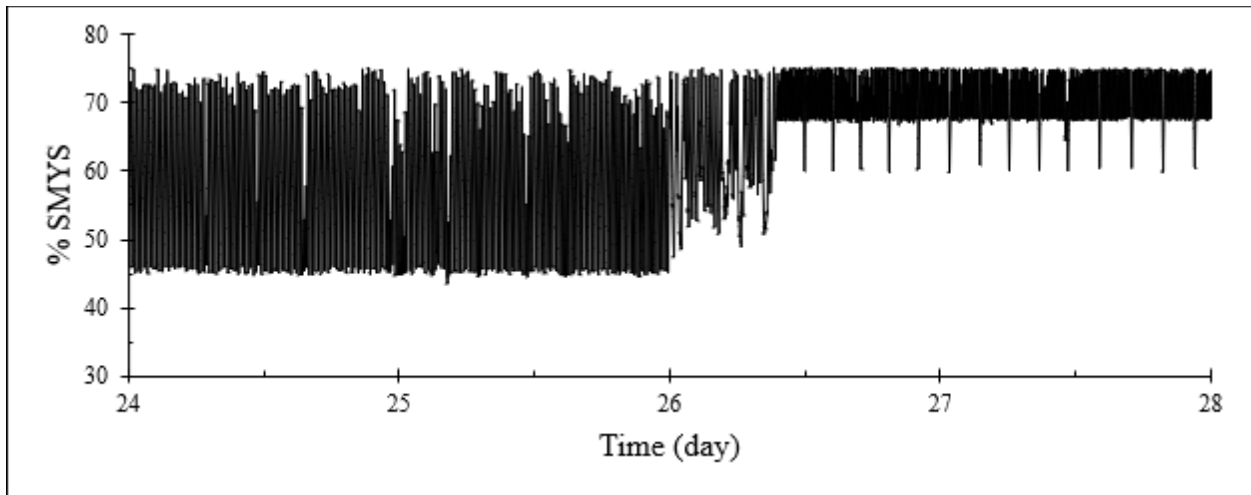
Figure A.7 Pressure fluctuations over time for day 24 – 28 of the full-scale test.
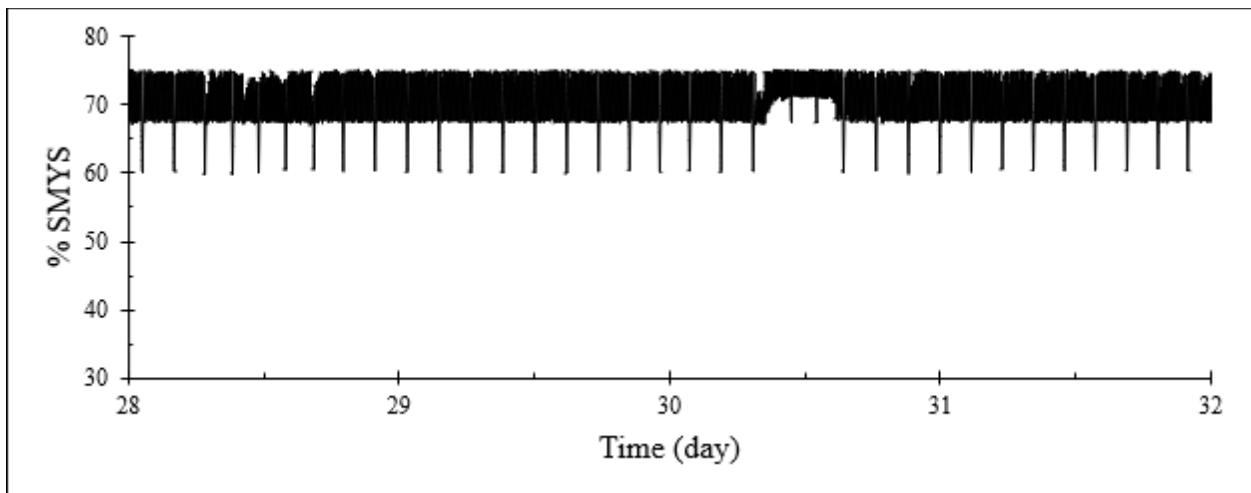
Figure A.8 Pressure fluctuations over time for day 28 – 32 of the full-scale test.
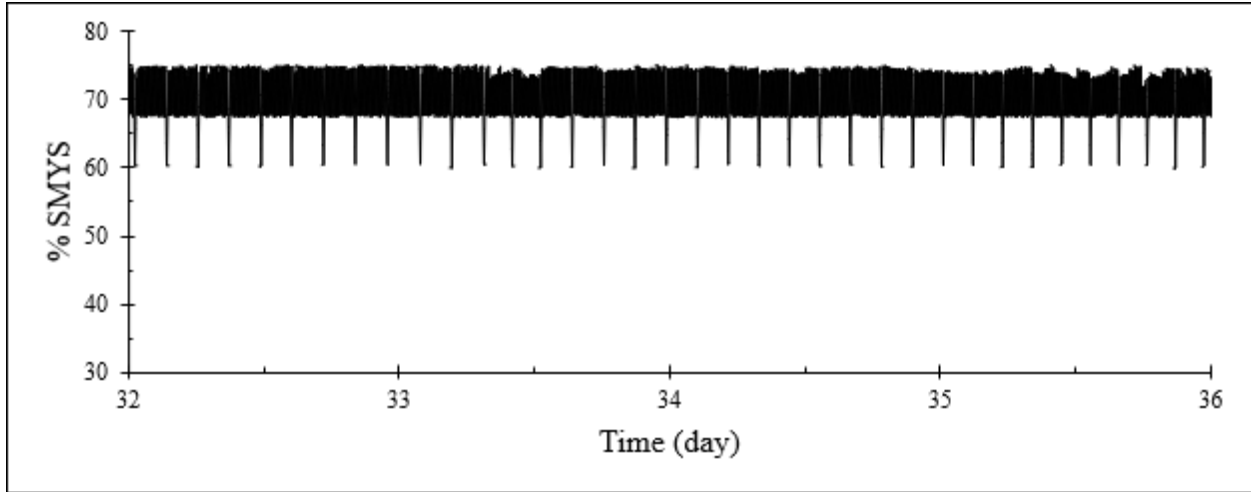
Figure A.9   Pressure fluctuations over time for day 32 – 36 of the full-scale test.
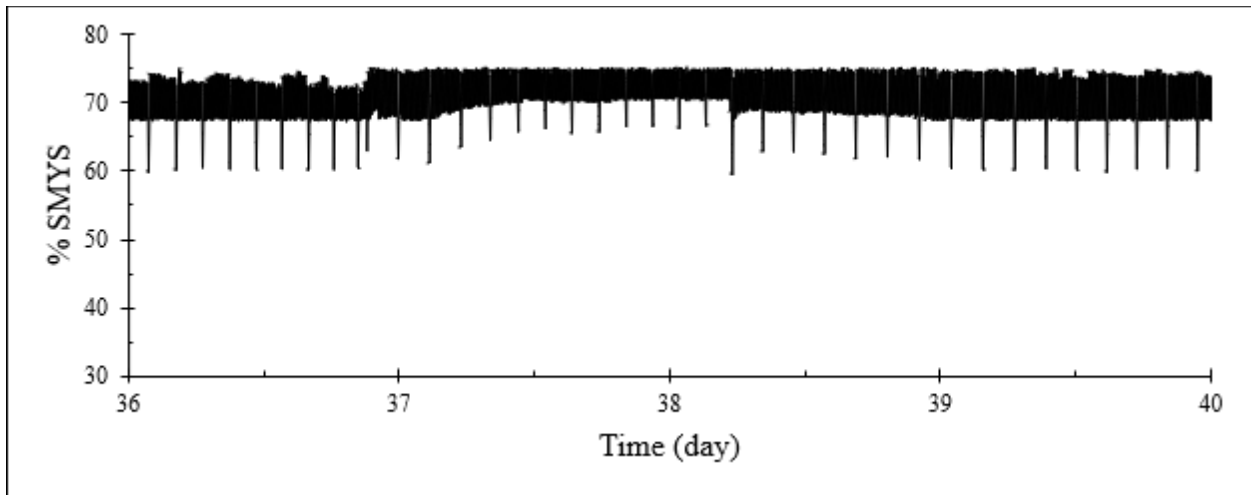
Figure A.10   Pressure fluctuations over time for day 36 – 40 of the full-scale test.
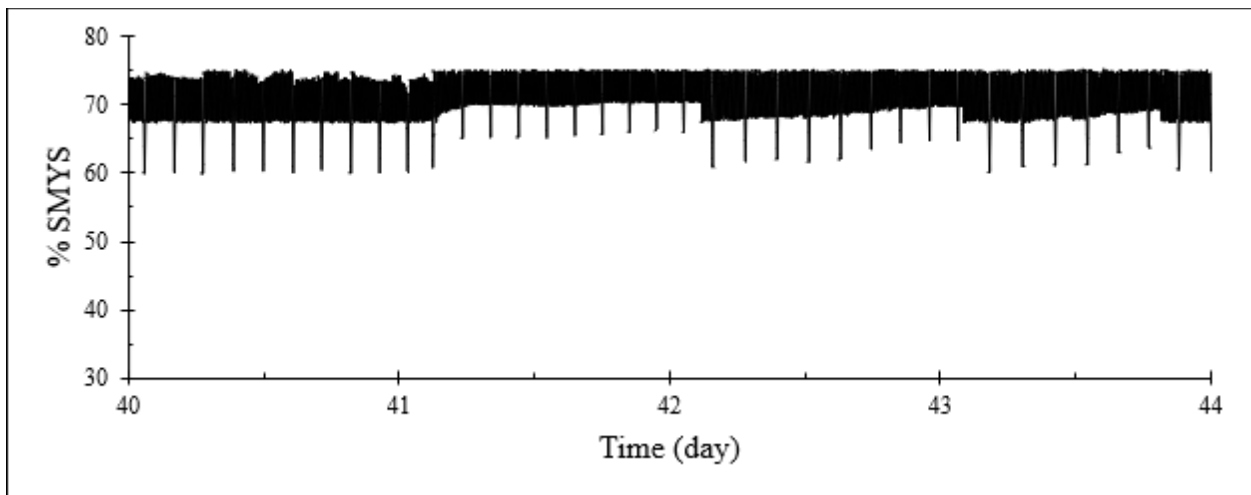
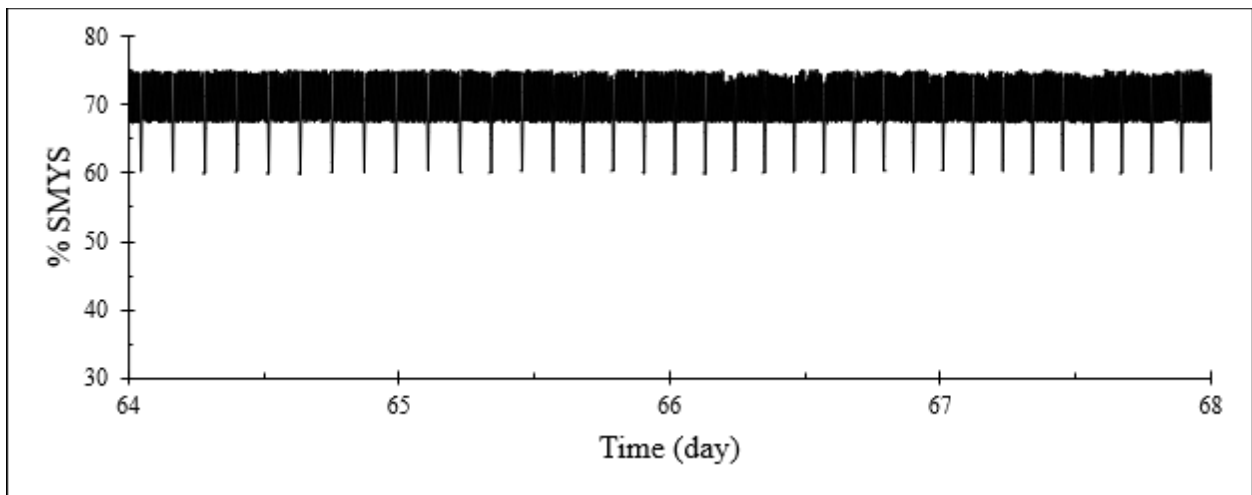**Figure A.11**   Pressure fluctuations over time for day 40 – 44 of the full-scale test.

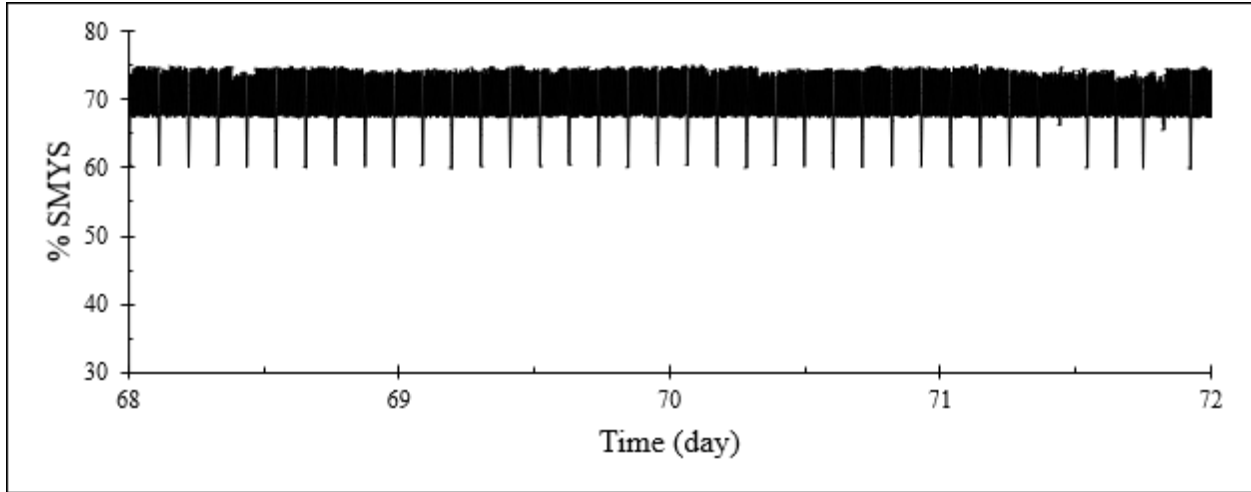**Figure A.12**　　Pressure fluctuations over time for day 44 – 48 of the full-scale test.

Figure A.13　　Pressure fluctuations over time for day 48 – 52 of the full-scale test.
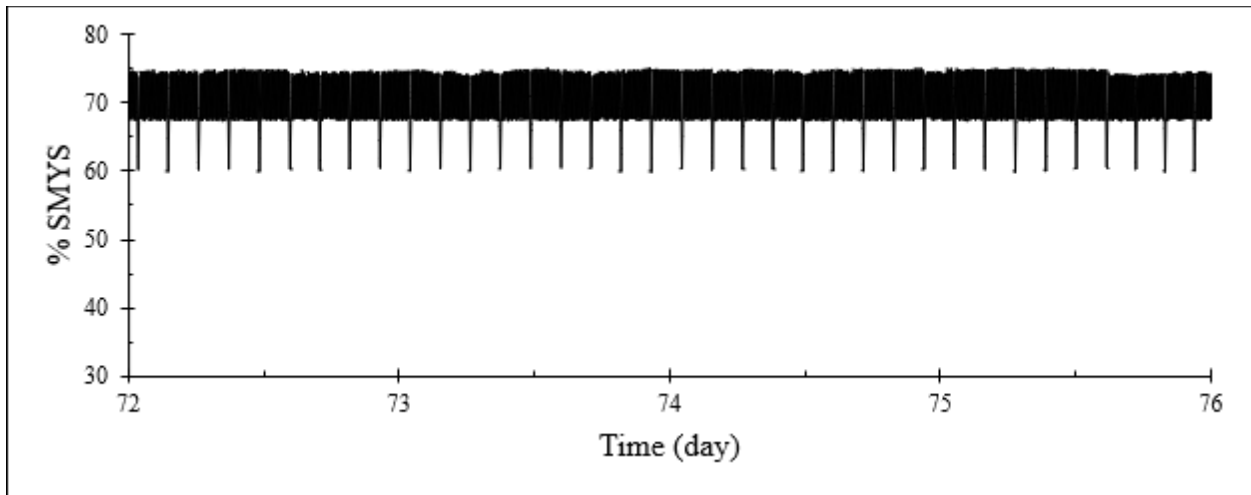

Figure A.14　　Pressure fluctuations over time for day 52 – 56 of the full-scale test.

Figure A.15 Pressure fluctuations over time for day 56 – 60 of the full-scale test.

Figure A.16 Pressure fluctuations over time for day 60 – 64 of the full-scale test.

Figure A.17 Pressure fluctuations over time for day 64 – 68 of the full-scale test.

Figure A.18   Pressure fluctuations over time for day 68 – 72 of the full-scale test.

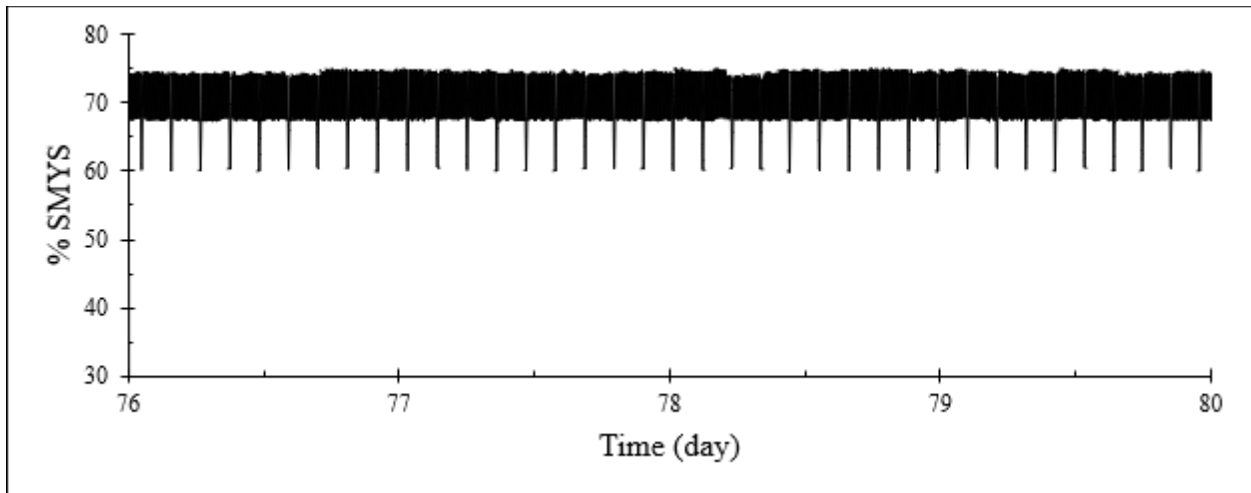**Figure A.19**   Pressure fluctuations over time for day 72 – 76 of the full-scale test.

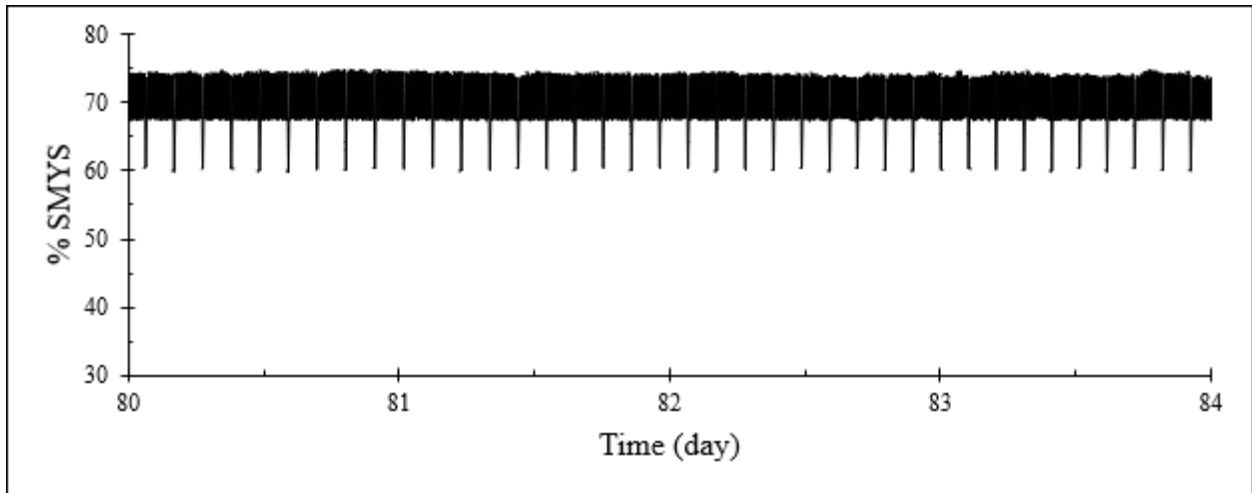**Figure A.20**   Pressure fluctuations over time for day 76 – 80 of the full-scale test.

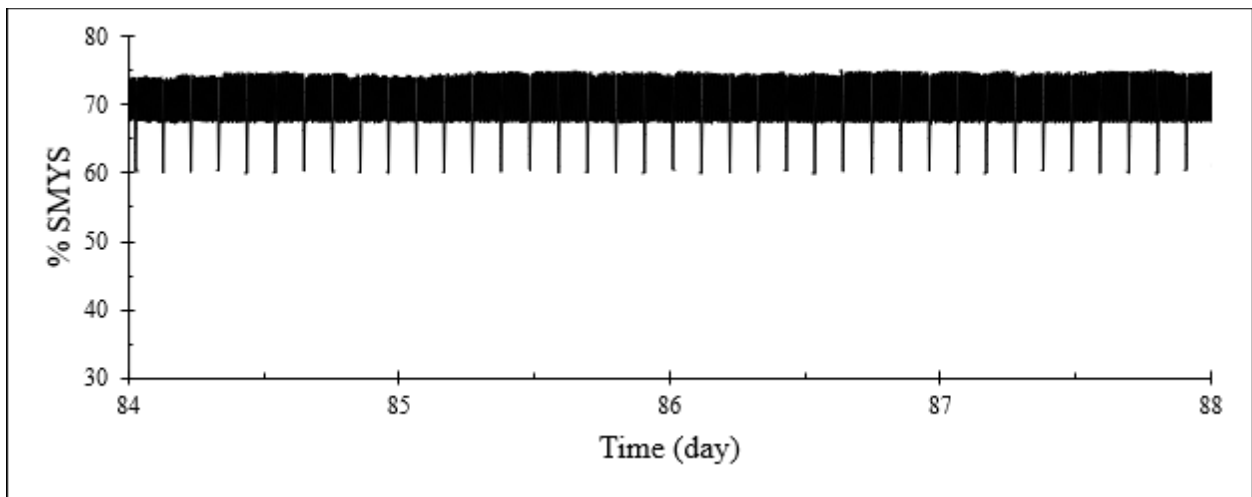**Figure A.21**   Pressure fluctuations over time for day 80 – 84 of the full-scale test.

Figure A.22   Pressure fluctuations over time for day 84 – 88 of the full-scale test.
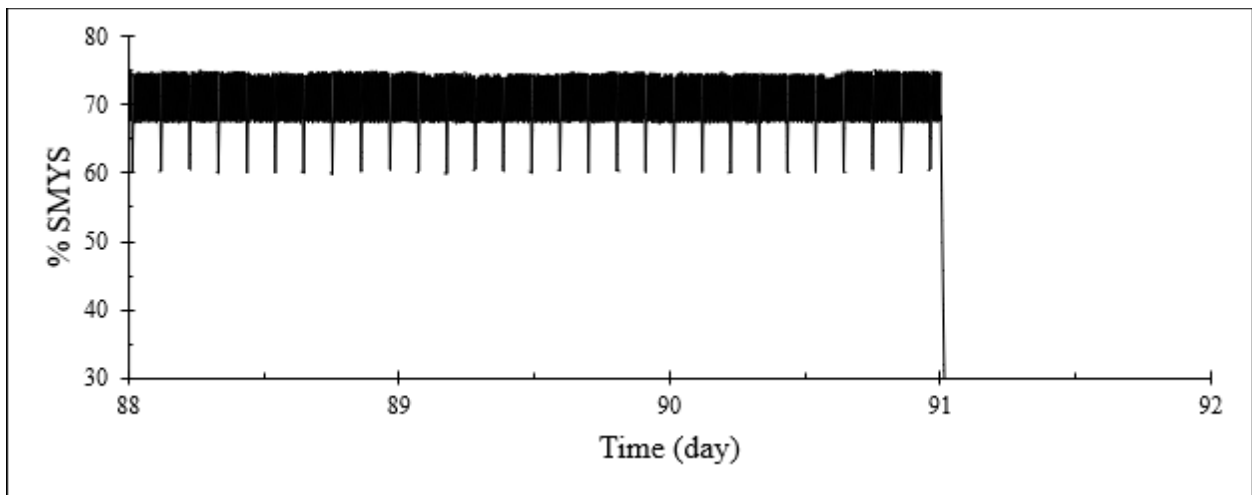

Figure A.23   Pressure fluctuations over time for day 88 – 91 of the full-scale test.

130

APPENDIX B: SAFETY MEASURES

The full-scale test was considered a pressurized vessel and redundancies were developed to ensure the safety of University of Alberta employees and the public. The hierarchy of hazard control is a system used by many industries to minimize and control exposure to hazards. In order from most effective to lease effective the controls are elimination, substitution, engineering controls, administrative controls and personal protective equipment (PPE). The controls used during the full-scale test (excluding PPE) are listed below.

Elimination: The risk of rupture due to internal corrosion of the pipe segment was eliminated by adding inhibitor to the internal fluid throughout the test.

Substitution: An internal gas media was substituted for liquid media to eliminate the dangers associated with rapid expansion of pressurized gas in the event of a rupture.

Engineering controls: An emergency relief valve was used to protect the pipe from unexpected dangerously high pressure. An uninterruptible power supply was implemented to provide emergency backup power to the test's critical systems in the event of an unplanned power outage. In addition, the control valve supplying compressed air to drive the pneumatic pump was a normally closed valve. This design ensured that the pump would stop if the pressure control system lost power as the pump air supply would be cut off.

Administrative controls: The test was conducted in a basement corridor of the I.F Morrison Structures Laboratory below the building's concrete strong floor. The strong floor and basement corridor walls were made of 66 cm thick reinforced concrete and access to the basement corridor housing the pipe segment was restricted.